Julius-Maximilians-
UNIVERSITÄT
WÜRZBURG

# Recombination Dynamics in Organic Solar Cells

Dissertation zur Erlangung des
naturwissenschaftlichen Doktorgrades
der Julius-Maximilians-Universität Würzburg

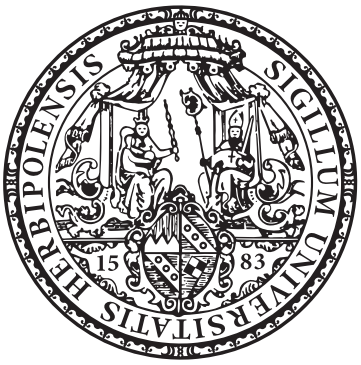


vorgelegt von
**Alexander Förtig**

aus
Beuchen im Odenwald

Würzburg 2013

Eingereicht am: 31.05.2013
bei der Fakultät für Physik und Astronomie

1. Gutachter: Prof. Dr. Vladimir Dyakonov
2. Gutachter: Prof. Dr. Jean Geurts

der Dissertation.

1. Prüfer: Prof. Dr. Vladimir Dyakonov
2. Prüfer: Prof. Dr. Jean Geurts
3. Prüfer: Prof. Dr. Giorgio Sangiovanni

im Promotionskolloquium.

Tag des Promotionskolloqiums: 28.10.2013

Doktorurkunde ausgehändigt am:

» Es ist nicht das Wissen, sondern das Lernen,
nicht das Besitzen, sondern das Erwerben,
nicht das Dasein, sondern das Hinkommen,
was den grössten Genuss gewährt. «

Carl Friedrich Gauß (1777-1855)

# Abstract

Besides established, conventional inorganic photovoltaics—mainly based on silicon—organic photovoltaics (OPV) are well on the way to represent a low-cost, environment friendly, complementary technology in near future. Production costs, solar cell lifetime and performance are the relevant factors which need to be optimized to enable a market launch of OPV.

In this work, the efficiency of organic solar cells and their limitation due to charge carrier recombination are investigated. To analyze solar cells under operating conditions, time-resolved techniques such as transient photovoltage (TPV), transient photocurrent (TPC) and charge extraction (CE) are applied in combination with time delayed collection field (TDCF) measurements. Solution processed and evaporated samples of different material composition and varying device architectures are studied.

The standard OPV reference system, P3HT:$PC_{61}BM$, is analyzed for various temperatures in terms of charge carrier lifetime and charge carrier density for a range of illumination intensities. The applicability of the Shockley Equation for organic solar cells is validated in case of field-independent charge photogeneration. In addition, a consistent model is presented, directly relating the ideality factor to the recombination of free with trapped charge carriers in an exponential density of states.

An approach known as $j/V$ reconstruction enables to identify the performance limiting loss mechanism of as-prepared and thermally treated P3HT:$PC_{61}BM$ solar cells. This procedure, involving TPV, CE and TDCF measurements, is extended to samples based on the rather new, low-band gap polymer PTB7 in combination with $PC_{71}BM$. While in the devices processed from pure chlorobenzene solution considerable geminate and nongeminate losses are observed, the use of a solvent additive facilitates efficient polaron pair dissociation minimizing geminate recombination.

Finally, in collaboration with the IMEC institute in Leuven, the two main organic solar cell device architectures, planar and bulk heterojunction—both based on CuPc and $C_{60}$—are directly compared in terms of nongeminate recombination and charge carrier distribution. Two experimental techniques, TPV and CE, as well as a macroscopic device simulation are applied to reveal the origin of different $V_{oc}$ vs. light intensity dependence.

# Zusammenfassung

Neben herkömmlichen, konventionellen anorganischen Solarzellen—hauptsächlich auf Silizium basierend—ist die Organische Photovoltaik (OPV) auf dem besten Wege in naher Zukunft eine kostengünstige, umweltfreundliche, komplementäre Technolgie darzustellen. Die Produktionskosten, die Lebenszeit der Solarzellen sowie deren Wirkungsgrad müssen dabei weiter optimiert werden, um einen Markteintritt der OPV zu ermöglichen.

Die vorliegende Arbeit befasst sich mit der Effizienz organischer Solarzellen und deren Limitierung durch die Rekombination von Ladungsträgern. Um funktionsfähige Zellen zu untersuchen, werden zeitaufgelöste Experimente wie die Messung der transienten Photospannung (TPV), des transienten Photostroms (TPC), die Ladungsextraktion (CE) sowie die *time delayed collection field* (TDCF) Methode angewandt. Untersucht werden sowohl flüssig prozessierte als auch aufgedampfte Proben, unterschiedliche Materialzusammensetzungen und verschiedene Probengeometrien.

Das Standardmaterialsystem der OPV, P3HT:$PC_{61}BM$, wird bei verschiedenen Temperaturen und Beleuchtungsstärken auf die Lebenszeit und Dichte der photogenerierten Ladungsträger überprüft. Für den Fall spannungsunabhängiger Generation von Ladungsträgern zeigt sich die Anwendbarkeit der Shockley-Gleichung auf organische Solarzellen. Des Weiteren wird ein konsistentes Modell erläutert, welches den Idealtitätsfaktor direkt mit der Rekombination von freien mit gefangenen, exponentiell verteilten Ladungsträgern verknüpft.

Ein Ansatz, bekannt unter der Bezeichung $j/V$ Rekonstruktion, ermöglicht es, den leistungslimitierenden Verlustmechanismus in unbehandelten und thermisch geheizten P3HT:$PC_{61}BM$ Solarzellen zu identifizieren. Dieses Verfahren, welches TPV, CE und TDCF Messungen beinhaltet, wird auf Proben basierend auf dem neuartigen, *low-band gap* Polymer PTB7 in Verbindung mit dem Fulleren $PC_{71}BM$ ausgeweitet. Während in der Zelle hergestellt aus reinem Chlorbenzol beträchtliche geminale wie nichtgeminale Verluste zu beobachten sind, erleichtert die Zugabe eines Lösungsmittelzusatzes die Polaronenpaartrennung, was zu einer starken Reduktion geminaler Verluste führt.

In einer Kooperation mit dem IMEC Institut in Leuven, werden abschließend die beiden bedeutensten Probenarchitekturen organischer Solarzellen, die planare und die Mischübergang Struktur, jeweils basierend auf CuPC und $C_{60}$, bezüglich nichtgeminaler Rekombination und Ladungsträgerverteilung miteinander verglichen. Neben den beiden experimentellen Techniken um TPV und CE werden makroskopische Simulationen herangezogen, um den Ursprung unterschiedlichen $V_{oc}$ vs. Lichtintensität–Verhaltens zu erklären.

# Contents

# Chapter 1
# Introduction

The need for a sustainable, nonpolluting and affordable energy supply for a fast growing world-wide population has been one of the most addressed issues in recent years. The goal to establish renewables as a substantial energy source involves changes in landscape and human environment and will certainly require changes in attitude. Mankind has exploited fossil energy resources such as coal and crude oil for decades and deployed nuclear power plants, without recognizing or considering the effects of atmosphere pollution, especially by carbon dioxide emission, or the dangers of nuclear power and its waste. Even though *peak oil*, the point in time of maximum rate of crude oil extraction has not been reached yet and uranium supply still suffices, one can observe an increased preference for *green* energies.

In 2011 Fukushima brought the potential threats of nuclear power back to our mind. At least since then, politicians especially in Europe, and in particular in Germany, opt for a regenerative energy supply. In 2011 the European Union demanded that renewable energy sources provide 20% of electric energy in 2020 and aimed at reducing green house gas emission by 20% [1]. The decision by the Federal Republic of Germany to withdraw from nuclear power effective by the end of 2022 is an ambitious and unique endeavor. It demands dramatic efforts in further development and deployment of renewable energy sources, the reorganization of the electricity grid and the optimization of the energy storage system in order to diminish the volatility problems of solar and wind energy.

The deployment of renewable energy technologies, such as biomass and wind energy, but especially the photovoltaic (PV) energy, were stimulated by generous feed-in tariffs in Germany in recent years. With an annual growth rate of more than 7 GW from 2010 to 2012 over 30 GW of photovoltaic power was installed by the end of 2012 [2]. In 2011 the solar cell market was dominated by multi crystalline silicon (57%) followed by crystalline silicon (31%) and thin film technologies like cadmium telluride (5%) [3]. The PV technology in Germany in general has to deal with rather low full-load hours of 950 h per year. Nevertheless, in 2012 almost 28 TWh of electric energy were generated by photovoltaic modules, representing 5% of the German net electricity demand [4].

The elementary process of converting solar irradiation into electric power by any solar cell is known as the photovoltaic effect. It was discovered by A. Becquerel in 1892 [5]. The distinct energy of a photon is absorbed and excites an electron to a state higher in energy. The first noteworthy silicon solar cell with a power conversion efficiency (PCE) of $\eta = 6\%$ was realized by the group around Daryl Chapin at the Bell Laboratories in 1954 [6]. The upper theoretical limit in terms of efficiency for single p–n junctions was determined to be about 30% by W. Shockley and H. J. Queisser [7] and is nowadays almost realized by crystalline Si solar cells ($\eta = 25.0\%$) [8].

Besides the above described conventional inorganic solar cells a younger technology, based on organic semiconductors, with new, innovative perspectives has developed rapidly within the last two decades. Even though the price for Si-modules in Germany has dropped meanwhile due to upscaling and outsourcing of production to low-wage countries, on average below 1 €/Wp, organic solar cells still are supposed to bring along a price advantage due to easily upscaleable, low temperature mass production [9, 10]. Next to economic reasons, the higher absorption coefficient of organic materials paves the way for thin active layers and—in combination with conductive paper or foil—for flexible, innovative applications [11]. Companies willing to commercialize organic photovoltaics (OPV) aim on gadget applications, flexible and mobile modules for the outdoor market or semitransparent solar cells in windows and thus building integration [12, 13, 14]. The used semiconducting polymers and fullerenes are soluble, for example in standard solvents like chlorobenzene or toluene and enable deposition by printing, spin-coating or doctor blading [10, 15]. If not soluble, they can be deposited by thermal evaporation under high vacuum.

While light emitting diodes based on organic semiconductors are already established on the market, the organic solar cell technology still has to catch up. Recently, efficiencies above $\eta = 11\%$ were reported by Mitsubishi Chemicals for laboratory single cells, but modules still reside far below at around 4% [8]. To realize the market launch of OPV, on the one hand product stability in terms of extrinsic solar cell degradation, for instance by moisture or oxygen, is one crucial aspect [16]. On the other hand, steady efficiency improvements are required and a detailed understanding of OPV working principle such as charge photogeneration and charge carrier recombination is essential. To gain a better insight, the present work addresses the issues of charge carrier recombination and active layer morphology in organic solar cells and their impact on device performance.

After a general overview on organic semiconductors and organic solar cells the two basic recombination mechanisms are introduced and their influence on solar cell performance is discussed. Then the experimental techniques used

in this work are highlighted and the relevant organic materials are presented together with details on device preparation. In the experimental results a reference system is used for an intensive temperature dependent study on the Shockley Equation, originally developed for inorganic p–n junctions. The used techniques, transient photovoltage and transient photocurrent, enable to study charge carrier lifetime and charge carrier density of organic solar cells under operating conditions and the evaluation of a recombination ideality factor. Subsequently, the impact of charge carrier recombination on the current–voltage characteristic for two material systems and different active layer morphologies is analyzed in detail. Finally, the two main organic solar cell device architectures, planar and bulk heterojunction, are directly compared in terms of nongeminate recombination and charge carrier distribution.

Chapter 2

# Organic Photovoltaics

## 2.1 From Organic Semiconductors to Solar Cells – A Brief Overview

Even though the main breakthrough in the field of organic semiconductors can be clearly found within the last three decades, their birth can be dated back to the beginning of the 20th century with the first study on the photoconductivity of anthracene crystals [17]. The discovery of electroluminescence in the 1960s [18] can be seen as the starting point of systematic research on the fundamental processes such as photo excitation and charge transport properties of the so-called small molecules [19, 20]. Another milestone in the development of organic semiconductors happened in the end seventies, when a new class of organic semiconductors was introduced and investigated in terms of electrical conductivity: (halogen) doped, highly conductive, conjugated polymers. Their discovery was honored with the Nobel Prize in Chemistry in the year 2000 [21, 22, 20].

Two major classes of organic semiconductors are distinguished. On the one hand, the class of small molecules, normally deposited from the gas phase (sublimation or evaporation), which partly even show a crystalline growth and a high degree of order. On the other hand, the younger material class of conjugated polymers, usually processed from the liquid phase by spin-coating or printing have the potential to revolutionize electronics. In both classes the conductivity originates from a conjugated $\pi$-electron system, further explained in Sec. 2.3.4.

First organic solar cell (OSC) devices consisted of a single, pure organic layer embedded between two electrodes of different work functions and yielded power conversion efficiencies (PCE) $\eta \ll 1\%$. The low PCE originated from the generation of a strongly bound (binding energy 0.5–1 eV) electron–hole pair (Frenkel exciton) upon photon absorption due to the low dielectric constant ($\varepsilon \approx 3 - 4$) in organic materials. Thus, separating electron and hole requires sufficient excess energy or the metal electrode within the distance a Frenkel exciton moves during its lifetime, called exciton diffusion length ($<$ 20 nm). Both possibilities are not very likely at room temperature for active layer thicknesses up to a few hundred nanometers. This results in a high prob-

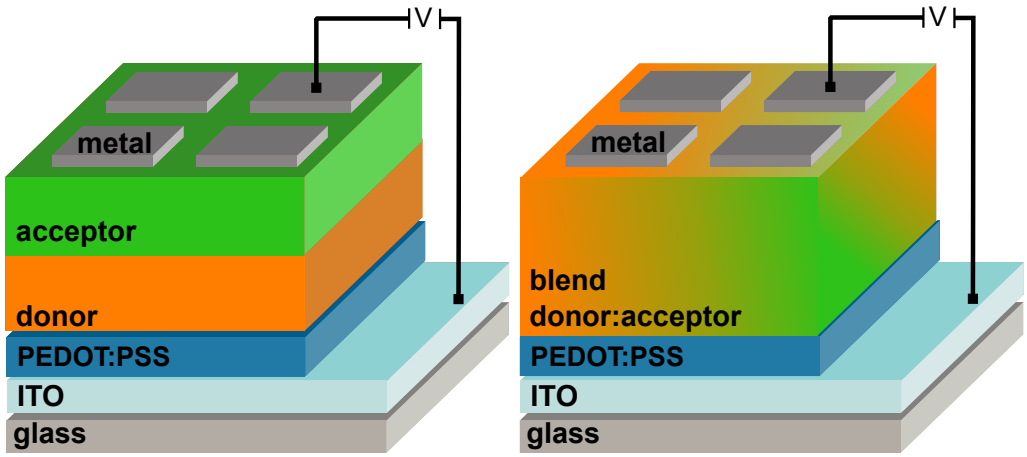


(a) planar heterojunction (b) bulk heterojunction

Figure 2.1: Device structure of a planar heterojunction (a) consisting of adjacent acceptor and donor layer and a bulk heterojunction organic solar cell (b), implemented by a donor–acceptor blend.

ability of a subsequent decay of the excited electron–hole pair to its ground state (recombination) and a decisive loss mechanism.

In the year 1986, Tang established a new approach to overcome the drawback of the strong exciton binding energy—the first organic bilayer solar cell with a PCE of $\eta \approx 1\%$ [23]. Thereby, two adjacent thin layers of two different organic compounds (see Fig. 2.1(a)) were deposited on top of each other to form a planar heterojunction (PHJ). In this particular case, Tang chose copper phthalocyanine (CuPc) for the bottom and a perylene tetra carboxylic (PV) derivative for the top layer, whereas the photon absorption (exciton generation) primarily occurs in the CuPc. For a more efficient exciton dissociation than in a single layer device, the second layer of PV derivative favorably provides a high electron affinity to overcome the exciton binding energy. If the exciton reaches the heterointerface within its lifetime, the electron is transferred from the CuPc (donor) to the PV molecule (acceptor). Due to the weak screening of the electric field in organic semiconductors, the so formed state (denoted as polaron pair) is still Coulomb bound and needs to be completely dissociated to obtain free charges (see Sec. 2.3.3). Nevertheless, as donor thicknesses of 100-200 nm are necessary to absorb most of the incoming photons, the exciton dissociation yield in a PHJ solar cell is still rather low, as only a few percent of the generated excitons reach the donor–acceptor interface. To overcome this major drawback of a PHJ device, the concept of bulk heterojunction (BHJ) solar cells was introduced in the mid nineties [24, 25]. Instead of two adjacent pure semiconducting layers, the active volume of a BHJ solar

cell consists of a well intermixed donor–acceptor system (see Fig. 2.1(b)), providing a spatially distributed heterointerface, which allows a very efficient exciton dissociation, approaching nearly 100%. This is realized by co-evaporation of conjugated small molecules or by spin-coating a polymer–fullerene blend from solution. Despite the enhanced exciton dissociation yield, the complete separation of polaron pairs and the transport of charge carriers in the more disordered bulk system provide further challenges discussed in Section 2.3. Yu *et al.* started with a bulk heterojunction solar cell yielding an efficiency of around 1% [25]. The subsequent efficiency improvements of BHJ devices during the last two decades strongly correlate with the attempts to control the active layer morphology in order to improve for instance the charge carrier transport. Thereby, solution processed active layers are mainly influenced by the choice of solvent, by a post-annealing step [26, 27] or by a second solvent (additive) [28]. This continous and systematic fundamental research as well as new synthesized low-band gap materials lead to recent efficiency values exceeding the benchmark of 10% [14] and by now even 11% [8].

## 2.2 Organic Semiconductors

In the general public, the term *organic* is associated with a living organism, for example a flower or the human body. From the view of fundamental research an organic material is usually artificially synthesized in the lab and is defined by its carbon-based compounds, hydrocarbons or their derivatives and could include any number of other elements, e.g. sulfur, oxygen or nitrogen. Thereby, the carbon atom (C), with its ground state electron configuration [He] $2s^2\ 2p^2$ and four possible covalent chemical bonds, plays the decisive role for the electric properties of organic semiconductors and the ability of carbon to form three $sp^2$-hybrid orbitals from one $2s$- and two of the $p$-orbitals ($2p_x 2p_y$) is exploited. The $sp^2$-orbitals arrange in coplanar $\sigma$-bonds at an angle of 120° and are superposed by a perpendicular $\pi$-bond of the forth valence electron in the $2p_z$-orbital (Fig. 2.2). A conjugation, alternating single and double bonds between carbon atoms, is necessary to realize a small molecule (molecular mass $<$ 1000 g/mol) or a conjugated polymer with semiconducting properties. The transition from a single carbon-based molecule to a conjugated polymer is illustrated schematically in Fig. 2.2. The $sp^2$-hybrid orbitals of neighboring C-Atoms form covalent $\sigma$-bonds and therefore strongly localized electron densities without contribution to the charge transport. Besides, the overlap of adjacent $p_z$-orbitals forms two $\pi$-bonds resulting in a delocalized $\pi$-electron system in parallel to the hybrid orbital plane. The delocalization enables a quasi-free electron transport along the conjugation

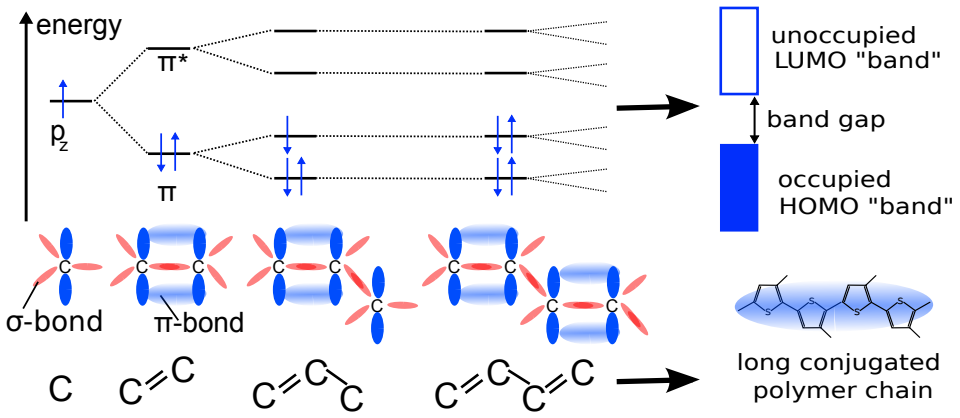


Figure 2.2: Transition from simple carbon $sp^2$-hybrid orbital with one $\pi$-electron in the $p_z$-orbital to a conjugated polymer with alternating single–double bonds and $\pi$-electrons smearing in energy, forming a HOMO energy band with binding and a LUMO energy band with anti-binding character. The semiconducting property stems from band gap formation due to the Peierls distortion [29]. Figure modified after [30, 31, 32].

length [20]. By the interaction of further carbon atoms several binding and anti-binding $\pi$-orbitals, slightly shifted in energy, become involved and two energy bands are formed. The one lower in energy, populated and with binding character, is denoted as the highest occupied molecular orbital (HOMO), and the one higher in energy, unpopulated and with anti-binding character, is called lowest unoccupied molecular orbital (LUMO). The Peierls distortion accounts for the slightly altering distances between neighboring carbon atoms and can be seen as the origin of the energy gap, required for the semiconducting character [29, 30].

## 2.3 Operating Principles in Organic Solar Cells

The architecture of an organic solar cell is depicted in Fig. 2.1 for PHJ (a) and BHJ (b) devices. Both start from a transparent conductive oxide, in our case indium tin oxide (ITO), deposited on a glass substrate. ITO is followed by a hole transporting layer (HTL) like PEDOT:PSS and the active material, in bilayer or blended configuration, respectively. The devices are finalized by a metal top contact, e.g. silver (Ag) or aluminum (Al) and sometimes with an additional interlayer such as calcium (Ca) for work function alignment. The crucial physical steps, (1) photon absorption and exciton generation, (2) exciton diffusion and dissociation, (3) polaron pair dissociation, (4) charge transport and (5) charge extraction at the contacts, to realize an efficient

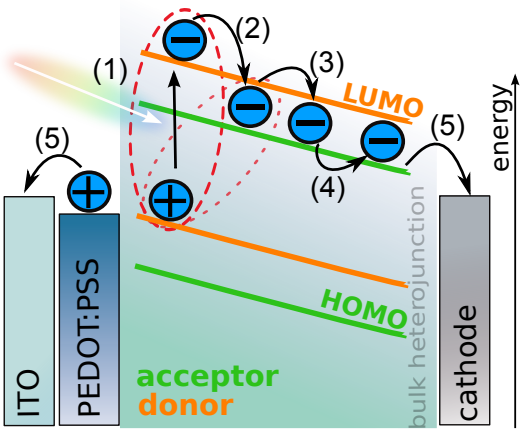


Figure 2.3: Scheme of the five crucial physical processes of an organic solar cell: (1) Photon absorption and exciton generation (2) Exciton diffusion to donor–acceptor interface and charge transfer (3) Polaron pair dissociation (4) Polaron transport (5) Charge extraction at the electrode.

energy converter are highlighted in the following and summarized in Fig. 2.3. For simplicity, only the blended donor–acceptor system is discussed, as the physical processes are almost identical in the bilayer configuration. For a detailed study on the differences between both device architectures I refer to the experimental results in Chapter 7.

### 2.3.1 Photon Absorption – Exciton Generation

Converting electromagnetic waves into photocurrent starts with the absorption of a photon. In contrast to their inorganic opponents, solar cells based on organic materials have high absorption coefficients. For example, CuPc as used in the first bilayer cell by Tang yields a peak extinction coefficient $k$ at 620 nm of 0.74, which results in an absorption of about 15% within only 10 nm layer thickness [33]. Typical active layer thickness of 100-200 nm for organic solar cells are sufficient to yield a satisfying absorption in the visible to near-infrared sun spectrum. Photon absorption predominantly occurs in the donor material and is equivalent to an excitation of an electron from the HOMO to the LUMO level (exciton generation). As already mentioned in Section 2.1 the exciton binding energy is rather high, usually between 0.5 eV and 1 eV. For example, the most prominent donor material in OPV, regioregular poly(3-hexylthiophene-2,5-diyl) (P3HT) yields an exciton binding energy of 0.7 eV [34]. The thermal energy at room temperature ($E_{th} \approx 26$ meV) is not sufficient to separate electron and hole to achieve a photocurrent. Therefore, an alternative and fast dissociation process is necessary to avoid a subsequent

radiative decay (and loss in photocurrent) of the exciton to its ground state after a lifetime $\tau$ of typically hundreds of ps to 1 ns [35, 36].

### 2.3.2 Exciton Diffusion & Dissociation

The distance covered by an exciton during its lifetime, the exciton diffusion length, is usually in the range of very few nanometers to about 20 nm in standard conjugated polymers, such as P3HT or PPV [36, 37], but can also exceed 65 nm in evaporated CuPc layers related to a higher degree of molecular order [37]. As briefly noted in Sec. 2.1, for a successful exciton dissociation the acceptor material with a stronger electron affinity must be within the diffusion length of the exciton to overcome its binding energy. For BHJ organic solar cells, the fullerenes $C_{60}$ and $C_{70}$ or for solution processed devices their soluble derivatives [6,6]-phenyl- $C_{61}/C_{71}$ butyric acid methyl ester ($PC_{61}BM/PC_{71}BM$) have proven to be the best acceptor choice so far. Once an exciton reaches a donor–acceptor interface, the electron is transferred to the acceptor molecule (charge transfer, CT) if this is energetically favorable, i.e. the gain in energy is larger than the exciton binding energy. The energy difference of the respective LUMO levels of both materials can be used as a rough estimation of this energy gain [34]. For the standard material combination P3HT:$PC_{61}BM$ the described charge transfer process is reported to take place in less than 120 fs [38, 24], which is considerably smaller than the exciton lifetime, and therefore very efficient. After a successful CT process, electron and hole reside on different molecules and are denoted as polaron pair in the charge transfer state. Due to their spatial separation and delocalization on respective molecules their binding energy is considerably weaker, which enables a thermal dissociation or a dissociation induced by the internal/external electric field.

### 2.3.3 Polaron Pair Dissociation

Understanding and analyzing the dissociation of a polaron pair—the intermediate step from a photogenerated exciton to free polarons—is one of the key problems in OPV, but still not fully understood. An early model to describe the separation of a Coulomb bound pair of ions with opposite charge was proposed by Onsager in 1938 [39]. An extended version, the Braun–Onsager model, accounting also for the finite lifetime of the initial bound state, was later on applied to study the electric field-assisted dissociation of charge transfer states in donor–acceptor systems by Braun [40]. The model is based on three transition rates: the decay rate of polaron pairs to the ground state $k_f$, the dissociation rate of polaron pairs to quasi free polarons $k_d$ as well as the

reverse transition of free polarons to polaron pairs $k_r$. It is noteworthy that in this model free polarons have to form a bound polaron pair with a finite residual dissociation probability before they may recombine to the ground state—a direct transition is forbidden. The respective transitions are summarized in Fig. 3.1 (a) and (b) resulting in a field-dependent polaron pair dissociation probability $P(F)$ of

$$P(F,T) = \frac{k_d(F,T)}{k_d(F,T) + k_f}, \tag{2.1}$$

with the electric field $F$ and the temperature $T$. The rate $k_d$ furthermore depends on the mobility $\mu$, the initial distance of electron and hole and the respective Coulomb binding energy [40, 41]. Nowadays, the Braun–Onsager model is the most commonly used model to describe polaron pair dissociation in OSC [42, 43, 44].

Nevertheless, the model describes a simplified situation as it does not include some aspects crucial for organic semiconductors, e.g. energetic disorder or high local charge carrier mobilities [45, 46]. However, the impact of high local charge carrier mobilities due to delocalized charge carriers along conjugated polymer chain segments was recently analyzed via Monte Carlo simulations by Deibel *et al.* [47]. Their findings of a dissociation yield up to 80% under an electric field of F$\approx 10^7$ V/m, realistic for standard OSC, agrees well with experimental data. Higher local mobilities might be due to partly crystalline regions within the predominately disordered donor or acceptor phase. Consequently, larger pure and well ordered phases of donor and acceptor can have a positive impact on polaron pair dissociation and device performance, which is contrary to a well intermixed and therefore disordered donor–acceptor blend system required to achieve a high exciton dissociation yield (see Sec. 2.3.2). This already indicates that the optimum donor–acceptor morphology to realize maximum device efficiency is always a tradeoff. On the one hand, a well intermixed donor–acceptor phase favors optimum exciton dissociation (charge transfer and polaron pair generation). On the other hand, partly crystalline and ordered donor–acceptor regimes lead to efficient polaron pair dissociation (free polarons). Aside the Braun–Onsager model other approaches exist such as the model of Petersen *et al.*, who introduced a field-dependent tunnel term to accurately account for the present field- and T-dependence of the polaron pair dissociation [48].

From literature it is known that there are material compositions, for example thermally treated P3HT:$PC_{61}BM$ blends, with voltage independent charge generation [49, 50, 51]. This might be related to the excess energy available after exciton dissociation ($\Delta$E=$LUMO_{donor}$-$LUMO_{acceptor}$) and was investigated intensively in the past [52, 53]. The issue of polaron pair dissociation being dependent on the electric field or not and its influence on the current–voltage

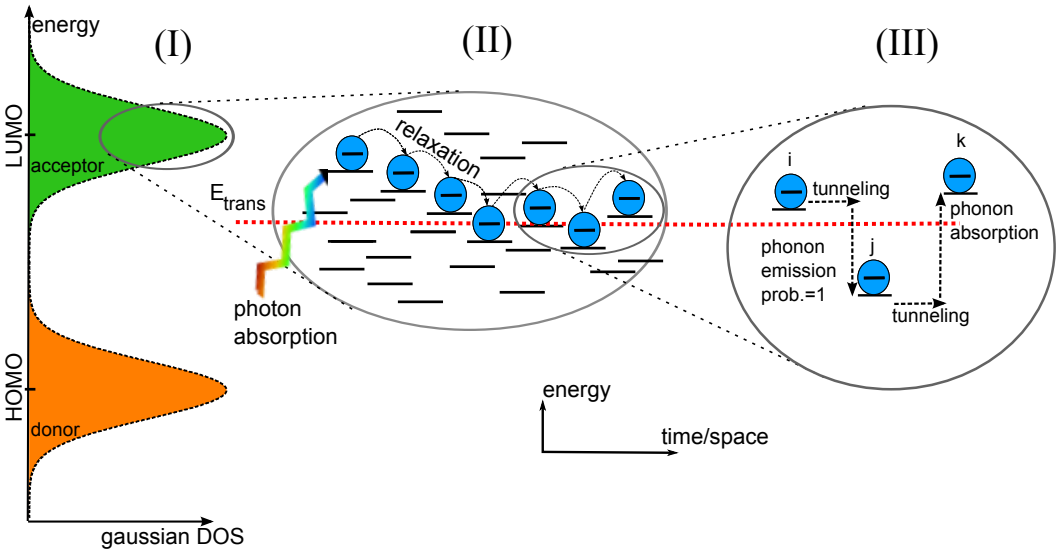


Figure 2.4: (I) Gaussian distributed HOMO level of the donor and the respective LUMO level of the acceptor niveau (II) energy relaxation of an excited electron via charge carrier hopping (III) charge transport from state $i$ over $j$ to $k$ based on hops around the transport energy via tunneling to overcome the spatial distance and thermally activated jumps to overcome energy barriers.

$(j/V)$ response of an organic solar cell will be further addressed in Sec. 3.1 and 3.3 as well as in Chapter 6.

### 2.3.4 Charge Transport

A successful polaron pair dissociation is followed by the transport of electron and hole (polarons) towards their respective electrode. Charge transport in disordered organic semiconductors essentially differs from the band transport known from crystalline inorganic semiconductors due to the absence of a three dimensional periodic lattice structure. In a classical inorganic semiconductor the electron wave functions delocalize over the entire crystal, leading to a quasi-free electron/hole transport within the conduction/valence band. Instead, organic semiconductors are characterized by a delocalization over single molecules, conjugated polymer segments or at the most partly crystalline regions and therefore in general yield rather localized states. This results in a fast (microscopic) charge transport along a conjugated polymer chain (intrachain transport) but limited transport between localized states due to their energetic and spatial disorder. Nevertheless, an occasional overlap between neighboring orbitals allows a charge transport between them, commonly de-

scribed by a hopping process of charges (inter-chain transport). In 1960 Miller and Abrahams presented a model to describe the hopping transport in inorganic semiconductors at low temperatures with localized states due to impurities [54]. The probability for a hop between an initially occupied state $i$ with energy $E_i$ and a nearby unoccupied state $j$ with energy $E_j$ is characterized by a tunneling term to overcome the spatial distance and a Boltzmann term for the energy difference $\Delta E = E_j - E_i$. In this model, known as *variable range hopping* (VRH) the emission of a phonon to account for the case $\Delta E < 0$ is always possible (probability=1) and thus hops downwards in energy are more likely than upwards. This directly leads to an energy relaxation process of free polarons initially occupying higher energetic states directly after polaron pair dissociation. The energy level where up and down hops are equally distributed is denoted as the transport energy $E_{trans}$ depicted in Fig. 2.4.

An important extension to the VRH model was introduced in 1993 by Bässler via Monte Carlo (MC) simulations. Predominantly based on photo absorption spectra he introduced a Gaussian density of states (GDOS) to discretize the energetic and spatial disorder of the localized states. The model is denoted as the Gaussian disorder model (GDM) with the hopping sites energy distribution $g(E)$ given by

$$g(E) \propto \exp\left(-\frac{E^2}{2\sigma^2}\right). \tag{2.2}$$

The energy $E$ is determined relative to the center of the density of states and the width of the distribution $\sigma$ is a parameter representing the degree of disorder [55]. Bässler used his simulations to analyze the charge transport and found a mobility $\mu$ depending on the temperature $T$, the disorder parameter $\sigma$ and the electric field $F$ according to

$$\mu(T, \sigma, F) \propto \exp\left[-\left(\frac{2\sigma}{3k_B T}\right)^2\right]\sqrt{F}, \tag{2.3}$$

which will be a matter of discussion in section 6.1.2. Furthermore, it was shown that the density of occupied states (DOOS) is Gaussian distributed and centered around equilibrium energy $E_{eq}$ below $E_{trans}$ (see Fig. 2.5).

An alternative way to describe the charge transport mechanism in disordered systems is the *multiple trapping and release* (MTR) model adopted from amorphous inorganic semiconductors. Introduced by Schmidlin [56], the model detaches from a hopping transport between localized sites. Instead, a band-edge-energy ($E_{trans}$) similar to the mobility-edge in inorganic semiconductors is defined, above which a quasi-free band-like transport like in crystalline systems with mobility $\mu_0$ is possible. The disorder of organics

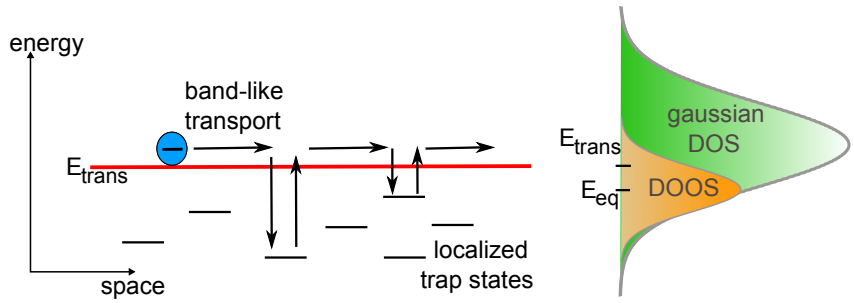


Figure 2.5: Scheme of the *Multiple Trapping and Release* principle: band–like transport above the transport energy $E_{\text{trans}}$ and immobile charges are captured in trap states below $E_{\text{trans}}$ until their release after a certain release time. The density of occupied states (DOOS) is embedded in the Gaussian density of states.

is represented by unoccupied states below $E_{trans}$ acting as trap states (see Fig. 2.5). Trapped and thus immobile charges can be thermally activated and released after a certain time, depending on their energetic position and the respective required activation energy. A direct transition between two trap states thereby is forbidden.

On their way towards the electrodes polarons of opposite charge may meet each other and annihilate. This loss mechanism can have a severe impact on device performance and is known as nongeminate recombination, which will be discussed in detail in Chapter 3.2. For a more extensive review on charge transport please see Refs. [55, 57, 58].

### 2.3.5 Charge Extraction

The final step to finish energy conversion from radiation to electric energy is the extraction of polarons at their respective electrode and release into the external circuit. If the rate of charge extraction via the electrode is too low, this may lead to charge accumulation near the contact resulting in a low fill factor and low performing devices. This was recently analyzed via macroscopic device simulations by using a reduced surface recombination to explain experimental current–voltage data [59].

The contact material plays an important role as its work function and the adjacent energy levels of the organic materials determine the charge injection/extraction barrier $\Phi$. Besides its influence on the extraction rate, the injection barrier $\Phi$ correlates with the open circuit voltage $V_{oc}$, discussed in details in Ref. [60].

Another performance limiting scenario is the extraction of electrons (holes) at the wrong electrode, respectively the anode (cathode) [61]. To avoid this

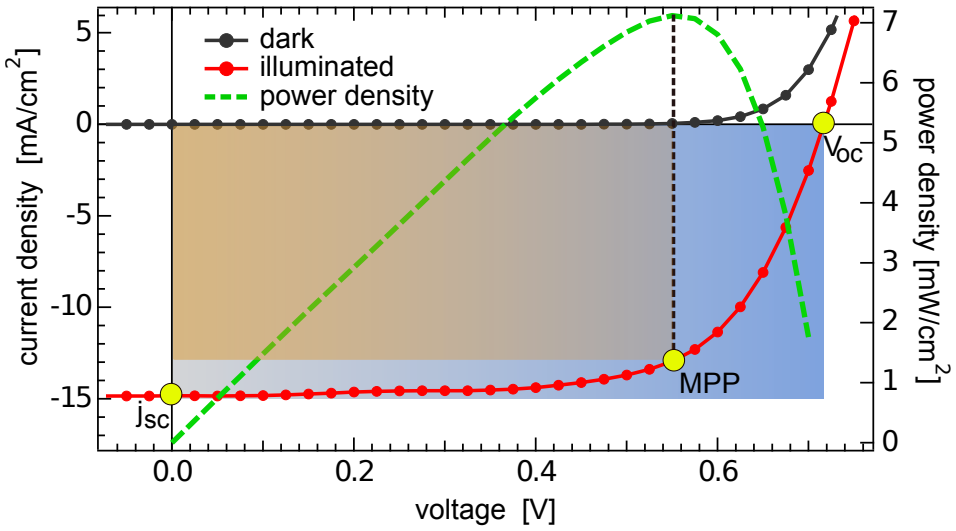


Figure 2.6: Dark and illuminated current–voltage characteristics of an organic solar cell based on the active material PTB7:$PC_{71}BM$. The green dashed line represents the power density with its maximum around 0.55 V. Marked in yellow, the point of maximum power (MPP), as well as the two characteristic parameters, the short circuit current density $j_{sc}$ and the open circuit voltage $V_{oc}$. The fill factor is defined via the ratio of the areas of the two rectangles (see text).

loss in photocurrent hole/electron transporting layers (HTL, ETL) are used as an interlay between the organic layer and the metal to create selective contacts. For more details on organic solar cells please see the concise reviews of Dennler *et al.* [62] or Deibel *et al.* [41, 63].

## 2.4 Current–Voltage characteristics

The quantity to describe the performance of a solar cell qualitatively is denoted as the solar cell efficiency $\eta$, defined by the ratio of maximum provided electrical power density $P_{max}$ to the incident light power density $\Phi_L$ (incident light power per area),

$$\eta = \frac{P_{max}}{\Phi_L}. \tag{2.4}$$

In order to investigate solar cell efficiency a current–voltage ($j/V$) characteristic is recorded under a given light intensity $P_L$. Exemplary dark and illuminated $j/V$ responses are depicted in Fig. 2.6, visualizing the characteristic parameters of a solar cell: the short circuit current density $j_{sc}$, the open circuit voltage $V_{oc}$ and the voltage which defines $P_{max}$, the maximum power

point $MPP$. The current density is defined by $j = I/A$ with the current $I$ through the active area $A$, to enable a comparison between cells of different active areas. The fill factor $FF$ is given by

$$FF = \frac{j_{MPP} V_{MPP}}{V_{oc} j_{sc}} \tag{2.5}$$

and is a quantity for diode-like rectification, represented in Fig. 2.6 by the ratio of the small (brown) and the big (blue) rectangle. The parameters $j_{MPP}$ and $V_{MPP}$ are defined by the maximum power point. The efficiency $\eta$ thus is

$$\eta = \frac{V_{oc} j_{sc} FF}{\Phi_L}. \tag{2.6}$$

To ensure comparable power conversion efficiencies among research groups standard testing conditions (STC) are defined by the International Electrochemical Commission. This standard yields a radiant density of 1000 W/m$^2$ of an AM 1.5G sun spectrum as well as a measurement temperature of 25°C. Thereby, the spectrum of the lamp providing the radiant power density plays an important role and must be considered carefully. Details how to accurately determine the efficiency can be found in Ref. [64].

Chapter 3

# Charge Carrier Recombination Dynamics

The annihilation of electron and hole, denoted as recombination of charge carriers, can have a severe impact on the device performance of an organic solar cell, which will be addressed in detail in Sec. 3.3. First of all, the main loss mechanisms are distinguished and explained. On the one hand, the so called geminate recombination process of excitons or still Coulomb bound electron–hole pairs (polaron pairs) in the charge transfer state is considered (see Sec. 3.1). On the other hand, the nongeminate charge carrier recombination is defined by electron–hole annihilation of quasi free polarons on their way towards the electrodes (see Sec. 3.2). Thus, nongeminate recombination occurs after a successful polaron pair dissociation and can therefore be distinguished from geminate processes by different decay dynamics and time scale.

## 3.1 Geminate Recombination

Upon photon absorption the strongly Coulomb bound exciton may undergo dissociation via a charge transfer of the electron from donor to acceptor. The so created polaron pair is still Coulomb bound and its dissociation process can be described by the Braun–Onsager model as noted in Sec. 2.3.3. If electron and hole decay to the ground state before they dissociate, this is denoted as geminate recombination and can lead to a voltage dependent charge generation. Thereby, the participating polarons originate from the same precursor state. Geminate recombination is specific to low mobility, low conductivity, typically disordered semiconductors [49] and usually occurs on a time scale up to a few ns [65, 66]. Geminate recombination scales linearly with light intensity as every absorbed photon creates one electron-hole pair. This is an important distinctive feature considering a differentiation with nongeminate recombination. The geminate recombination rate $R_{gem}$ is given by

$$R_{gem} = \frac{PP}{\tau_{PP}}, \tag{3.1}$$

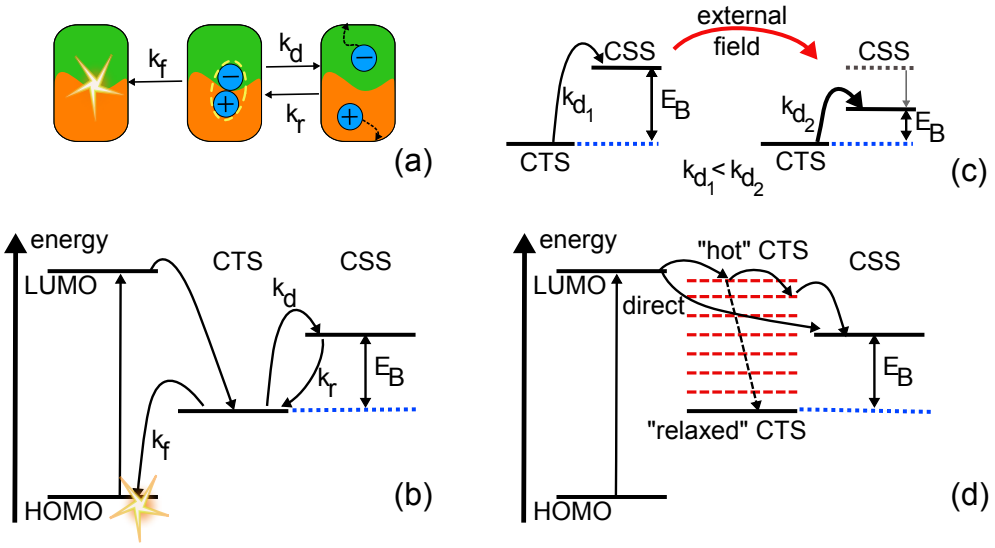


Figure 3.1: (a) A schematic description of polaron pair dissociation according to the Braun–Onsager model is given: dissociation occurs with the rate $k_d$, free charge carriers become a bound polaron pair again with the rate $k_r$ and the decay to the ground state takes place with the rate $k_f$. (b) Scheme of dissociation via a charge transfer state (CTS) energetically located below the charge separated state (CSS) and the possible transitions as described above. (c) An external electric field lowers the energy barrier $E_B$ and favors polaron pair dissociation ($k_d$ rises) (d) Direct dissociation or via a "hot" charge transfer state and thus negligible geminate recombination. Equivalent scenario to (b) if relaxation to the "relaxed" CTS is faster than the transition to CSS (dashed arrow). Figure in part similar to Ref. [53, 32].

with the finite lifetime of the polaron pair $\tau_{PP}$ and the polaron pair density $PP$. An energetic scheme of the relevant transitions is provided in Fig. 3.1 (b). A polaron pair occupying the relaxed (thermalized) charge transfer state (CTS) is created after photo excitation via ultrafast charge transfer [38]. The binding energy $E_B$ has to be overcome in order to realize a complete charge dissociation (charge separated state, CSS). The polaron binding energy $E_B$ strongly depends on the active material. For example, photoluminescence measurements on the well-known material system MDMO-PPV:$PC_{61}BM$ yielded a binding energy of $E_B \approx 200$ meV [67]. Hence, an externally applied electric field can be used to lower the energy barrier $E_B$ and facilitate a successful polaron pair dissociation (see Fig. 3.1 (d)). The Braun–Onsager model introduced in Sec. 2.3.3 theoretically describes this process while aside experimentally a strongly field-dependent charge generation for

MDMO-PPV:$PC_{61}BM$ devices was verified by time delayed collection field measurements [51]. Despite an existing binding energy of the polaron pair, a field-dependent charge generation is not necessarily present in organic solar cells, as shown recently for annealed P3HT:$PC_{61}BM$ devices [50, 51]. In this case, the binding energy $E_B$ can be overcome either by a direct transition from the LUMO state to the CSS or by a polaron pair dissociation via an excited ('hot') CTS within about 100 fs [33, 65, 53]. Both scenarios result in negligible influence of geminate recombination on the polaron pair dissociation yield and consequently lead to a voltage independent charge generation. This will be further addressed in Sec 3.3 and in Chapter 5 & 6.

## 3.2 Nongeminate Recombination

In contrast to geminate recombination the nongeminate recombination process is based on electron and hole from different precursor states. The participating, oppositely charged polarons originate from different photons but meet each other on their way towards the electrodes. The amount of charge in the device depends on the electric field as due to a field-induced current flow charges are transported into the external circuit. Thus, one expects nongeminate recombination being strongly dependent on the applied voltage due to its influence on the current flow and on the charge carrier density $n$ present in the device.

A well established model often used to describe nongeminate recombination in organic solar cells was introduced by Paul Langevin in 1903, and is now briefly explained [68].

### Langevin Theory

The original model by Langevin refers to recombination dynamics of two oppositely charged ions in a large reservoir [68]. Recombination occurs if two oppositely charged ions approach each other to a distance below the Coulomb capture radius, i.e. the distance $r_c$ of equal thermal and Coulomb binding energy. The recombination process itself is not the limiting factor, but the finding of electron and hole. This is a consequence of the low charge carrier mobility $\mu$ often observed in organic semiconductors .

The recombination rate given by the Langevin theory is

$$R_L = \gamma(np - n_i^2), \tag{3.2}$$

with the charge carrier densities for electrons $n$ and holes $p$, the intrinsic

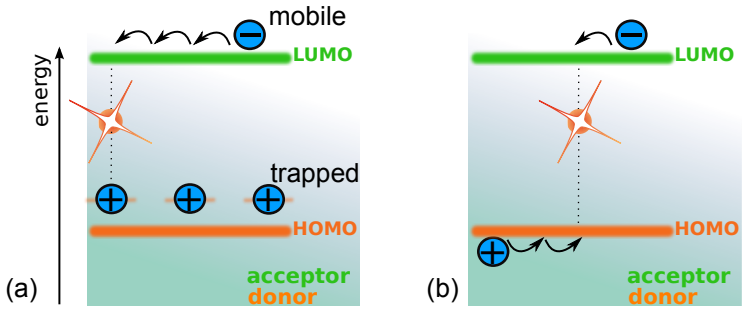


Figure 3.2: (a) Nongeminate recombination of a mobile and a trapped polaron often referred to as monomolecular recombination $\propto n$ (b) Nongeminate recombination of two mobile polarons yielding a recombination rate $\propto n^2$.

charge carrier density $n_i$ and the Langevin recombination prefactor $\gamma$ with

$$\gamma = \frac{q}{\varepsilon\varepsilon_0}(\mu_e + \mu_h), \tag{3.3}$$

where $q$ represents the elementary charge, $\varepsilon\varepsilon_0$ the effective dielectric constant and $\mu_e$ and $\mu_h$ the mobilities of electrons and holes. The requirement of a large reservoir is one critical property when the Langevin model is applied to organic bulk heterojunction solar cells. Two reservoirs, the donor and acceptor phase exist, while electron and hole transport are usually confined to different phases, which means recombination occurs mainly across the donor/acceptor interface. Consequently, in dependence on the active layer morphology, the preparation conditions and the organic materials itself, a deviation from the Langevin recombination is expected. For example, tempered cells based on the materials P3HT:$PC_{61}BM$ feature a clear donor–acceptor phase separation and yield a deviation of almost two orders of magnitude, represented in a reduction factor $\gamma$ while the difference for as-prepared cells with a fine donor–acceptor intermixing is much less [69].

Despite the possibility to calculate the Langevin recombination rate according to Eq. 3.2, which requires access to charge carrier mobility $\mu$ and density $n$, the nongeminate recombination rate is experimentally also given by

$$R_{nongem} = \frac{n}{\tau(n)} = k_\lambda n^{\lambda+1}, \tag{3.4}$$

with the lifetime of the charge carriers $\tau(n)$ in dependence on their density $n$ and the empirical recombination prefactor $k_\lambda$ as well as the recombination order $\lambda$. If not noted otherwise, Eq. (3.4) is used to calculate the nongeminate recombination rate. The required charge carrier lifetime is determined by transient photovoltage (TPV) measurements and the charge carrier density $n$ is accessible by a combination of TPV and transient photocurrent (TPC) as

well as by the so called charge extraction (CE) technique (see Chapter 4). The right hand side of Eq. (3.4) is a generalized expression for the recombination rate and enables to determine the recombination order $\lambda + 1$ [70].

In the past, studies on the recombination of organic BHJ solar cells dealt with the question whether the dominant recombination process was mono- or bimolecular [49, 71]. Within this approach, both mono- and bimolecular recombination refer to a nongeminate process, and are defined in terms of how the recombination rate scales with charge carrier concentration (monomolecular: R $\propto n^1$ with recombination order $\lambda + 1 = 1$, bimolecular: R $\propto n^2$ with recombination order $\lambda + 1 = 2$) [72]. The pure annihilation of two mobile polarons, as highlighted in Fig. 3.2 (b), leads to a nongeminate decay of second order. Aside, recombination of a mobile charge carrier and a trapped one yields a nongeminate decay of first order if $n_t \ll n_c$ with $n_t$, $n_c$ representing the density of trapped and mobile charge carrier densities. Thereby charges can either be trapped energetically in a state below $E_{trans}$ (see Fig. 3.2 (b)) or morphologically in a self-contained phase—both yielding an immobile charge carrier. In the latter case, the charge carrier would not be extracted in an experiment, as no connection to an electrode exists.

Recently, several groups reported on the recombination order $\lambda$+1 to be higher than two if determined by transient experiments on organic solar cells. The deviation from a quadratic decay order is commonly explained by the influence of trapped charge carriers [70, 73, 74]. Considering the MTR model, charges trapped ($n_t$) and not accessible by mobile counterparts ($n_c$) due to phase separation can be released after a certain time and participate delayed in the recombination process. Experimentally trapped charge carriers reduce the recombination rate and increase the apparent recombination order. The severe impact of nongeminate recombination as well as the influence of trapped charges will be a matter of interest in the experimental results (see Chapter 5 and Sections 6.1, 6.2).

## 3.3 Impact of Charge Recombination on the $j/V$ Characteristics

As discussed in Sec. 3.1, geminate recombination competes with a successful polaron pair separation and occurs on a time scale of 100 fs up to tens of nanoseconds, thus, directly limiting charge generation $G$. Besides, nongeminate losses of quasi-free polarons usually take place on a time range of hundreds of nanoseconds up to a few hundred micro seconds after photon absorption depending on the present charge carrier density, as stated above. Recently Shuttle *et al.* introduced a model to analyze the impact of geminate

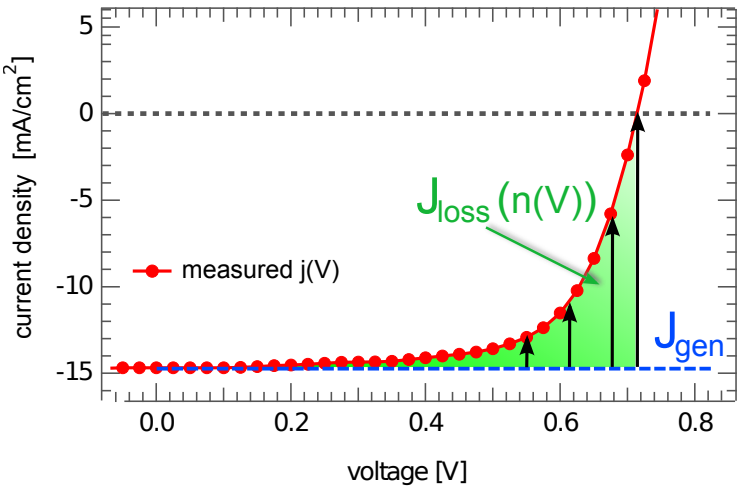


Figure 3.3: Schematic draft of $j/V$ reconstruction procedure: From the continuity equation in equilibrium Eq. (3.8) is derived, which enables to reconstruct measured $j/V$ characteristics by the determination of generation current $j_{gen}$ (blue dahsed line) and the loss current $j_{loss}$ (green area). In a first approximation $j_{gen}$ is assumed to be voltage independent, while $j_{loss}$ features a clear dependence on voltage (black arrows) present in $n(V)$. (after [76])

and nongeminate losses on the current–voltage ($j/V$) response of an organic solar cell [75]. It is based on the continuity equation representing the correlation between the microscopic dynamics discussed above and the macroscopic current–voltage behavior. In equilibrium, the continuity equation is given by

$$-\frac{1}{q}\frac{\partial j}{\partial x} + G - R = 0 \quad , \tag{3.5}$$

with the spatial deviation of the current density $\frac{\partial j}{\partial x}$ as well as the generation rate $G$ and the recombination rate $R$. Thereby, the generation rate is a product of the photon absorption and the charge separation efficiency and, thus, influenced by geminate losses being potentially voltage dependent. The rate $R$ is defined by nongeminate losses generally scaling nonlinearly with charge carrier density [70, 73, 75]. The idea of Shuttle *et al.* is based on the determination of $G$ and $R$ in the voltage range relevant for device performance and a subsequent reconstruction of measured $j/V$ curves. Integration of Eq. (3.5) enables to divide the current density $j$ into a generation current $j_{gen}$ and a loss current $j_{loss}$, defined according to

$$j_{gen} = -q\int_0^d G(x)dx \approx qd\overline{G} \tag{3.6}$$

and

$$j_{loss} = -q \int_0^d R(x)dx \approx qd\overline{R} \tag{3.7}$$

with the thickness of the active layer $d$. The assumption of spatially uniform generation $\overline{G}$ and recombination $\overline{R}$ is made requiring a rather uniform charge carrier density distribution $n(x) \approx \overline{n}$, as discussed recently [77]. The influence of possible charge density gradients on our analysis will be a matter of interest in the experimental results (see Chapter 6.2). Consequently, the integration of Eq. (3.5) leads to

$$j(V) = qd(\overline{G}(V) - \overline{R}(V)) = j_{gen}(V) - j_{loss}(n(V)), \tag{3.8}$$

while at the same time charge injection is neglected, as we focus on the voltage range between $V = 0$ V and $V_{oc}$. A schematic draft of the applied model based on Eq. (6.5) is shown in Fig. 3.3. In a first approximation, the generation is assumed to be voltage independent and, thus, constant over the voltages considered. To estimate the generation current $j_{gen}$ either the short circuit current density $j_{sc}$ is used for well rectifying diodes or hence the saturated photocurrent density under illumination in reverse direction (blue dashed line). The voltage dependence of $R$ and therefore of $j_{loss}$ stems from the voltage dependence of the charge carrier density $n(V)$, which is derived by the charge extraction technique (see Sec. 4.3). If the calculated current based on Eq. (3.8) coincides with the measured $j/V$ characteristics, one can draw two conclusions for the investigated system:

- geminate recombination can be neglected and the charge generation appears voltage independent.
- nongeminate recombination is identified as the major loss mechanism and limits current–voltage response.

If reconstructed and measured $j/V$ response do not coincide, either geminate losses have to be considered or the nongeminate recombination rate $R$, determined under open circuit conditions is explicitly dependent on the voltage (see discussion of Section 6.2).

Chapter 4

# Experimental

In the following chapters I will focus on the experimental part of my work and will highlight and describe the experimental techniques used during my studies. First, transient photovoltage (TPV) and transient photocurrent (TPC) are explained, which were used to probe the charge carrier lifetime after polaron pair dissociation and the charge carrier density under open circuit conditions in working solar cells. Afterwards, another powerful opto-electronic method, the charge extraction (CE) technique, is presented which enables to investigate the charge carrier density of operating devices in dependence on the applied voltage. Finally, the time delayed collection field (TDCF) technique to study geminate recombination is briefly introduced. All time-resolved transient measurements were performed in an optical closed-cycle helium cryostat (50-300K). The temperature was controlled by a Lakeshore 332 cryogenic temperature controller featured with two heater-sensors. In Fig. 4.1 the required hardware for the experimental setup and relevant connections are summarized. The chapter is finalized by a section on the organic materials used during this work and a paragraph on the device preparation of bulk heterojunction solar cells out of solution.

## 4.1 Transient Photovoltage (TPV)

Transient techniques such as charge extraction by linearly increasing voltage (CELIV) provide simultaneous access to charge carrier dynamics, i.e. charge carrier mobility and charge carrier density [78, 79]. However CELIV involves typically high intense, monochromatic laser excitation and non-equilibrium conditions. Instead, transient photovoltage is based on monitoring the photovoltage decay upon a small optical perturbation during various constant bias light conditions. TPV was applied to organic solar cells in 2008 for the first time [70]. To realize this quasi-equilibrium technique, the solar cell is connected to the high impedance input of a digital storage oscilloscope (Agilent Infiniium DSO90254A) via a high impedance ($\sim$1.5 G$\Omega$) voltage amplifier (customized FEMTO amplifier) to ensure open circuit conditions and no external current flow. A variable, constant bias light illumination is provided by a high power light emitting diode (LED) with 10 W electrical power (Seoul P7

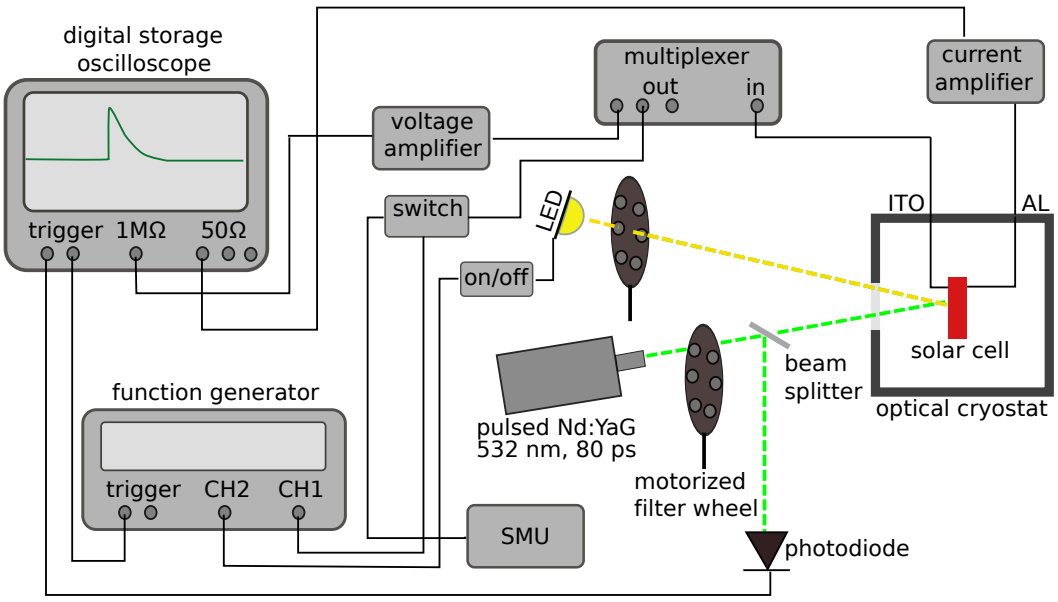


Figure 4.1: Schematic draft of the measurement setup for TPV, TPC and CE. For details on TDCF measurements see Ref. [32].

Emitter). There is a considerable spectral mismatch between the LED light source and the sun-simulator, used to pre-characterize the samples in the nitrogen glovebox. In order to realize comparable light intensity conditions for different devices, the source current of the LED $I_{LED}$ is set to a value where the test cell provides the identical short circuit current as under one sun conditions of the sun-simulator. This source current $I_{LED}$ is defined as the light intensity equivalent to one sun ($P_L = 1$ sun). The LED is supplied by a constant power source (Keithley2602) and the intensity is varied by the source current (linear dependence on light intensity, checked by Si-Photodiode) as well as additional neutral density filters to realize light intensities of about 0.01 of a sun to 3 suns.

Variable bias light intensities lead to a range of open circuit voltages $V_{oc}$ to be studied. In addition to the bias light a small optical perturbation ($\lambda = 532$ nm) is applied using a Nd:YAG (neodymium-doped-yttrium aluminium garnet) laser (EKSPLA PL-2210) with a pulse duration of about 80 ps. The additional amount of charges upon laser excitation leads to a rise in voltage $\Delta V_{oc}$. In order to ensure quasi-equilibrium conditions the laser intensity is well attenuated by neutral density filters to meet the requirement, that the change in voltage holds $\Delta V_{oc} \ll V_{oc}$. As no current flow is possible, the subsequent voltage decay directly monitors nongeminate charge carrier recombination. Shuttle *et al.* verified by a direct comparison with transient

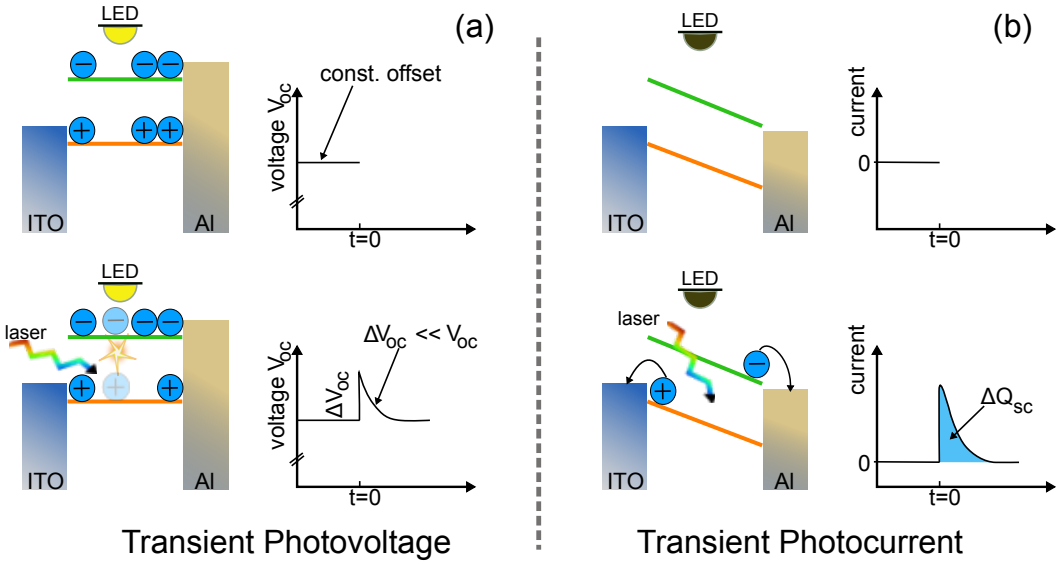


Figure 4.2: (a) Transient photovoltage is based on open circuit conditions of the solar cell and a constant bias light (LED) generating a constant voltage offset. No charge flow is observed due to the absence of an internal field. At $t = 0$ a 80 ps laser pulse generates additional charges, which lead to rise in voltage ($\Delta V_{oc}$). The subsequent voltage decay directly monitors the recombination of charges and enables the determination of the charge carrier lifetime $\tau_{\Delta n}$, as an external current flow is suppressed. (b) No background illumination is required for transient photocurrent. Thus, no current is detected prior to the laser pulse at $t = 0$. The blue area underneath the current transient represents the amount of charge $\Delta Q_{sc}$ added to the device by the laser pulse.

absorption measurements that the photovoltage decay is indeed a measure of polaron density [70] instead of an alternative process like dielectric relaxation [80]. Within the small-perturbation regime, the photovoltage transient can be well described by a single exponential decay and the small-perturbation charge carrier lifetime $\tau_{\Delta n}$ is derived in dependence on the respective open circuit voltage due to the constant background illumination. One can thereby assume,

$$\frac{d\Delta V_{oc}}{dt} \propto \frac{d\Delta n}{dt} = k\Delta n = -\frac{\Delta n}{\tau_{\Delta n}} \tag{4.1}$$

with the time $t$, the change in charge carrier density $\Delta n$ and the recombination prefactor $k$, which leads to the observed exponential charge decay

$$\Delta n(t) = \Delta n_0 \exp\left(-\frac{t}{\tau_{\Delta n}}\right) \tag{4.2}$$

and the measurable respective voltage decay to the ground level $V_{oc}$,

$$V_{oc}(t) = V_{oc} + \Delta V_{oc} \exp\left(-\frac{t}{\tau_{\Delta n}}\right) \quad . \tag{4.3}$$

One assumes that charge recombination starts at time zero after charge separation. Thus the peak voltage of the transient underestimates the change in voltage $\Delta V_{oc}$ due to incurred charge losses during the development of the voltage signal. For this reason the change in voltage $\Delta V_{oc}$ is determined by Eq. (4.3) and the respective fit on the TPV signal [81]. However, in order to study total charge carrier dynamics not only $\Delta n$ is necessary but also information on the charge carrier density $n$ in total.

## 4.2 Transient Photocurrent (TPC)

The determination of the steady-state carrier concentration $n$ under open circuit conditions requires a combination of both techniques, transient photovoltage and transient photocurrent and a procedure denoted as differential charging. Thereby the differential capacitance $C$ is given by the voltage rise $\Delta V_{oc}$ when a small amount of charge $\Delta Q_{sc}$ is added to the device,

$$C = \frac{\Delta Q_{sc}}{\Delta V_{oc}} \quad . \tag{4.4}$$

The voltage transient described above provides information on $\Delta V_{oc}$ and an additional photocurrent transient under short circuit conditions is recorded with an identical laser pulse to determine $\Delta Q_{sc}$. The TPC signal is measured either in the dark or at low bias light illuminations to minimize recombination losses for a correct determination of $\Delta Q_{sc}$. By the variation of the background illuminations the offset voltage $V_{oc}$, as well as the voltage change upon laser excitation $\Delta V_{oc}$, are varied and thus a dependence of $C$ on the open circuit voltage $V_{oc}$ becomes evident. Integrating the capacitance with respect to the voltage yields the desired charge carrier density $n(V_{oc})$ under open circuit conditions

$$n(V_{oc}) = \frac{1}{Aqd} \int_{-\infty}^{V_{oc}} C(V_{oc}) dV, \tag{4.5}$$

with active area $A$ and thickness $d$. For a correct determination of $n$ some important aspects have to be considered:

- Charge losses due to recombination during the current transient are neglected.

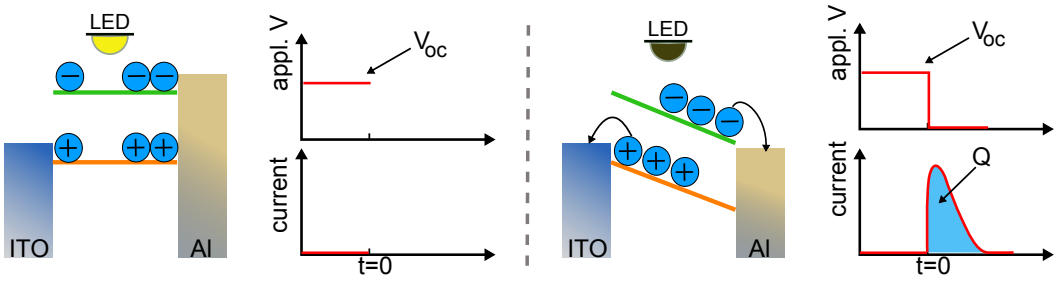


Figure 4.3: Scheme of charge extraction experiment: For $t < 0$ the LED provides constant bias light while the device is kept under open circuit conditions externally, which leads to rather flat bands and suppressed external current. Therefore under equilibrium conditions charge generation equals charge recombination. At $t = 0$ the LED is switched off while simultaneously the device is shorted and a current transient can be measured. The area underneath the transient represents the charge stored in the device and enables to calculate the charge carrier density $n(V_{oc})$ stored in the device under open circuit conditions.

- The capacitance values are corrected for the geometric capacitance $C_{geo}$, either estimated from $C_{geo} = \varepsilon\varepsilon_0 \frac{A}{d}$ or from charge extraction measurements in the dark (see Sec. 4.3).

- The parameters $\Delta V_{oc}$ and $\Delta Q_{sc}$ are determined under different conditions, i.e. open and short circuit conditions, which implies differences in the internal electric field.

To receive reliable results of the carrier density, the differential charging approach requires a charge carrier generation independent of the electric field. Otherwise under short circuit conditions more charges would be generated than under the same optical excitation under open circuit conditions, falsifying the determined capacitance. This is the main drawback of the TPV/TPC measurement, as for unknown systems based on new material compositions, a voltage dependent generation can not be excluded. An alternative way which overcomes this handicap is the charge extraction technique described in the following.

## 4.3 Charge Extraction (CE)

The charge extraction technique is applied to solar cells to investigate the charge carrier density $n$ under a certain illumination at any desired voltage.

For the sake of simplicity in the following detailed description, as well as in the scheme of the measurement procedure in Fig. 4.3 only CE transients under open circuit conditions are considered. Measurements apart of $V_{oc}$ were carried out likewise, while the voltage has to be corrected for the series resistance $R_s$, described in detail in Sec. 6.1.3.

A typical CE experiment under open circuit conditions begins with the choice of illumination realized by the same light emitting diode and identical light intensity calibration, as described in Sec. 4.1. The illuminated current–voltage characteristics are recorded via a source–measure–unit (Keithley 2602) to identify the open circuit voltage. Regarding the CE experiment, this voltage value is applied to the solar cell, while at the same time the LED provides the identical light intensity as used during the $j/V$ measurement. Thus, the device is kept under open circuit conditions, where no current flow can be detected via the digital storage oscilloscope and the generation equals the recombination ($G = R$). The externally applied voltage is supplied to the solar cell by a Keithley 2602 in combination with a fast digital/analog switch. In the next step, the LED bias light is switched off (intrinsic LED turn on/off times less than 200 ns) via a high power transistor (response time of ∼215 ns is considered). Synchronized via a double pulse generator (Agilent 81150A) the solar cell is simultaneously brought to short circuit by the digital/analog switch (response time ∼80 ns). The current transient is amplified by a FEMTO DHPCA-100 current–voltage amplifier and detected via a digital storage oscilloscope (Agilent Infiniium DSO90254A). The charge carrier density $n_{total}$ is obtained from extracted charge $Q_{total}$ defined by the integration of the current transient with respect to the time,

$$n_{total} = \frac{Q_{total}}{Aqd} = \frac{1}{Aqd} \int_{t=0}^{t_{stop}} I(t)dt\cdot \tag{4.6}$$

The time $t_{stop}$ depends on the active materials, the temperature and the light intensity and is defined by $I(t_{stop}) \approx 0$. It has to be noted that the total charge $Q_{total}$ is the sum of photogenerated charges in the bulk volume $Q_{bulk}$ and a considerable amount of capacitive charges residing on the electrodes $Q_{geo}$. Consequently, a study of bulk charges requires a geometric capacitance correction. This is realized by a range of CE measurements in the dark and in low reverse direction ($-0.05$ V$< V_{appl} < -0.3$ V), where charge injection is negligible and the signal is dominated by electrode charging. In this voltage range the charge $Q_{geo}$ depends linear on the voltage, $Q_{geo} = C_{geo}V$ with the geometric capacitance of the device $C_{geo}$. To account for the capacitive charges, the dark signal in reverse direction is upscaled to the voltage applied during the CE transient and is deducted from the detected original signal.

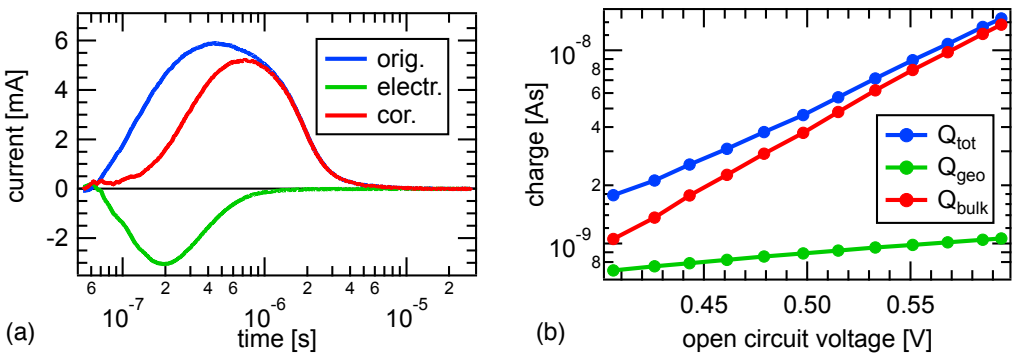


Figure 4.4: (a) Original transient data measured on a P3HT:$PC_{61}BM$ solar cell in blue, and the corrected data (red), which accounts for the electrode charge contribution, determined via CE transient recorded in reverse direction in the dark (green) (b) Impact of the electrode correction on the determined $Q(V_{oc})$ dependence: marginal influence for high light intensities (high open circuit voltages), but change in slope becomes apparent.

Thus, the desired charge carrier density of bulk charges is given by

$$n_{bulk} = \frac{Q_{total} - Q_{geo}}{Aqd} \tag{4.7}$$

and the required signal correction are exemplarily shown in Fig. 4.4 (a), while the impact of the electrode correction on the $Q(V_{oc})$ dependence is presented in Fig. 4.4 (b).

## Recombination losses during Extraction

After this necessary correction for the electrode charge the charge carriers lost due to recombination during extraction have to be accounted for. To this end, an iterative procedure with the number of cycles $j$ as described by Shuttle *et al.* is used [82]. In the following the main steps are briefly noted. The CE transients at $V_{oc}$ are chosen, beginning with the lowest illumination intensity. First of all, the charge density $n_{dev,j}(t_i)$ stored in the device at a certain time step $t_i$ is calculated for cycle $j = 0$ by

$$n_{dev,j}(t_i) = n_{bulk,j}(t_{stop}) - n_{bulk,j}(t_i), \tag{4.8}$$

with discretized time values $\Delta t = t_{i+1} - t_i \leq 1$ ns and $n_{bulk,j}(t_i)$ representing the extracted bulk charge (corrected for the capacitive contribution) at a certain time step $t_i$. The recombination dynamics $R(n)$ under open circuit

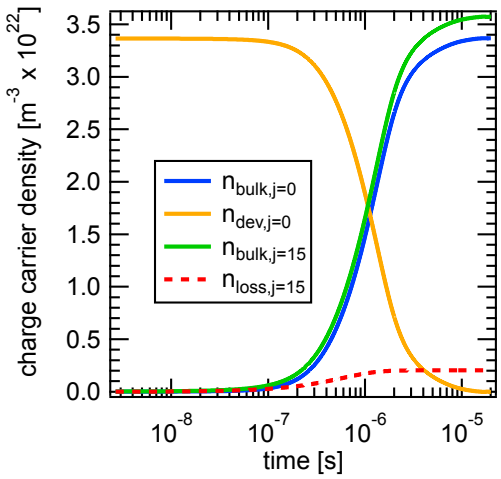


Figure 4.5: Experimental CE-transient of a P3HT:$PC_{61}BM$ (annealed) cell under 1 sun (blue) and the the corrected signal (green), where recombination losses during charge extraction are accounted for. The dashed red line refers to the sum of iteratively determined losses while the orange signal is calculated by Eq. (4.8) and represents the charge carriers in the device at a certain time $t_i$ at the beginning of the iterative procedure.

conditions determined before via a combination of TPV and CE measurements is set as $R(n_{dev,j})$ and enables to estimate the loss of charges due to recombination $n_{loss,j}(t_i)$ within the time span $\Delta t$,

$$n_{loss,j}(t_i) = R(n_{dev,j}(t_i))\Delta t \cdot \tag{4.9}$$

The total amount of losses within the first cycle $j = 0$ is then given by

$$n_{loss,j} = \sum_{t=0}^{t_{stop}} n_{loss,j}(t_i), \tag{4.10}$$

and is used for a first correction:

$$n_{bulk,j+1}(t_{stop}) = n_{bulk,0}(t_{stop}) + n_{loss,j} \ . \tag{4.11}$$

Before the procedure is repeated with $j$ increased by 1, all initial densities for the different light intensities are corrected once and the resulting new charge carrier densities are used to re-evaluate an updated recombination rate $R(n_{dev,j+1}) = \frac{n_{dev,j+1}}{\tau(n_{dev,j+1})}$ according to Eq. (3.4). The whole process is repeated for several iterations $j$ until the calculated losses are convergent, $n_{loss,j} - n_{loss,j-1} \to 0$. This is typically the case after 4-5 runs, but to ensure a

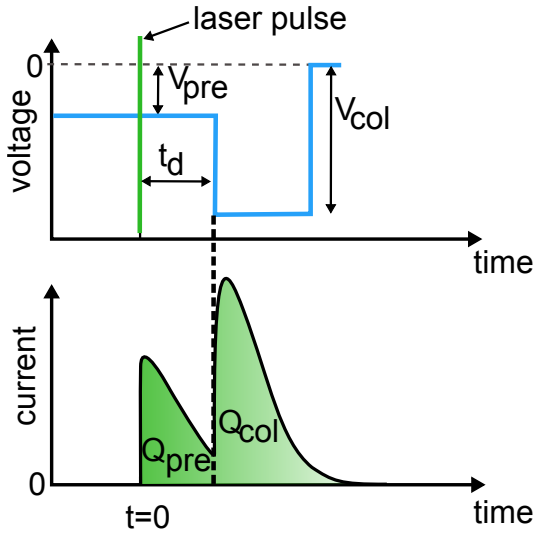


Figure 4.6: Top: Applied voltage during a TDCF measurement; Bottom: exemplary TDCF signal, featuring the prebias charge $Q_{pre}$ during the delay time $t_d$ and the collection charge $Q_{col}$ after $t_d$.

convergence in any case 15 runs were usually done. An exemplary correction can be seen in Fig. 4.5, where an illumination of one sun was chosen and the deviation between measured and corrected charge carrier density was in the range of 6%. The influence of losses during charge extraction strongly depends on temperature and light intensity, but was generally considered for all data points if not specifically noted otherwise. After a successful correction of the carrier densities $n(V_{oc})$ determined under open circuit conditions the precise recombination dynamics $R(n)$ is known. In the following data from voltage dependent densities $n(V)$ determined apart from $V_{oc}$ is iteratively corrected with the same procedure but with a fixed dynamic $R(n)$.

## 4.4 Time Delayed Collection Field (TDCF)

In this thesis the time delayed collection field technique is used to study the influence of geminate recombination in organic solar cells. The technique is over 30 years old and was originally applied to inorganic devices [83], but later also used to study solar cells based on organic materials [84, 50, 51]. Next to geminate processes, the technique enables to investigate nongeminate recombination or to determine charge carrier mobilities. However, in the following only the features relevant for this work are highlighted and for a more detailed description see Ref. [32]. In Fig. 4.6 a scheme of a TDCF measurement is shown. At the top, the voltage applied by a double pulse generator

is depicted while the recorded current signal (below) is detected via the 50 Ω input of a digital storage oscilloscope from Agilent. During photo excitation realized by a Nd:YAG laser in a ps-time range, the pre-bias voltage $V_{pre}$ is applied to the device continuously (for details on equipment see Sec. 4.1 and Fig. 4.1). Thereby, $V_{pre}$ defines an internal electric field $F_{device}$ present within the device during photon absorption according to

$$F_{device} \approx \frac{V_{bi} - V_{pre}}{d}, \tag{4.12}$$

with the built-in potential $V_{bi}$ usually approximated by the open circuit voltage $V_{oc}$. Consequently, a variation of $V_{pre}$ leads to a variation in the electric field $F_{device}$ and enables to study the influence of $F_{device}$ on the charge generation process after photon absorption. The total charge $Q_{tot}$ can be seen as a sum of the prebias charge $Q_{pre}$ and the collection charge $Q_{col}$, defined via integration over the current transient with respect to the delay time $t_d$. The delay time must be chosen carefully (typically $t_d \leq 100$ ns) to ensure that the charge generation process via a possible CT-state is finished, but nongeminate losses of already separated charges can be neglected. If the active material features a field-dependent charge generation, a certain electric field during the delay time $t_d$ is required to separate all polaron pairs and consequently the total charge $Q_{tot}$ will depend on the applied voltage $V_{pre}$ (see Sec. 6.2). To minimize the impact of nongeminate recombination and realize a fast charge extraction the collection voltage $V_{col}$ in reverse direction is typically set to $V_{col} \leq -4$ V. Besides the choice of the delay time $t_d$ other parameters like the laser intensity and the choice of $V_{col}$ are essential to obtain reliable results, which is explained in details in Ref. [32].

## 4.5 Organic Materials

The rapid development and the extensive research in the field of organic photovoltaics in the last 10 years lead to a great variety of organic materials featuring a various range of different optical and electrical properties. A typical classification refers to their electron affinity differentiating between donor and acceptor materials.

### Donor materials

My experimental work in the lab offered the possibility to examine and test several donor materials upon their ability to serve as an organic photoactive material. Within this thesis however, I focus on only three donor materials in combination with one respective acceptor (see below).

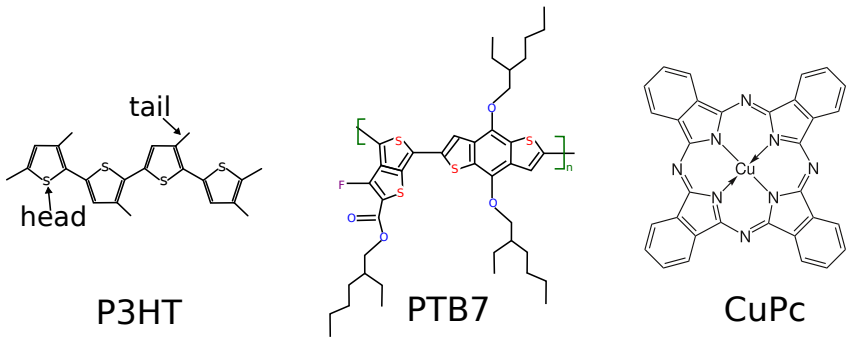


Figure 4.7: Donor materials used in this work: the extensively studied polymer P3HT (left), the rather new low band gap polymer PTB7 (middle) and the small molecule CuPc (right).

Photon absorption takes predominately place within the donor material. Two of the donors are polymers, the extensively studied and widely spread poly(3-hexylthiophene) (P3HT) and the promising, rather new, low band gap polymer Poly[[4,8-bis[(2-ethylhexyl)oxy]benzo[1,2-b:4,5-b]dithiophene-2,6-diyl][3-fluoro-2-[(2-ethylhexyl)carbonyl]thieno[3,4-b]thiophenediyl]] (PTB7), both typically prepared out of solution (see Sec. 4.6).

One monomer of P3HT, the most prominent donor material in OPV, consists of a thiophene ring (head) and an attached hexyl side chain (tail) to ensure solubility. Alternating head-to-tail arrangements of several monomers creates a polymer, where the regioregularity (RR) represents the percentage of perfectly alternating head-to-tail orientation (see Fig. 4.7 left). In this study we used P3HT purchased from Rieke metals, named P200 with a RR$\geq$ 95% and an absorption in the range of 450 to 650 nm. The thermal treatment of cells based on P3HT combined with $PC_{61}BM$ (see below) leads to the development of crystalline domains, visible in XRD measurements [85], an improved charge transport [86] as well as device performance [87].

Instead, the rather new polymer PTB7 (supplied by 1-material) features a higher absorption range up to 750 nm due to a lowered band gap of $E_g \approx$ 1.85 eV. Consequently, PTB7 yields an improved photon harvesting and higher photocurrents than P3HT for example. The rather complex structure of PTB7 can be seen in Fig. 4.7 (middle). Introduced in 2010, first cells based on PTB7:$PC_{71}BM$ yielded efficiencies of 7.4% [88]. In first glance, XRD studies revealed predominately amorphous domains within the PTB7:$PC_{71}BM$ bulk, surprisingly [89].

Finally, for a direct comparison between the two major solar cell architectures, planar and bulk heterojunction (see Chap. 7), a small molecule named copper-phthalocyanine (CuPc) was used (see Fig. 4.7 (right)). CuPc yields

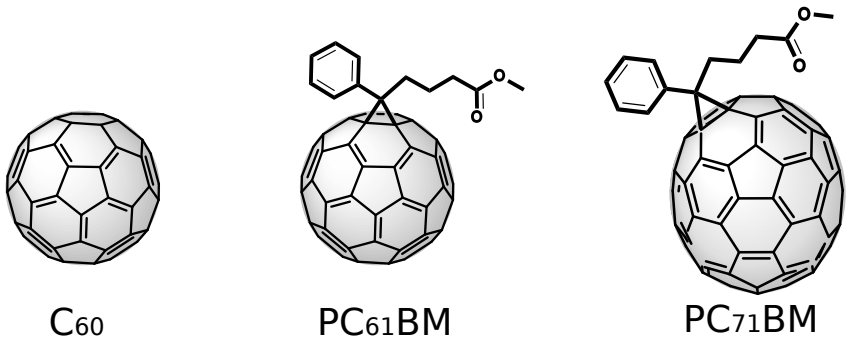


Figure 4.8: Acceptor materials used in this work: the fullerene $C_{60}$ (left), and its soluble derivatives $PC_{61}BM$ (middle) and $PC_{71}BM$ (right).

its maximum absorption between 580 and 720 nm [37] and is processed by thermal evaporation, which enables to realize planar and bulk configuration. CuPc was purchased from Sigma Aldrich and was purified at least once, using thermal gradient vacuum sublimation.

## Acceptor materials

Compared to their respective donor, the acceptor materials are strongly electronegative, which is necessary to guarantee a fast and efficient electron transfer from the donor to the acceptor molecule. Despite an extensive research for new acceptor materials, the spherical fullerene $C_{60}$ (see Fig. 4.8 left) and its derivatives are the most commonly used organic acceptor materials since almost 20 years. $C_{60}$, consisting of 60 carbon atoms forming a football like cage, is only poorly soluble in typical organic solvents and is therefore thermally evaporated together with CuPc. A soluble $C_{60}$ acceptor derivative is realized by adding a side chain (see Fig. 4.8, middle) denoted as [6,6]-phenyl-$C_{61}$butyric acid methyl ester ($PC_{61}BM$). In order to improve the weak absorption of $PC_{61}BM$, an asymmetric configuration of 70 carbon atoms leads to a molecule called [6,6]-phenyl-$C_{71}$butyric acid methyl ester ($PC_{71}BM$), which is depicted in Fig. 4.8, right. It features a higher absorption in the visible range [90, 91]. $C_{60}$ was purchased from SES-reasearch and purified at least once, using thermal gradient vacuum sublimation while $PC_{61}BM$ (purity 99.5 %) and $PC_{71}BM$ were purchased from Solenne and used without further purification.

In this work, solar cells based on P3HT:$PC_{61}BM$, PTB7:$PC_{71}BM$ as well as CuPc:$C_{60}$ and CuPc/$C_{60}$ are studied, whereas preparation conditions can play an important role, as noted in the following.

## 4.6 Device Preparation

In the framework of this thesis two totally different device structures are relevant. The bilayer configuration, shown in Fig. 2.1(a) and the bulk heterojunction structure illustrated in Fig. 2.1(b). In our own labs we are focused on processing out of solution typically favored to produce intermixed donor–acceptor (blend) systems, while bilayer configurations usually are deposited by thermal evaporation. Thus, for the bilayer preparation we cooperated with the Interuniversity Microelectronics Centre (IMEC) in Belgium and the preparation details will be addressed in Chapter 7. Consequently in the following I will sum up the details for bulk heterojunction devices processed out of solution only.

As already noted, the standard structure of BHJ devices is depicted in Fig. 2.1(b). Starting point of every processing run is an indium tin oxide (ITO) coated glass substrate, which was structured by lithography based on wet chemical etching prior to device preparation. The ITO was purchased from Präzisions Glas & Optik GmbH, CEC010S and yielded a sheet resistance lower than $10\Omega/\square$. To ensure reproducible and high quality device performance a proper substrate cleaning is essential. All substrates are mechanically cleaned in soap water and run through a 10 min ultrasonic bath in soap water, acetone and isopropyl alcohol afterwards. Then a 35-40 nm thick hole transport layer of poly(3,4-Ethylendioxythiophen):poly(Styrensulfonat) (PEDOT:PSS) from CLEVIOS (AI4083) is deposited by spin-coating to achieve a selective anode contact. Afterwards the substrates are transferred into a two chamber glovebox (GB) system with nitrogen atmosphere, where all subsequent steps are carried out to avoid contact of the organic materials with oxygen and water. To remove residual water the substrates covered with PEDOT:PSS are heated for 10 minutes at 130°C inside the GB. Thereafter, the active layer is deposited by spin-coating from a solution of a donor–acceptor blend. Typical organic solvents like chlorobenzene or ortho-dichlorobenzene are used to dissolve the organic semiconductors. Some special donor–acceptor compositions require a second solvent to improve later on device performance, which is denoted as solvent additive, i.e. diiodooctane, but is explicitly noted in the respective section of the results. The material concentration and the choice of spin speed parameters is crucial to obtain the favored active layer thickness. The layer deposition is optionally followed by a heating step, to influence the active layer morphology by thermal activation energy. The so called annealing is for instance applied to improve cell efficiency of P3HT:$PC_{61}BM$ cells but not beneficial for cells based on PTB7:$PC_{71}BM$ and is specifically noted if applied to the devices. Finally, the metal cathode, typically consisting of a 3 nm calcium layer and a 120 nm aluminum layer is thermally evaporated in an adjacent

ultra high vacuum chamber, with an average pressure $p < 10^{-6}$ mbar.

Basic device characterization by current–voltage measurements under a solar simulator took place directly after sample preparation in the second chamber of the glovebox system to prevent any influence of oxygen and water on the devices. All subsequent transient opto-electronic measurements (TPV, TPC, CE, TDCF) and light intensity dependent $j/V$ characteristics as well as temperature dependent studies were preformed in an optical cryostat. During the transfer the devices were briefly exposed to ambient air.

Chapter 5

# Shockley Equation Parameters by Transient Experiments

In this chapter, organic solar cells based on the well-known reference material system P3HT:$PC_{61}BM$ are intensively investigated by static current–voltage ($j/V$) characteristics, as well as transient photovoltage (TPV) and transient photocurrent (TPC) measurements in a temperature dependent study. First, the Shockley Equation (SE), originally derived to describe an inorganic p–n junction, is used to determine the SE parameters, i.e. the ideality factor and the dark saturation current, from the $j/V$ measurements. It is shown, that these parameters are directly related to charge carrier recombination and become accessible by TPV and TPC in the case of field-independent charge generation. In the second part, the ideality factor is linked to recombination of free with trapped charge carriers in an exponential density of tail states. Parts of this chapter are published in Paper 3.

## 5.1 Introduction

The polaron recombination dynamics fed into the continuity equation have been shown to deliver sufficient information to reproduce the complete $j/V$ response of P3HT:$PC_{61}BM$ solar cells at room temperature [75] which will also be a matter of interest in Chapter 6. However, in the present chapter an extension on the work of Maurano *et al.* [92] is provided, who combined parameters obtained by static ($j/V$) and transient photovoltage / transient photocurrent (TPV/TPC) methods in the Shockley equation [93]. In order to justify the validity of this approach and/or its limitations, in the following the ideality factor and dark saturation current density derived by static and transient measurements on P3HT:$PC_{61}BM$ OSC in the temperature range from 200 to 300 K at various light intensities are directly compared. The photocurrent is reproduced and the work of Kirchartz *et al.* [72], is prolonged by a detailed analysis of the impact of charge carrier recombination on the ideality factors.

## 5.2 Theoretical Background

The established model to describe the current–voltage response of semiconductor p–n junctions under illumination is based on the ideal SE,

$$j(V) = j_0 \left( \exp\left( \frac{qV}{n_{id}kT} \right) - 1 \right) - j_{gen}, \tag{5.1}$$

with dark saturation current $j_0$, elementary charge $q$, ideality factor $n_{id}$, thermal energy $kT$ and the photogenerated current $j_{gen}$ [93]. Conventional p–n junctions are characterized by well developed energy bands where photogeneration yields delocalized charge carriers. In contrast, OSC are based on excitonic materials, in which the photogeneration of quasi free polarons upon photon absorption is via bound precursor states and strongly depends on the active material. Furthermore, BHJ devices consist of donor and acceptor material phases across the whole volume, resulting in many spatially distributed heterojunctions instead of a single planar one.

Despite these differences to inorganic p–n junctions, the SE was successfully applied to organic solar cells based on different donor–acceptor systems in the past [94, 95]. Its application to devices based on MDMO-PPV:$PC_{61}BM$ [96] failed due to voltage dependent photocurrent generation $j_{gen}(V)$. For OSC based on P3HT:$PC_{61}BM$, used in this work, the polaron pair dissociation is reported to be independent [65, 50, 92] or weakly dependent [97, 47, 51] on voltage, providing a good starting point for the following analysis. For simplicity, an ideal diode was assumed in this study, neglecting any series resistance ($R_s = 0$) or leakages by shunts ($R_p = \infty$). No significant influence on the data was found by taking a series resistance into consideration, which was experimentally determined from the ohmic range of dark $j/V$ characteristics. Eq. (5.1) solved for $V_{oc}$ at a given light intensity with $j(V_{oc}) = 0$ and for $j_{gen} \gg j_0$ results in

$$V_{oc} = n_{id}\frac{kT}{q} \ln\left( \frac{j_{gen}}{j_0} + 1 \right) \tag{5.2}$$

$$\approx n_{id}\frac{kT}{q} \ln\frac{j_{gen}}{j_0}. \tag{5.3}$$

In order to experimentally access the photogenerated charges by $j/V$ measurements, a voltage independent generation current $j_{gen}$ is assumed.

## 5.3 Device Preparation & Measurements

Bulk heterojunction solar cells based on a P3HT:$PC_{61}BM$ 1:0.8 blend are prepared as described in Sec. 4.6 from a solutions of 25 mg/ml out of chlorbenzene. Prior to contact evaporation (3 nm Ca/100 nm Al) the 110 nm

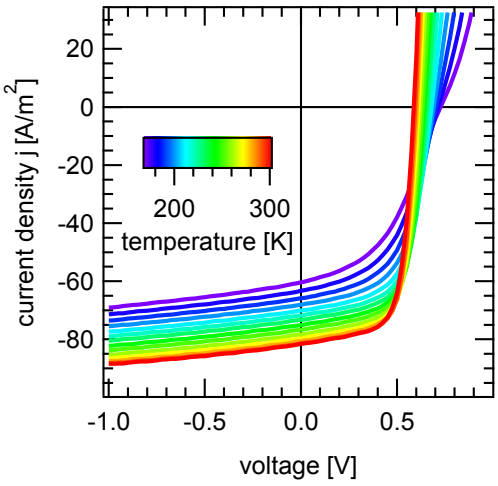


Figure 5.1: Current–voltage response of an annealed P3HT:$PC_{61}BM$ 1:0.8 solar cell under one sun in a temperature range from 300 to 170 K.

thick active layer was annealed for 10 min at 130°C. All materials were used without further purification. Prior to any additional measurements an Oriel 1160 AM1.5G solar simulator was used to perform illuminated $j/V$ measurements of devices kept under inert glovebox atmosphere. A representative cell, yielding a power conversion efficiency of approximately 3.3 % was chosen for further detailed transient studies. As already described in Chapter 4, the sample was transferred into a closed cycle optical cryostat for temperature dependent static and transient electrical studies, including $j/V$ measurements as well as TPV/TPC experiments.

## 5.4 Results and Discussion

In Fig. 5.1 the temperature dependent $j/V$ characteristics is depicted to get an impression about the device performance at different temperatures. In principle, a decrease in short circuit current density $j_{sc}$ and fill factor as well as an increased open circuit voltage $V_{oc}$ becomes apparent, when the temperature is varied from 300 to 170 K, which was reported already in literature [98]. At the same time the charge carrier mobility decreases for lower temperatures directly influencing the current and the fill factor while, according to Eq. (3.2), the reduced recombination rate due to lower mobility boosts the open circuit voltage $V_{oc}$.

Before coming back to the $j/V$ data further below, the temperature dependent TPV/TPC measurements are considered. As described in Sec. 4.1

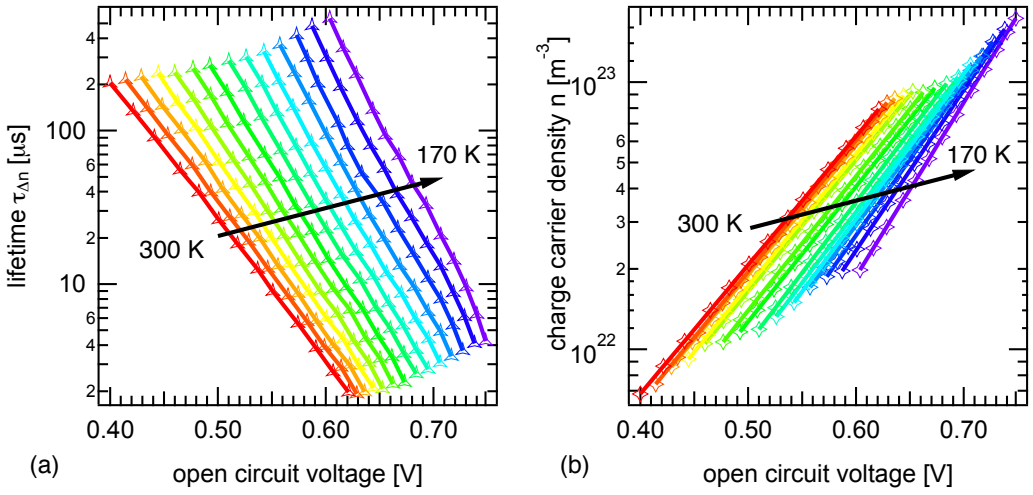


Figure 5.2: Temperature dependent results from TPV/TPC measurements for cells based on P3HT:$PC_{61}BM$: (a) small perturbation charge carrier lifetime and (b) charge carrier density both in dependence on the open circuit voltage. Thereby $V_{oc}$ was varied by changing the illumination intensity.

and 4.2 the small perturbation charge carrier lifetime $\tau_{\Delta n}$ and the charge carrier density $n$ under open circuit conditions can be derived from TPV/TPC experiments. The results for different illumination intensities and respective voltages are depicted in Fig. 5.2. As can be seen, the small perturbation charge carrier lifetime $\tau_{\Delta n}$ (Fig. 5.2 (a)) and the charge carrier density $n$ (Fig. 5.2 (b)) both exponentially depend on $V_{oc}$ and can be described by

$$\tau_{\Delta n} = \tau_{\Delta n_0} \exp\left(-\frac{qV_{oc}}{n_\tau kT}\right) \tag{5.4}$$

with the ideality factor of charge carrier lifetime $n_\tau$. And similarly,

$$n = n_0 \exp\left(\frac{qV_{oc}}{n_n kT}\right), \tag{5.5}$$

with $n_n$ defined as the ideality factor of charge carrier density. It is noted that the slopes in the semi-logarithmic representation of Fig. 5.2 (a) and (b) were previously described by parameters $\beta$ and $\gamma$ [70], which are related to the here utilized dimensionless ideality factors $n_\tau$ and $n_n$ by

$$n_\tau = \frac{q}{\beta kT}, \tag{5.6}$$

$$n_n = \frac{q}{\gamma kT}. \tag{5.7}$$

As seen in Fig. 5.2 both slopes $(\beta, \gamma)$ increase when the temperature is lowered.

### 5.4.1 SE parameters from Static and Transient Methods

To describe the experimentally found polaron dynamics in organic photovoltaic devices a generalized equation $dn/dt = -k_\lambda n^{\lambda+1} = -R(n)$ is often used as already mentioned in Section 3.2 (compare Eq. 3.4) addressing nongeminate recombination [70, 73, 74]. From TPV/TPC analysis, the decay order of the recombination rate $R$, $\lambda + 1$, and the small perturbation charge carrier lifetime $\tau_{\Delta n}$ can be experimentally determined. Using these values the total charge carrier lifetime $\tau_n$ can be calculated, as it is shown in Appendix A and in Ref. [99],

$$\tau_n = \tau_{\Delta n}(\lambda + 1), \tag{5.8}$$

where

$$\lambda = \frac{n_n}{n_\tau}. \tag{5.9}$$

Using Eqs. (5.4) and (5.8), small perturbation lifetimes values can be eliminated,

$$\tau_n = \tau_{n_0} \exp\left(-\frac{qV_{oc}}{n_\tau kT}\right). \tag{5.10}$$

Dividing Eq. (5.5) by Eq. (5.10), we obtain:

$$\underbrace{\frac{n}{\tau_n}}_{R(n)} = \underbrace{\frac{n_0}{\tau_{n_0}}}_{R_0} \exp\left(\frac{qV_{oc}}{(\frac{1}{n_n} + \frac{1}{n_\tau})kT}\right), \tag{5.11}$$

where $R(n)$ is defined as the recombination rate under illumination depending on illumination intensity while $R_0$ represents the recombination rate in dark. Solving Eq. (5.11) for $V_{oc}$ yields a more generalized expression,

$$V_{oc} = n_R \frac{kT}{q} \ln\left(\frac{R(n)}{R_0}\right), \tag{5.12}$$

with the recombination ideality factor $n_R$ defined as

$$n_R^{-1} = n_n^{-1} + n_\tau^{-1}, \tag{5.13}$$

which is consistent with earlier representations of the ideality factor [100, 72]. Comparing Eq. (5.12), derived by using relations empirically found in transient measurements (Eqs. (5.5),(5.4)), and the right hand side of Eq. (5.3), the SE solved for $V_{oc}$ to describe steady-state $j/V$ measurements, the same equation structure becomes apparent. To compare both equations, first the equality of recombination rates and respective currents is motivated. At $V_{oc}$ generation and recombination rates are equal, i.e. $G = R$, which implies the generation

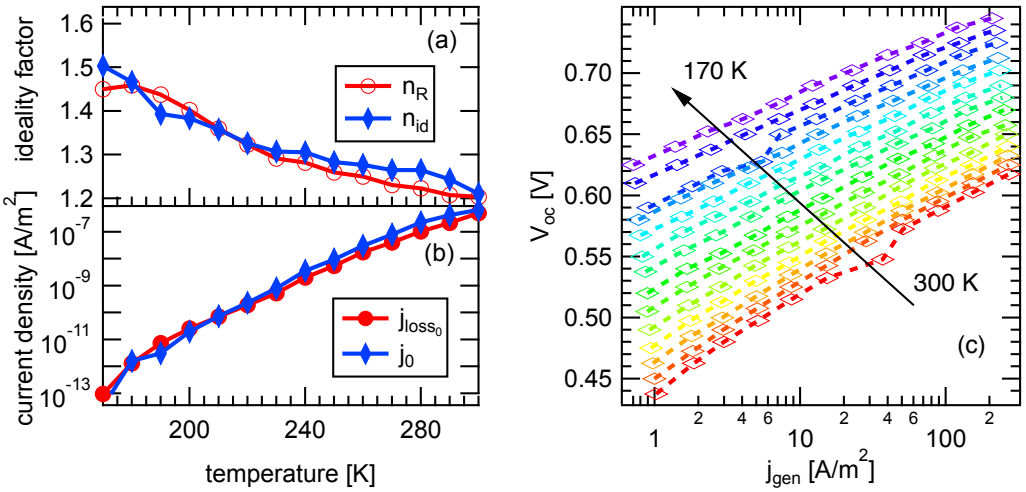


Figure 5.3: (a) Ideality factor of a P3HT:$PC_{61}BM$ 1:0.8 solar cell in dependence on temperature revealed from TPV/TPC studies on the recombination dynamics $n_R$ and from illuminated $j/V$ data $n_{id}$, analyzed with the Shockley Equation (see Eq. (5.3)). (b) Respective dark saturation current densities in dependence on temperature. $j_{loss_0}$ was calculated from TPV/TPC studies on the recombination dynamics in the dark with Eq. (5.15) and $j_0$ from illuminated $j/V$ response at $V_{oc}$ via Eq. (5.3) (c) The open circuit voltage $V_{oc}$ in dependence on the generation current $j_{gen}$ for various temperatures used to determine the static SE parameters $n_{id}$ and $j_0$.

current $j_{gen}$ (see Eq. (5.3)) is cancelled by the recombination current $j_{loss}$, defined as

$$j_{loss} = R(n)qd, \tag{5.14}$$

with the thickness of the active layer $d$. Likewise, the dark saturation current $j_0$ may be treated as thermally generated intrinsic charge carriers with the density $n_0$ and lifetime $\tau_{\Delta n_0}$ canceled by recombination $R_0$ in thermal equilibrium. Hence, the respective loss current in the dark $j_{loss_0}$ can be written as

$$j_{loss_0} = R_0 qd\cdot \tag{5.15}$$

The above considerations provide a rationale to the interconnection between the SE parameters derived diversely. Fig. 5.3 (a) shows ideality factors $n_{id}$ and $n_R$, as defined above, which were experimentally obtained as function of temperature by means of static ($j/V$) and transient (TPV/TPC) methods, respectively. To determine the static SE parameters $j/V$ characteristics

were recorded for different bias lights. Then, $V_{oc}$ was plotted vs. $j_{gen}$ (see Fig. 5.3 (c)) and analyzed by Eq. (5.3) to yield the ideality factor $n_{id}$ and $j_0$. Within the measured temperature range $n_R$ and $n_{id}$ correspond well to each other. Similarly, the dark saturation current $j_0$ and the dark recombination current $j_{loss_0}$, depicted in Fig. 5.3 (b), are almost equal for different temperatures. The ideality factor rises from 1.2 at room temperature to 1.5 at 170 K. A similar trend with temperature was observed in the past for organic solar cells based on different materials, although a stronger temperature dependence was obtained [96, 101].

From the experimental observation shown in Fig. 5.3 (a)/(b), the SE equivalence for P3HT:$PC_{61}BM$ based OSC to Eq. (5.12), derived from studying charge carrier recombination by transient techniques, can be suggested.

## Effective band gap energy $E_g$

As shown in Fig. 5.3 (b), the dark saturation current yields a strong temperature dependence. To further analyze this behavior in Fig. 5.4 (a), the dark saturation current $j_{loss_0}$ determined by TPV/TPC is plotted versus $1/(Tn_R(T))$, with the temperature dependent ideality factor $n_R(T)$ from Fig. 5.3 (a). The linear fit of the semi-logarithmic plot is in excellent agreement with the measured data and is expressed by the relation

$$j_{loss_0} = j_{00} \exp\left(-\frac{E_g}{n_R(T)kT}\right). \tag{5.16}$$

The fit demonstrates that the dark saturation current follows the Boltzmann distribution and allows to identify the effective band gap energy $E_g$, which is proportional to the difference between HOMO and LUMO energy levels of donor and acceptor, respectively. An effective gap of $E_g = 1.07$ eV was found for the studied cell based on P3HT:$PC_{61}BM$. From the $V_{oc}(T)$ data (see Fig. 5.4 (b)), a value of $E_g \approx 0.90 \pm 0.15$ eV was evaluated according to Ref. [98], Eq. (1). Vandewal *et al.* obtained a value of $E_g = 1.08$ eV from the energy onset of the photocurrent generated by CT absorption [102], which agrees particularly well with our value. Guan *et al.* found somewhat larger values ($E_g \approx 1.3 - 1.4$ eV) using ultraviolet and inverse photoemission spectroscopy [103]. As discussed in Ref. [104], energy values derived by photoemission spectroscopy can be seen as onsets of respective valence and conduction band. Due to charge carrier relaxation into the tail states of the density of states, the techniques such as TPV/TPC and $j/V$ measurements are expected to reveal the effective band gap $E_g$ from the density of occupied states after thermalization instead.

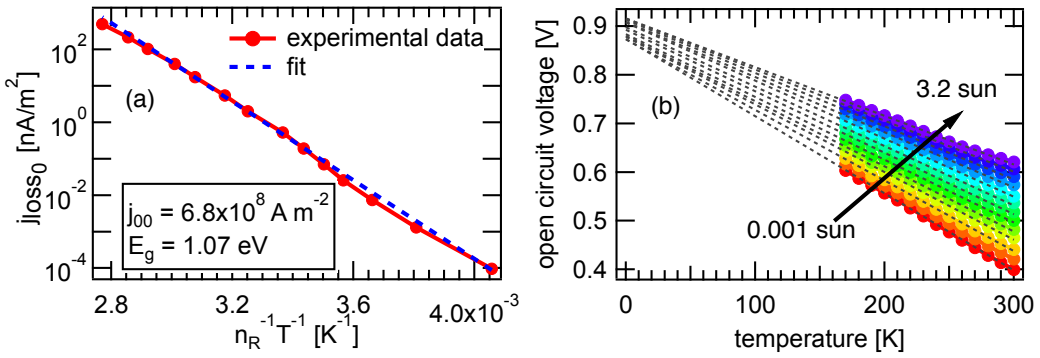


Figure 5.4: (a) Dark saturation current evaluated by studying the charge carrier dynamics plotted versus $1/Tn(T)$ in order to estimate the effective band gap energy $E_g$ from Eq. (5.16). (b) Approximation of $E_g$ by $V_{oc}(T)$ dependence according to Ref. [98].

### 5.4.2 Loss Current vs. Photocurrent

To complete the comparison of Eq. (5.3) and Eq. (5.12) the photogenerated charge is compared to the number of charge carriers recombining at $V_{oc}$. In order to estimate the photogenerated charge carriers, we used the saturated current density $j_{sat}$ under illumination in reverse bias ($V = -1$ V).

If the generation of charge carriers is voltage independent for P3HT:PC$_{61}$BM cells in the range of $-1$ V $< V < V_{oc}$ [50, 51] and $j_{sat}$ is not reduced by nongeminate recombination, we expect

$$j_{sat} = j_{loss} \cdot \tag{5.17}$$

For the comparison, Eq. (5.14) was used to calculate the recombination current $j_{loss}$ under illumination at open circuit.

The saturation current $j_{sat}$ and the nongeminate recombination current $j_{loss}$ at $V_{oc}$ determined via TPV/TPC measurements for different illumination intensities from 0.1 sun to about 1.8 suns are shown in Fig. 5.5 (a). Within experimental error, $j_{loss}$ is in a very good agreement with $j_{sat}$ for all light intensities and temperatures above 200 K. Below this temperature $j_{sat}$ becomes smaller than $j_{loss}$, which seems to imply more charges recombining than being generated. This counterintuitive result can at least partly be explained by estimating the nongeminate recombination losses at $V = -1$ V according to Ref. [105]. We find 2% loss at room temperature and 5% at 170 K, revealing the limitations of the analysis as the determined generation current $j_{sat}$ is underestimated. Accounting for these nongeminate losses, a very small deviation

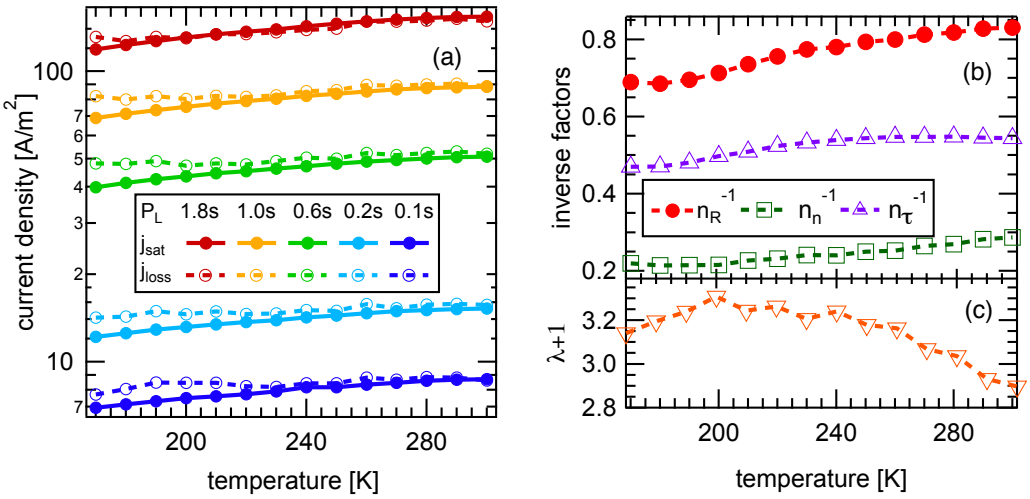


Figure 5.5: (a) Current density $j_{sat}$ (solid lines) from $j/V$ response compared to recombination current $j_{loss}$ (dashed lines) measured by TPV/TPC for different temperatures and bias lights according to Eq. (5.17). For $T < 200$ K a stronger deviation of both parameters becomes apparent. (b) Temperature dependence of the inverse ideality factors for charge carrier density, $n_n^{-1}$, and lifetime, $n_\tau^{-1}$, as well as their sum, resulting in the inverse ideality factor $n_R^{-1}$. (c) Corresponding recombination order $\lambda = n_n/n_\tau + 1$.

of $j_{sat}$ and $j_{loss}$ remains, showing that the field dependence of the photogeneration is less than 10% between open and short circuit conditions even at temperatures below 200 K. In accordance with earlier findings [97, 47, 50, 51], the photocurrent in annealed P3HT:$PC_{61}BM$ solar cells is field-independent in a temperature range from 300 to 200 K and at best slightly field-dependent for $T < 200\ K$. This result will be confirmed by additional experiments in Chapter 6.

### 5.4.3 Contributions to Recombination Ideality Factor $n_R$

In Eq. (5.12) the recombination ideality factor $n_R$ was defined. As mentioned above $n_R$ is composed by the ideality factor for charge carrier density $n_n$ and charge carrier lifetime $n_\tau$, respectively (see Eq. (5.13)). In Fig. 5.5 (b), the inverse ideality factors derived from the transient experiments are plotted versus temperature. At 300 K, $n_\tau = 1.84$ and $n_n = 3.49$ become apparent yielding a recombination ideality factor of $n_R = 1.20$. As shown already in Fig. 5.3 (a), the ideality factor from the $j/V$ characteristics under illumina-

tion was $n_{id} = 1.21$. Although the following considerations are based on the ideality factors measured under illumination, it is noted for comparison that the dark ideality factor was 1.30, whereas Kirchartz *et al.* [72] found a value of 1.6.

The recombination order, given by $\lambda + 1 = \frac{n_n}{n_\tau} + 1$ as pointed out above, is shown in Fig. 5.5 (c). The recombination order at 300 K of $\lambda + 1 = 2.90$ is slightly higher as compared to the values of 2.60 (Ref. [70]) or 2.75 in our former study on P3HT:$PC_{61}BM$ (Ref. [73]). This might be related to slightly different preparation conditions and different material batches.

### 5.4.4 Interpretation of Ideality Factors

The following discussion is based on the very concise approach offered by Kirchartz *et al.* [72]. The experimentally determined ideality factors are used to consider the dominant recombination mechanism in the P3HT:$PC_{61}BM$ solar cells under open circuit conditions.

Ideality factors higher than 1 in organic bulk heterojunction solar cells are commonly seen as an evidence for a dominant trap assisted recombination process. Kirchartz *et al.* proposed the recombination of free charge carriers $n_c$ with trapped charge carriers $n_t$ in an exponential tail as dominant nongeminate loss mechanism in P3HT:$PC_{61}BM$ solar cells. The corresponding recombination rate is $R \propto n_c n_t$, assuming symmetric electron and hole concentrations. According to Ref. [106] the density of trapped charges $n_t$ relates to the free charges $n_c$ by

$$n_t \propto n_c^{kT/E_U} \tag{5.18}$$

if trap states are distributed exponentially with a characteristic Urbach tail energy $E_U > kT$ (see Fig. 5.6 (b)). In a conventional semiconductor, where charge neutrality ($n = p$) is assumed, the density of free charges $n_c$ scales with

$$n_c \propto \exp\left(\frac{qV}{2kT}\right). \tag{5.19}$$

Together with Eq. 5.18 this leads to

$$n_t \propto \exp\left(\frac{qV}{2E_U}\right) \tag{5.20}$$

and the recombination rate scaling with

$$R \propto n_c n_t \propto \exp\left(\frac{qV}{2kT}\right) \exp\left(\frac{qV}{2E_U}\right) = \exp\left(\frac{qV}{kT} \underbrace{\left[\frac{1}{2} + \frac{kT}{2E_U}\right]}_{n_{id}^{-1}}\right) \tag{5.21}$$

with the ideality factor $n_{id}$ being identified by van Berkel *et al.* [100]. The scaling of $R$ on carrier density,

$$R \propto n_c n_t \propto n_t^{E_U/kT+1} \tag{5.22}$$

illustrates that if the trapped charges are included in the density $n$ determined experimentally, the often reported recombination order $\lambda+1 > 2$ (see Eq. 3.4) can be explained by tail recombination with $E_U > kT$.

With the above described approach Kirchartz *et al.* was able to calculate the characteristic (Urbach) tail energy $E_U$ from experimental data [70] by three routes:

(i) By the voltage dependence of the extracted charge carrier concentration (compare Eq. 5.20 and Eq. 5.5), which is given by the ideality factor $n_n$,

$$E_U = \frac{n_n kT}{2}. \tag{5.23}$$

(ii) From the (in their case dark) ideality factor, based on Eq. 5.21

$$n_{id}^{-1} = \frac{kT}{2E_U} + \frac{1}{2}. \tag{5.24}$$

(iii) From the recombination order

$$\lambda + 1 = \frac{E_U}{kT} + 1, \tag{5.25}$$

according to Eq. 5.22. From (i) Kirchartz *et al.* found $E_U \approx 50$ meV, from (ii) $E_U \approx 100$ meV at room temperature, whereas from (iii) $E_U = 41$ meV can be calculated. This discrepancy was discussed in some detail in their publication [72].

In order to show the self consistency of the above presented framework of ideality factors determined by transient techniques (see Section 5.4.1), Eq. (5.13) is considered and verified in the following. For that purpose Eq. (16) of Ref. [72] is used, where Kirchartz *et al.* considered the carrier concentration dependent loss current at $V_{oc}$,

$$j_{loss} \propto R(n) \propto n^{\delta} \equiv n^{\lambda+1} \tag{5.26}$$

and its connection to the voltage dependence of the carrier concentration, cf. Eq. (5.5). It is further reported that

$$\underbrace{\frac{d\ln j_{loss}}{d\ln n}}_{\lambda+1} \cdot \underbrace{\frac{d\ln n}{dV}}_{n_n^{-1}\frac{q}{kT}} = \underbrace{\frac{d\ln j_{loss}}{dV}}_{n_{id}^{-1}\frac{q}{kT}}, \tag{5.27}$$

while the under braced notation already refers to the here presented framework [107]. Evaluating this equation, considering $\lambda = \frac{n_n}{n_\tau}$, the relation

$$\left(\frac{n_n}{n_\tau} + 1\right) \cdot n_n^{-1} = n_{id}^{-1} \tag{5.28}$$

is found, which directly yields Eq. (5.13) derived in Sec. 5.4.1. Thus, the three different routes (i)-(iii) outlined above are effectively merged to one, while the (experimentally found) deviation of $n_\tau < 2$ is accounted for in the revised approach. Due to the good agreement between transient and static ideality factor (see Fig. 5.3 (a)), it is possible to determine a consistent Urbach energy of $E_U \approx 45 - 50$ meV at T=300 K. The increase of $n_n$ with lower temperatures (Fig. 5.5 (b)) also indicates a thermally activated process concerning the charge carrier concentration: the lack of thermal energy leading to a growing fraction of trapped charge carriers is compatible with the assumption of exponential tail states. However calculating the characteristic Urbach energy from the temperature dependent $n_n$ by using Eq. (5.23), $E_U = 40$ meV for 200 K is found, showing that an exponential tail may not be the precise shape of the density of trap states, but can serve as an approximation in a limited temperature range.

To go further beyond the approach of Kirchartz *et al.* in the following, a more general recombination rate is considered, including the annihilation of free charge carriers with one another and free with trapped charge carriers,

$$R(n) = k' n_c (n_c + n_t) = k' n_c n. \tag{5.29}$$

Here, the overall charge carrier concentration is given as $n = n_c + n_t$. For simplicity, the same recombination prefactor $k'$ for both contributions $n_c^2$ and $n_c n_t$ is used.

Usually the rate limiting step in nongeminate recombination is the finding of the localized charge carriers by a hopping process, which is reflected by a prefactor proportional to the mobility of the mobile charge carriers, based on Langevin theory [41, 72, 108]. However, although beyond the scope of this work, it is pointed out that in the multiple-trapping-and-release approximation of hopping transport, the effective mobility $\mu$ is proportional to a trap-free mobility $\mu_0$ times the fraction of free to all charge carriers, $\mu_0 \frac{n_c}{n}$ [109]. Within this approach, $R \propto \mu n^2$ and $R \propto \mu_0 n_c n$ are in principle equivalent. The reader is asked to bear in mind that this representation can serve as a first approximation, but neglects the field dependence in a hopping model. However, Eq. (5.29) is sufficient to describe the recombination process in terms of the ideality factors discussed above.

The small-signal method TPV yields the effective lifetime of all charge carriers, $\tau_n$. For charge extraction, it is assumed that all charge carriers were

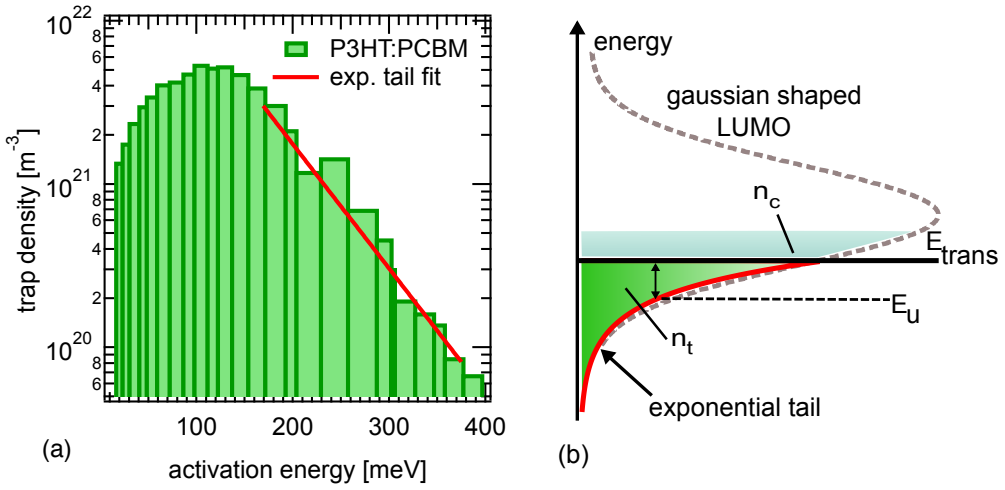


Figure 5.6: (a) Trap density distribution of a P3HT:$PC_{61}BM$ blend device, as measured by the thermally stimulated currents technique [110]. Disregarding the detailed shape of the trap distribution, the energetic tail (solid line) is approximated, finding a characteristic energy $E_U \approx 57$ meV. (b) Scheme of the exponential tail approximation on the gaussian density of states.

extracted, in accordance with Kirchartz *et al.* [72]. Thus, the experimentally determined effective recombination rate is $R = n/\tau_n = (n_c + n_t)/\tau_n$ (c.f. Eq. (5.11)). Considering the assumed recombination rate, Eq. (5.29), and an effective recombination rate $R = \frac{n}{\tau_n}$, leads to

$$\tau_n = (k' n_c)^{-1}. \tag{5.30}$$

Within the assumptions made for the recombination, the effective lifetime is inversely proportional to the free charge carrier concentration $n_c$. Therefore, one would expect that $n_\tau$ should equal 2 in accordance with $n_n$ for free charge carriers (see Eq. (5.19)). However, this statement is only valid if the recombination prefactor $k'$ is assumed to be voltage independent. While the detailed reason for the experimental finding of $n_\tau = 1.84$ cannot be identified, it should be mentioned that the assumption of $k' \neq k'(V)$ may not hold true [111, 112] and that concentration gradients and their influence [113] are disregarded.

In order to verify that the nongeminate recombination mechanism in annealed P3HT:$PC_{61}BM$ solar cells is indeed due to losses of free carriers with one another and with carriers trapped in exponential tail states with $E_U \approx 50$ meV, thermally stimulated current measurements, presented previously, are reconsidered [110]. In this set of experiments, trap states deeper than 400 meV are not accounted for. The distribution of the trap states is shown in a semilogarithmic plot (Fig. 5.6 (a)). Neglecting the detailed

shape, the energetic tail can be approximated by an exponential Urbach fit ($n_t \propto \exp(-\frac{kT}{E_u})$) yielding a characteristic energy $E_U \approx 57$ meV. This is in good accordance with a recent reconstruction of the density of trap states in P3HT:$PC_{61}$BM blends [114], and supports the findings from above.

## 5.5 Conclusion

The SE parameters such as ideality factor $n_{id}$ and dark saturation current $j_0$ were derived from static $j/V$ measurements as well as from the transient techniques (TPV/TPC) and were shown to coincide within experimental error for OSC based on P3HT:$PC_{61}$BM. The ideality factor and dark saturation current density were directly compared experimentally over the temperature range from 200 to 300 K. The recombination current determined under open circuit conditions is shown to be equal to the respective saturation current for various bias lights and temperatures, which implies that the polaron pair dissociation is not significantly influenced by the electric field. A good agreement of static and transient approaches over a wide temperature range demonstrates the validity of the Shockley model for OSC, if the charge carrier photogeneration is voltage independent. Additionally, the dark saturation current measured at different temperatures was used to determine the effective band gap of P3HT:$PC_{61}$BM blend to be in the range of $E_g \approx 0.9 - 1.1$ eV, which is in good agreement to values from literature. By further analyzing the ideality factors, nongeminate recombination of free with both free and trapped charge carriers in exponential tail states is discussed. Using data from thermally stimulated current measurements, we verified that the charge carrier traps can indeed be approximated by an exponential trap distribution.

Chapter 6

# Impact of Charge Recombination on $j/V$ response

In the present chapter the impact of geminate and nongeminate charge carrier recombination on the current–voltage characteristics of different organic solar cells is studied by transient photovoltage and charge extraction in combination with time delayed collection field measurements. Special emphasis is put on the morphological aspect. First, as-prepared (pristine) and thermally treated (annealed) P3HT:$PC_{61}BM$ devices are compared and investigated in a temperature dependent study. Secondly, the analysis is extended by the high performing low-band gap polymer PTB7 in combination with $PC_{71}BM$. The influence of a solvent additive on the $j/V$ response is discussed and the respective dominant loss mechanism is determined. Parts of the following results were published in Paper 2 and Paper 5.

## 6.1 Pristine vs. annealed P3HT:$PC_{61}BM$ Solar Cells

### 6.1.1 Introduction

In the previous chapter the charge carrier recombination in annealed P3HT:$PC_{61}BM$ solar cells was already studied by TPV and TPC measurements. Within the present chapter, as-prepared and annealed devices from the same material batch are prepared and compared in terms of device performance, charge carrier lifetime and charge carrier density. Further the nongeminate loss current is calculated and its impact on the current–voltage response is analyzed, according to the $j/V$ reconstruction procedure described in Section 3.3.

The device preparation in principle was identical to the one described in Sec. 5.3. The cells referred to as pristine were not tempered before contact evaporation, while annealed cells were heated for 10 min at 130°C. The temperature dependent TPV and charge extraction (CE) measurements were performed in the same closed cycle optical cryostat as previously mentioned in Chapter 4 & 5.

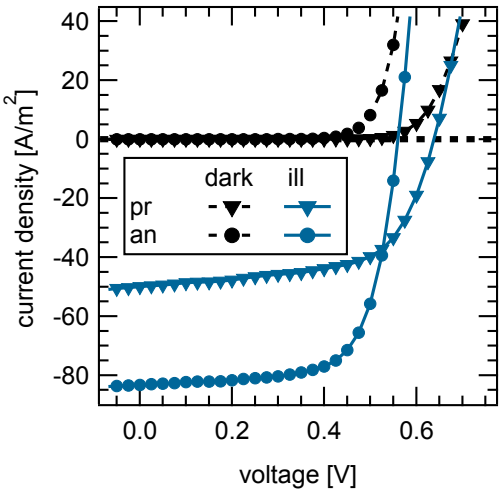


Figure 6.1: Current–voltage response of a pristine and an annealed P3HT:$PC_{61}BM$ 1:0.8 solar cell under one sun AM 1.5 spectrum at 300 K.

### 6.1.2 T-dependent nongeminate Recombination

As shown in several publications by atomic force microscopy (AFM) or bright-field transmission electron microscopy (TEM) images, the morphology of P3HT:$PC_{61}BM$ active layers dramatically changes with external applied thermal energy (annealing) [115, 116]. From X-ray diffraction measurements an increase in crystallinity upon annealing and further an a-axis orientation of polymer crystallites can be concluded (side-chain perpendicular to substrate) [85]. The formation of elongated PCBM nanocrystals upon annealing was proven by high resolution TEM images and provides a more efficient transport pathway for electrons and thus significantly improves charge carrier transport [117]. The resulting influence on device performance becomes apparent in Fig. 6.1, where representative pristine and annealed $j/V$ characteristics are plotted for one sun illumination under AM 1.5 spectrum at 300 K. The macroscopic device parameters are summarized in Tabel 6.1. The rise in efficiency from 2% to 3.3% upon annealing is mainly attributed to the enhanced short circuit current and the fill factor reaching 70% which is in good accordance with literature [116]. The improved fill factor indicates better charge transport properties in annealed cells, while the higher current could originate from improved charge generation due to donor–acceptor phase separation becoming apparent in TEM images [115]. The reduced fill factor in pristine cells might have its origin in a voltage dependent charge generation. As concluded in Chapter 5, annealed cells exhibit a charge generation mainly independent of the electric field, even at low temperatures. To further analyze the origin of

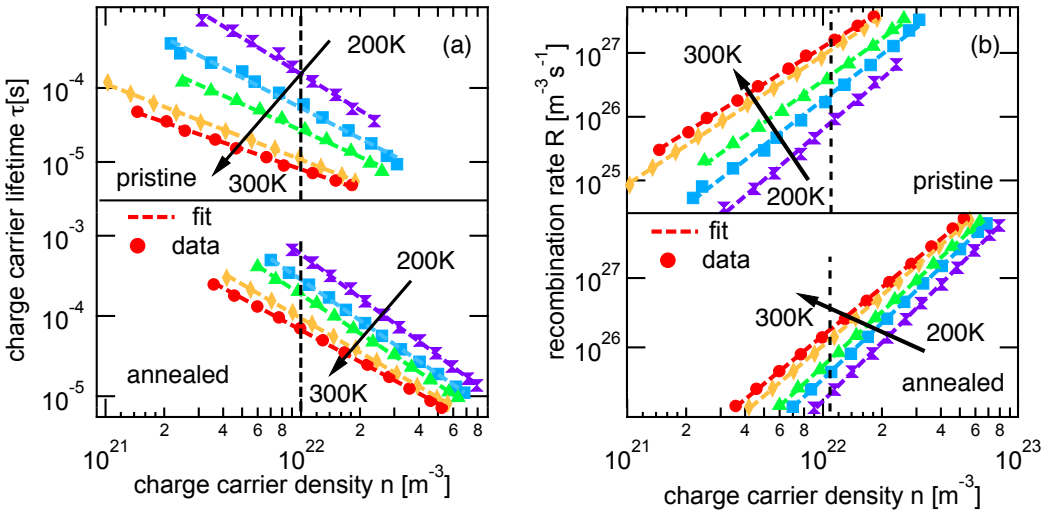


Figure 6.2: Temperature dependent results from TPV/CE measurements for cells based on P3HT:PC$_{61}$BM: (a) Comparison of the charge carrier lifetime $\tau$ as a function of the charge carrier density $n$ for pristine and annealed cells. Dashed lines refer to fits according to Eq. (6.1) and illustrate the recombination order $\lambda$. (b) Respective recombination rates R calculated by Eq. (3.4) in dependence on $n$.

the difference in photovoltaic performance, in Sec. 6.1.3 an $j/V$ reconstruction based on nongeminate losses is carried out as described theoretically in Sec. 3.3.

In the following the differences between pristine and annealed cells with respect to nongeminate recombination are addressed. To this end, the small perturbation charge carrier lifetime $\tau_{\Delta n}$ and the charge carrier density $n(V_{oc})$ under open circuit conditions are determined via TPV and CE measurements. As already noted in Chapter 5, the parameter $\tau_{\Delta n}$ directly accessible by TPV, is related to the total charge carrier lifetime by $\tau(n) = \tau_{\Delta n}(\lambda + 1)$ (see Eq. (5.8)) [99, 118]. The dependence of lifetime $\tau$ on charge carrier den-

| P3HT:PC$_{61}$BM | $j_{sc}$ [A/m$^2$] | $V_{oc}$ [mV] | FF [%] | $\eta$ [%] |
|---|---|---|---|---|
| pristine | 50 | 643 | 63 | 2.0 |
| annealed | 83 | 565 | 70 | 3.3 |

Table 6.1: $j/V$ parameters of pristine and annealed P3HT:PC$_{61}$BM cells under one sun illumination at 300K.

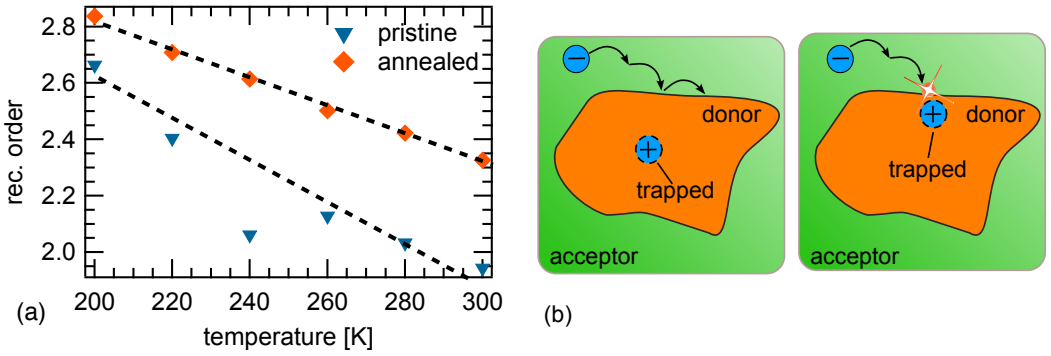


Figure 6.3: (a) Recombination order of pristine and annealed P3HT:$PC_{61}BM$ cells for various temperatures. Dashed lines are guides for the eyes. (b) *left*: Scheme of hole trapped apart from heterointerface → screened from nongeminate recombination as long as trapped *right*: hole trapped close to interface → annihilation possible although being trapped.

sity $n$ is depicted in Fig. 6.2(a) for temperatures from 300K to 200K. For the pristine cell exponential dependencies of lifetime and charge carrier densities on $V_{oc}$ were found, similar as reported in Chapter 5 for annealed ones (see Fig. 5.2 and Eq. (5.5), (5.10)). Consequently, the dependence of lifetime on charge carrier density $\tau(n)$ in both devices results in

$$\tau(n) = \tau_0 n^{-\lambda}, \tag{6.1}$$

where $\tau_0$ responds to the intercept at $n = 0$ in Fig. 6.2(a) and $\lambda$ refers to the recombination order defined by Eq. (5.9) [92]. Eq. (6.1) was used for the fit shown in Fig. 6.2(a).

As depicted by the slopes of the fits the carrier concentration dependence of $\tau(n)$ becomes stronger at low temperatures. Consequently, the magnitude of the charge decay order $\lambda + 1$ increases at lower temperatures, which indicates additional trapped and subsequently released charges being involved in recombination processes, as reported previously for annealed devices [73, 112]. In general $\tau$ is higher ($\approx$ factor 5) for the annealed than for the pristine cell at matched $n$ and temperature. This finding can result from distinct phase separation and crystalline domains within the bulk due to thermal treatment [119]. Absolute values for $T = 300$K are in good agreement with Ref. [99]. For a better comparison in Fig. 6.2(b) the respective nongeminate recombination rates $R(n)$, calculated by Eq. 3.4 are compared with respect to the charge carrier density. The fine intermixing of donor and acceptor leads to considerable higher recombination rates in pristine cells. In both representations, $\tau(n)$

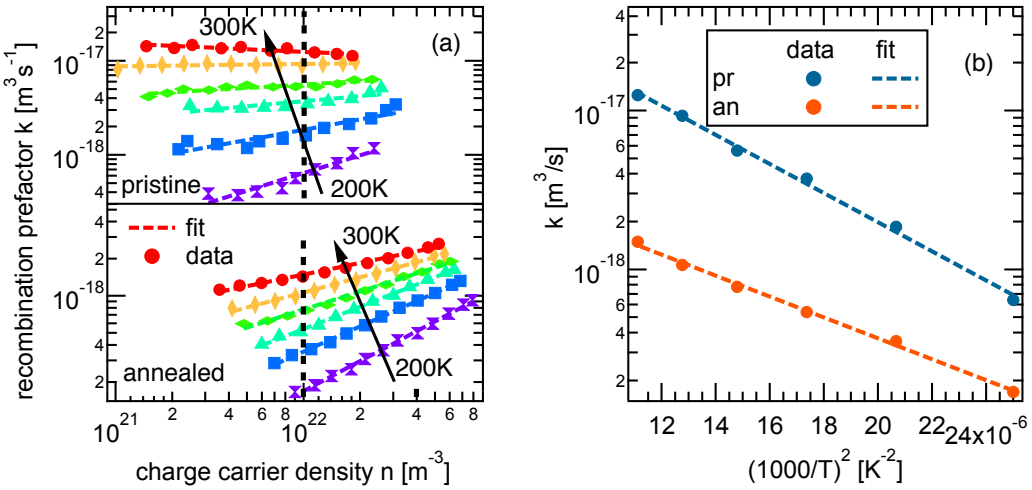


Figure 6.4: (a) Recombination prefactor $k$ of the as-prepared and the annealed cell in dependence on charge carrier density for various temperatures. (b) Semi-logarithmic temperature dependence of $k$ for one distinct carrier density $n = 10^{22}$ m$^{-3}$.

and $R(n)$, a stronger dependence on temperature for the pristine cell becomes apparent. Calculating the apparent recombination order (see Fig. 6.3 (a)) corroborates this statement. Starting around a pure bimolecular order of $\lambda+1 \approx 2$ for 300 to 260K the increase for lower temperatures is stronger for the pristine than for the annealed cell (dashed lines in Fig. 6.3 (a)). To understand this behavior, two aspects have to be considered. As already mentioned above and discussed in literature [73, 112], the presence and their delayed participation in recombination of trapped charges $n_t$ leads to the higher apparent recombination order. It is thereby also important where exactly charges are trapped spatially: close to a donor–acceptor heterointerface and thus accessible by their oppositely charged counterpart moving in the other phase (Fig. 6.3 (b) *right*) or apart from any heterointerface within a pure domain and not being able to recombine as long as being trapped (Fig. 6.3 (b) *left*).

The differences in morphology become apparent by AFM/TEM images [115, 116, 117], where a clear phase separation in annealed cells is visible. Hence, the portion of charges being trapped apart from an heterointerface is assumed to be higher in annealed cells due to larger domains leading to initially higher recombination orders, i.e. Fig. 6.3 (a).

As Mauer *et al.* discussed recently by results based on transient absorption measurements on annealed P3HT:$PC_{61}BM$ devices, the ratio $n_t/n_c$ between

trapped and free charges rises with lower temperature. This results in a charge carrier density dependent mobility $\mu$ being more pronounced at low temperatures [120]. To this end, the enhanced decay order for low temperatures is not surprising. The ratio of trapped to free charges is also effected by the width $\sigma$ of the density of states, while the percentage of trapped charges rises with $\sigma$. In order to estimate the width $\sigma$ in the framework of the Gaussian disorder model (GDM) a pure bimolecular decay $R \propto n^2$ is assumed, with a charge carrier dependent recombination prefactor $k(n)$, as discussed in Ref. [73]. This results in

$$R = k(n)n^2, \tag{6.2}$$

while $k(n)$ corresponds to the Langevin recombination prefactor $\gamma \propto \mu$, i.e. Eq. (3.2). Consequently, following the GDM and Eq. (2.3) the temperature dependence of $k$ should be analog to $\mu(T)$ and hold

$$k \propto \exp\left(-\left(\frac{2\sigma^*}{3kT}\right)^2\right), \tag{6.3}$$

where $\sigma^*$ is related to the energetic disorder of the system. In Fig. 6.4 (a) $k(n) = \frac{R}{n^2}$ is plotted for both, the pristine and the annealed solar cell. To analyze $k(T)$ a cross section at $n = 10^{22}$ m$^{-3}$ was taken, indicated by the vertical dashed line. The result is summarized in Fig. 6.4 (b), where the temperature dependence of $k$ is revealed.

Eq. (6.3) was used for the respective fit and a very good agreement to the experimental data becomes apparent. The respective fit parameters enable to determine $\sigma^* \approx 50.3$ meV for the annealed and $\sigma^* \approx 59.4$ meV for the pristine device. One can therefore conclude that a major part of the temperature dependence of $k(T)$ stems from the charge carrier mobility in the framework of the GDM. The higher $\sigma^*$ in pristine devices might be one reason for the stronger temperature dependence of the recombination order in pristine cells, as trapping at low temperatures is more dominant than in annealed samples.

### 6.1.3 $j/V$ Reconstruction of P3HT:PC$_{61}$BM

The following study on the impact of recombination on the $j/V$ characteristics is based on the approach of $j/V$ reconstruction described in Sec. 3.3. As shown in Fig. 6.2(b) a power law dependence of the nongeminate recombination rate $R$ on the carrier density $n(V_{oc})$ was successfully determined by the combination of TPV and CE measurements under open circuit conditions. In order to calculate the correct nongeminate loss current $j_{loss}(V)$ necessary for $j/V$ reconstruction, two prerequisites must be fulfilled. On the one hand, voltage dependent CE measurements need to be recorded to derive $n(V)$ data. On

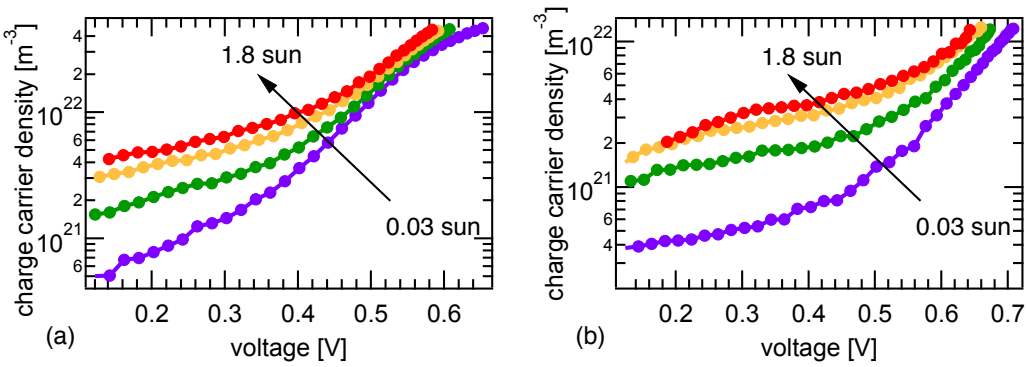


Figure 6.5: Voltage dependent charge carrier density $n(V)$ for different illumination intensities at room temperature for (a) an annealed and (b) an as-prepared P3HT:PC$_{61}$BM solar cell.

the other hand, the nongeminate recombination rate must not be dependent explicitly on voltage.

For annealed P3HT:PC$_{61}$BM solar cells at room temperature a successful $j/V$ reconstruction based on pure nongeminate recombination loss currents was reported recently [75]. By verification of this finding the new established experimental setup and subsequent data evaluation was tested on reliability. In Fig. 6.5 the charge carrier density in dependence on voltage and different illumination intensities is depicted for the annealed (a) and the pristine device (b) at room temperature. Except for the case of $V = V_{oc}$, a photocurrent is flowing for every applied voltage. As a consequence, the series resistance $R_S$ of the measurement circuit needs to be determined in order to account for the correct voltage. It was derived from the ohmic range of the dark $j/V$ curve at 300K and yielded $R_S = 92\ \Omega$ for the annealed and $R_S = 217\ \Omega$ for the pristine device. The voltage $V$ used was corrected for $R_S$ by $V = V_{appl} - IR_S$.

The trend on voltage and the absolute values are comparable to Ref. [75], which hints on reliable data. If both cells, pristine and annealed, are compared higher charge carrier densities are revealed for the annealed device. This is in good accordance with the lower recombination rate in annealed cells determined above (see Fig. 6.2(b)).

Employing Eq. (3.8) and approximating the generation current $j_{gen}$ to be voltage independent and equal to the short circuit current ($j_{gen} = j_{sc}$) yields

$$j(V) = j_{sc} - j_{loss}(n(V))\cdot \tag{6.4}$$

Here, $j_{loss}(n(V))$ is determined by Eq. (5.14) while $R$ is calculated by Eq. (3.4) and experimental $n(V)$ data together with Eq. (6.1) as input parameters. The

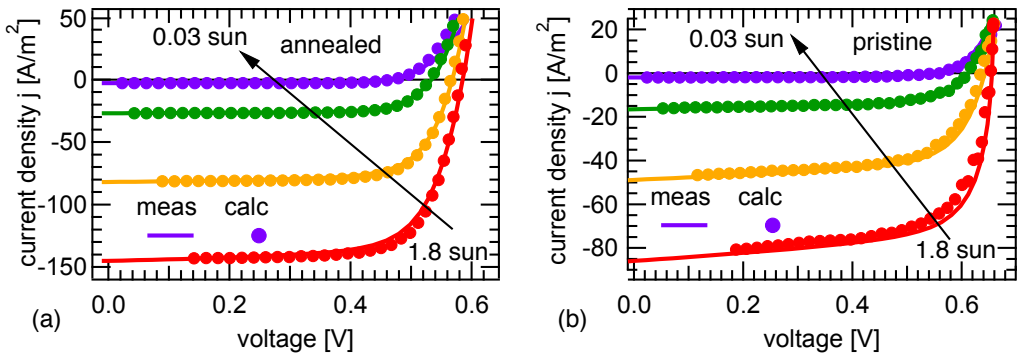


Figure 6.6: $j/V$ reconstruction for different light intensities for (a) annealed and (b) pristine P3HT:$PC_{61}BM$ solar cells at room temperature.

calculated $j/V$ response (by Eq. (6.4)) is plotted together with the measured data in Fig. 6.6. The excellent agreement for all light intensities between the measured and the reconstructed $j/V$ curves of the annealed devices perfectly agrees with the results of Shuttle *et al.* Also the measured data of the as-prepared cell is in good accordance with the calculations based on nongeminate losses. This result primarily reveals that the photogeneration of charge carriers in both, annealed and pristine P3HT:$PC_{61}BM$ solar cells is voltage independent for 300K. Furthermore in the examined voltage range the $j/V$ characteristics is dominated by nongeminate recombination losses solely and geminate losses therefore can be neglected. Thus, nongeminate recombination is identified as the performance limiting loss mechanism in P3HT:$PC_{61}BM$ solar cells.

For a deeper understanding of the present material system the same calculations of $j/V$ reconstruction were done in a temperature range from 300K to 200K. The charge carrier density $n(V)$ for an illumination intensity of one sun for the pristine and the annealed cell and different temperatures is depicted in Fig. 6.7(a) in dependence on voltage. All voltages were corrected for the series resistance $R_s$, as described above. For both samples the average charge carrier concentration $n$ increases for low temperatures while the dependence of $n$ on $V$ becomes weaker, especially at higher voltages. The former is again attributed to a decrease in mobility and thus recombination. The reduced slope of $n(V)$ at low temperatures, especially for the pristine cell, could result from space charge limitation, hindering injection at a certain applied voltage as well as charge extraction in CE experiments.

The experimental $n(V,T)$ data enables to calculate the respective nongeminate loss current $j_{loss}$ $n(V,T)$. Together with the respective short circuit cur-

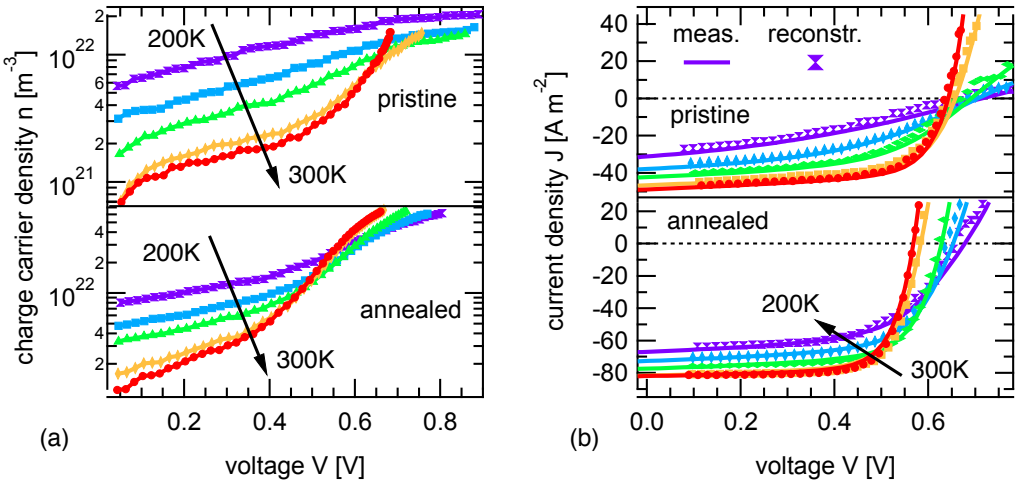


Figure 6.7: (a) Charge carrier density in dependence on voltage for different temperatures of pristine and annealed P3HT:$PC_{61}$BM solar cells and (b) the respective reconstructed and measured $j/V$ characteristics.

rent of every temperature, Eq. (6.4) is employed to calculate $j(V,T)$. The calculations and the measured $j/V$ characteristics for one sun illumination are plotted in Fig. 6.7(b) for both cell types. It is nicely shown that the fill factor and the open circuit voltage could be reproduced quite accurately for both cells in the studied temperature range. Hence, the good agreement of measured and reconstructed data confirms that nongeminate recombination is the main loss mechanism determining the $j/V$ behavior for annealed [75] as well as for pristine P3HT:$PC_{61}$BM devices in a wide temperature range. It is pointed out that the very good agreement implies a voltage independent photogeneration in the range $0 < V < V_{oc}$ and down to 200K. Similar results concerning photogeneration were found recently for annealed samples [49, 50, 51, 121], but were not yet reported for pristine ones. From the dramatic change in morphology between pristine and annealed devices (revealed by AFM and XRD measurements) also an impact on charge generation was assumed. Consequently, it is quite surprising that the photogeneration is found to be field-independent in both device types. In order to verify the constant photogeneration rate of the pristine device, time delayed collection field measurements (TDCF) were applied additionally. As described in Sec. 4.4 TDCF is well established to investigate field-dependent charge generation [51, 50]. A delay time of $t_d = 380$ ns and a collection voltage of $V_{col} = -6$ V were chosen. In Fig. 6.8 the voltage range $-2\ V < V < V_{oc}$ is analyzed. In very

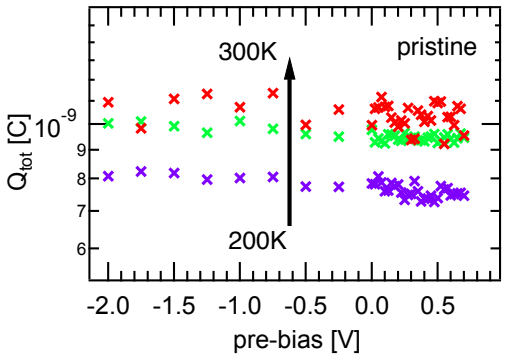


Figure 6.8: Total extracted charge $Q_{tot}$ of time delayed collection field measurements for different pre-bias voltages and temperatures of a pristine P3HT:$PC_{61}$BM solar cell.

good accordance with our statement from above, the total extracted charge $Q_{tot}$ varies less than 5% between open circuit and short circuit conditions, which is negligible in relation to the experimental error. To conclude, both approaches, the successful $j/V$ reconstruction and the TDCF measurements, revealed a field-independent charge generation in as-prepared P3HT:$PC_{61}$BM solar cells.

### 6.1.4 Conclusion

From a temperature dependent study focused on nongeminate recombination in pristine and annealed P3HT:$PC_{61}$BM solar cells clear differences between both devices became apparent. The fine intermixed donor–acceptor morphology in as-prepared devices results in about one order higher nongeminate recombination rates than in annealed devices. The stronger increase of recombination order with decreasing temperature in pristine devices could also be related to the changes in morphology. The temperature dependence of the recombination prefactor $k$ appears in good accordance with the prediction of the Gaussian Disorder Model and a slightly higher ($\sigma^* \approx 59$ meV) energetic disorder was found in pristine than in annealed ($\sigma^* \approx 50$ meV) samples.

Furthermore, the impact of nongeminate recombination on the $j/V$ characteristics was investigated. A voltage dependent nongeminate loss current was determined and used in combination with a voltage independent photogeneration term to reconstruct measured $j/V$ curves. The perfect agreement of measured and reconstructed $j/V$ data identified nongeminate losses as the performance limiting loss mechanism in P3HT:$PC_{61}$BM solar cells. In addition, this revealed a field-independent charge generation in pristine and

annealed devices for the temperatures considered here.

## 6.2 Impact of Solvent Additive on PTB7:$PC_{71}BM$ Solar Cells

### 6.2.1 Introduction

While in the previous Sec. 6.1.3 the intensively studied and well optimized material combination of P3HT:$PC_{61}BM$ was investigated, the following part concentrates on the rather new, low band gap polymer PTB7 in combination with the fullerene $PC_{71}BM$. In recent years the power conversion efficiency of organic solar cells improved above 11% [122, 8] This performance enhancement is mainly due to the development of new low-band gap semiconductors, like PTB7 and their broadened absorption spectrum. Thus, these new material compositions deserve particular consideration in order to understand the crucial steps from photon absorption to photocurrent. In order to further improve device performance, identifying the performance limiting loss mechanisms is essential. As described in details in Chapter 3, on the one hand, geminate losses of bound electron–hole pairs compete with polaron pair dissociation. As electron–hole dissociation via an intermediate charge transfer state might require a certain activation energy to obtain free charges (see Ref. [33]) this process can be facilitated by an external electric field (Fig. 3.1). On the other hand, nongeminate recombination of free–free or trapped–free polarons after successful polaron pair dissociation depends on the charge accumulation in the device and, thus, relies on the applied voltage and respective current flow (Fig. 3.2). From the previous investigations on P3HT:$PC_{61}BM$ and from literature it is known that for polymer and small molecule based OSC both, nongeminate losses [75, 118] as well as geminate losses, [123, 124] can have a strong impact on the device performance and the shape of the $j/V$ characteristics.

### 6.2.2 Device Preparation & Measurements

Bulk heterojunction organic solar cells were prepared as described in detail in Sec. 4.6. The active layer was based on a PTB7:$PC_{71}BM$ 1:1.5 blend processed from a solution of pure chlorobenzene (CB) and from a combination of chlorobenzene (97%) and the co-solvent (additive) 1,8-diiodooctane (DIO, 3%). A semiconductor solution with a concentration of 20 mg/ml was used to realize 100 nm thick layers, reported as optimum thickness for this material composite [88]. As metal top contact calcium (3 nm) and aluminum (120 nm) were deposited by evaporation.

Prior to any additional measurements an Oriel 1160 AM1.5G solar simulator was used to perform illuminated $j/V$ measurements of devices kept under

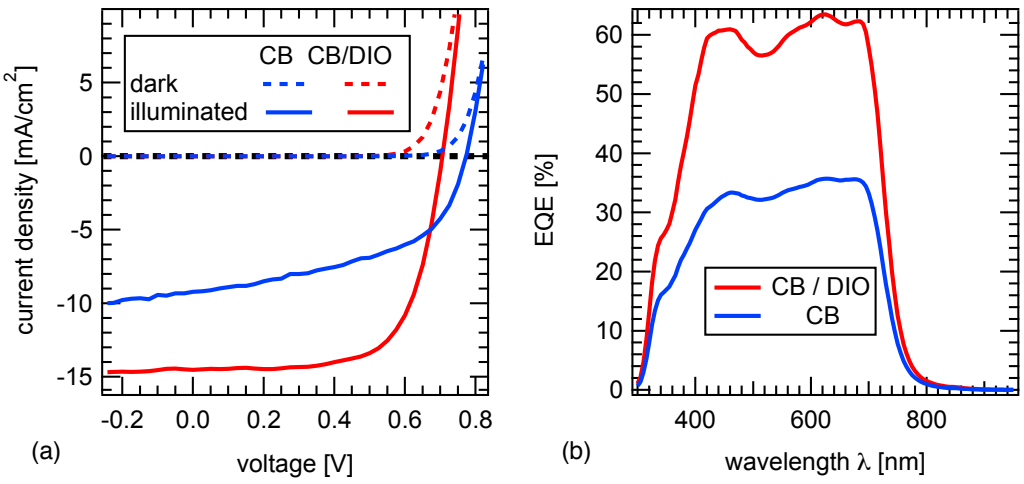


Figure 6.9: (a) Current–voltage response of a PTB7:$PC_{71}BM$ 1:1.5 solar cell, processed with and without DIO as additive under one sun simulated AM 1.5 spectrum at 300 K. (b) External quantum efficiency for both devices.

inert glovebox atmosphere. Furthermore, static and time-resolved studies, namely TPV, CE and TDCF were carried out in a closed cycle optical cryostat as described in detail in Chapter 4. The derived experimental data was treated as reported in Ref. [98, 125] and Sec. 6.1.3, while all charges were corrected for recombination losses during extraction as specified in Sec. 4.3.

### 6.2.3 Results

Two sets of organic solar cells, based on a PTB7:$PC_{71}BM$, were investigated differing only by the use of the solvent additive (see above). The influence of the co-solvent DIO on device performance becomes evident in the respective current–voltage response depicted in Fig. 6.9(a). Under one sun simulated illumination, the sample processed without additive yields an open circuit voltage of $V_{oc} = 770$ mV, a short circuit current density of $j_{sc} = 9.2$ mA/cm$^2$ with a fill factor of $FF = 51\%$ and a device efficiency of $\eta = 3.6\%$. In contrast, the device processed with DIO shows $V_{oc} = 710$ mV, $j_{sc} = 14.6$ mA/cm$^2$, a fill factor of $FF = 67\%$ and an almost twice as high PCE of $\eta = 7.0\%$. Significant improvement of fill factor and photocurrent is observed when using the additive, in accordance with earlier findings [88, 121, 89, 126]. From the external quantum efficiency a clearly enhanced yield for the device with additive is revealed, while the shape is rather constant (see Fig. 6.9(b)). The

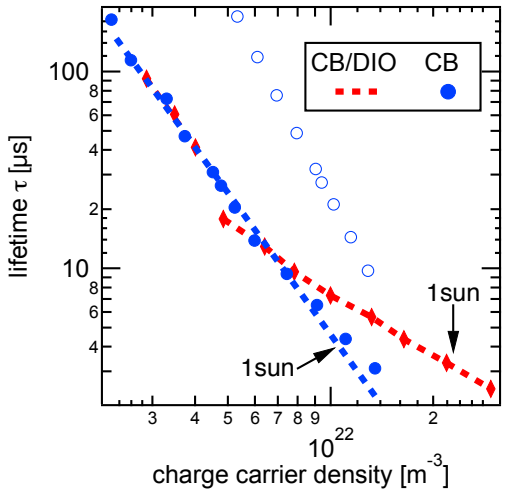


Figure 6.10: Charge carrier lifetime $\tau$ derived from TPV measurements as a function of charge carrier density $n$ from CE for PTB7:$PC_{71}BM$ solar cells processed from chlorobenzene solution and from a combination of chlorobenzene and 1,8-diiodooctane. Diamonds and filled circles represent experimental data points, while the dashed line demonstrates the fit according to $\tau(n) = \tau_0 n^{-\lambda}$. The data points represented by blue open circles are based on a charge carrier density theoretically calculated as described in the discussion.

chosen additive DIO is rather effective to influence the PTB7:$PC_{71}BM$ composite, as it has a high boiling point and selectively dissolves $PC_{71}BM$, which was reported in Ref. [127] to enable fullerene intercalation into the polymer network during film formation.

In the following, the differences in nongeminate and geminate recombination dynamics for both device types are presented in order to investigate the origin of the dramatic change of $j_{sc}$ and $FF$. The nongeminate recombination rate $R$ of photogenerated charge carriers is empirically defined according to Eq. (3.4). In order to determine the nongeminate recombination rate experimentally, TPV and CE experiments under open circuit conditions were applied. As discussed in literature and in Chapter 5, from the small perturbation charge carrier lifetime $\tau_{\Delta n}$ the total charge carrier lifetime $\tau(n)$ is accessible by TPV (see Eq. 5.8) [99, 118]. The average charge carrier density $n$ under open circuit conditions is derived by CE. The data is corrected for the geometric capacitance (see further details in discussion) and, iteratively, for charges lost by recombination during extraction [82, 118]. In Fig. 6.10, TPV and CE are combined to yield the charge carrier lifetime $\tau$ as a function of charge carrier density under open circuit conditions.

For both device types a power law dependence according to $\tau(n) = \tau_0 n^{-\lambda}$

is found: In the low charge carrier density regime, the $\tau(n)$ values coincide, correspondingly yielding the same slope ($\lambda \approx 2.4$) for both devices. However, at higher carrier densities the device with additive shows a reduced slope with $\lambda \approx 1.1$. For the device without DIO only a minor change in slope becomes apparent. According to Ref. [72] and as discussed in the previous Chapter 5, an activation energy $E_u$ characterizing the exponential trap distribution can be estimated from the parameter $\lambda$ [125]. For low charge carrier densities $E_u \approx 2\lambda \cdot kT/n_\tau = 51$ meV is found. This indicates trap limited recombination for the device processed without additive and in the low charge carrier regime of the device prepared from CB/DIO. Above $n = 10^{22}\ m^{-3}$ direct (Langevin–type) recombination of free charge carriers is expected, as the apparent recombination order $\lambda + 1$ is about 2 at 300K. For an illumination equivalent to one sun, the nongeminate charge carrier lifetime for the device processed without additive is slightly longer than for the one with additive (see arrows in Fig. 7.4(b)).

The influence of geminate recombination was studied by time delayed collection field (TDCF) measurements by investigating the total extracted charge $Q_{tot}$ under a range of prebias voltages. These experiments were performed under very low fluences to avoid nongeminate recombination [50] (further experimental details in Sec. 4.4). In Fig. 6.11 the normalized total charge $Q_{tot}(V)/Q_{tot}(-5\text{V})$ is plotted versus the prebias voltage applied during the delay time $t_d$ (380 ns). While the extracted total charge is rather constant for the device with additive, a clear voltage dependence for the sample processed from CB becomes apparent. Relevant in terms of solar cell performance is the voltage regime between $V = 0$ V and $V_{oc}$: A voltage dependent photogeneration is equivalent to geminate losses, which are quantified by the polaron pair dissociation probability PP($V$). A polynomial fit over the complete voltage range was used to find an analytical approximation for PP($V$) between short and open circuit conditions.

To understand the impact of geminate and nongeminate recombination on the performance of the device, the $j/V$ reconstruction was applied, in analogy to Sec. 6.1 and to recent studies on P3HT:$PC_{61}BM$ as well as small molecule based devices in literature [75, 118, 123]. The procedure is described in detail in Sec. 3.3. The steady state current density $j/V$ of the device is described by integrating the continuity equation (Eq. 3.5) for charge carriers yielding Eq. (3.8).

In order to calculate the voltage dependent nongeminate loss current $j_{loss}(V)$ from $V = 0$ V to $V_{oc}$, CE experiments under the desired voltage were performed, in analogy to the measurements at $V_{oc}$ described on page 66. All voltages were corrected for the series resistance $R_s$ by calculating $V = V_{app} - R_s I$. From the ohmic range of the dark $j/V$ curve, the

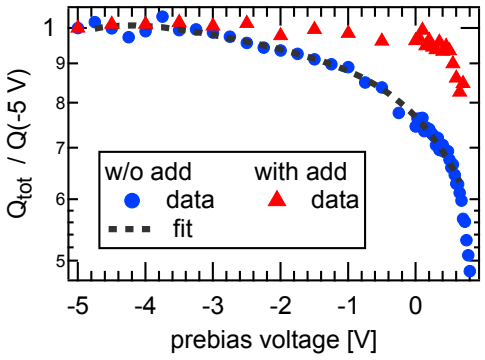


Figure 6.11: Normalised total extracted charge $q_{tot}$ from TDCF measurements in dependence on the applied prebias voltage for the device with and without additive.

values $R_s \approx 84\ \Omega$ for the device with additive and $R_s = 105\ \Omega$ for the one without additive were derived. The voltage dependent charge carrier density for both devices is shown in Fig. 6.12 for three different light intensities.

The $n(V)$ relation and the dependence of $\tau$ on $n$ found under $V_{oc}$ conditions (Fig. 6.10) are used to calculate the charge carrier density dependent recombination rate $R(n(V))$ for the respective applied voltage by Eq. (3.4). This data was fed into Eq. (5.14), which allowed to determine the nongeminate recombination current $j_{loss}(n(V))$.

As the photogeneration of the sample with additive was voltage independent, as shown in Fig. 6.11, the respective generation current $j_{gen}$ was assumed to be constant and set equal to the short circuit current density,

$$j_{gen} \approx j_{sc}, \tag{6.5}$$

similar to the case of P3HT:$PC_{61}BM$ (Sec. 6.1) and the approach in Ref. [75, 118].

Instead, for the solar cell fabricated from pure CB solution, the voltage dependent polaron pair dissociation PP($V$) derived by TDCF is substantial (see Fig. 6.11 blue). It was considered for the reconstruction by a voltage dependent generation current

$$j_{gen}(V) = j_{sc} \cdot \mathrm{PP}(V). \tag{6.6}$$

The term PP($V$) was derived from the polynomial fit (Fig. 6.11, dashed line) described above and accounts for the relative charge photogeneration between $V = 0$ V and $V = V_{oc}$. In order to calculate the $j/V$ response for both device types, either Eq. (6.5) or Eq. (6.6) were entered into Eq. (3.8) for the device

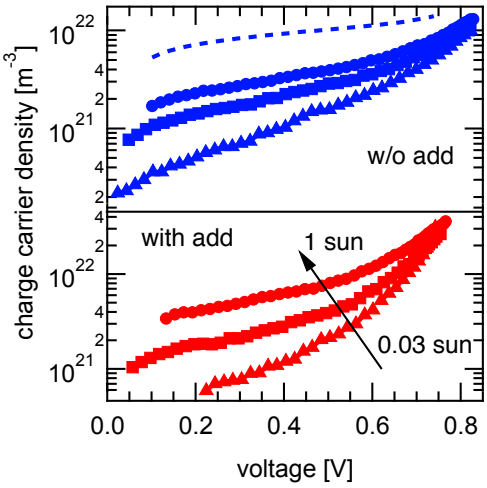


Figure 6.12: Voltage dependent charge carrier density $n(V)$ from charge extraction experiments for PTB7:$PC_{71}BM$ devices with and without additive at three different light intensities. Blue dashed line: theoretical charge carrier density data of one sun illumination, required for a successful $j/V$ reconstruction (see discussion below).

processed with or without additive, respectively. Hereby gained $j/V$ data perfectly agrees with the measured data for the device with additive for three light intensities presented (Fig. 6.13(a)). Instead, although experimentally determined geminate and nongeminate losses were considered, the reconstruction of the device processed from pure CB shows significant deviations from the measured $j/V$ characteristics (Fig. 6.13(b)).

### 6.2.4 Discussion

The application of the co-solvent 1,8-diiodooctane results in a dramatic change of the active layer morphology (see Fig. 6.14 and Ref. [126, 128]) and also in a considerably improved device performance (Fig. 6.9(a)), mainly related to an enhanced photocurrent (Fig. 6.9(b)). For the present material systems the additive leads to a more uniform morphology and the formation of an interpenetrating network [129]. For a devices processed without DIO a large phase separation is present and isolated fullerene domains can be supposed from AFM phase diagrams (Fig. 6.14) as well as from AFM/TEM studies in literature [129, 127, 126]. A much smoother surface topography for the device processed with DIO becomes apparent from the height profile.

Despite the described morphological differences, TPV and CE studies revealed similar charge carrier lifetimes and, thus, comparable nongeminate re-

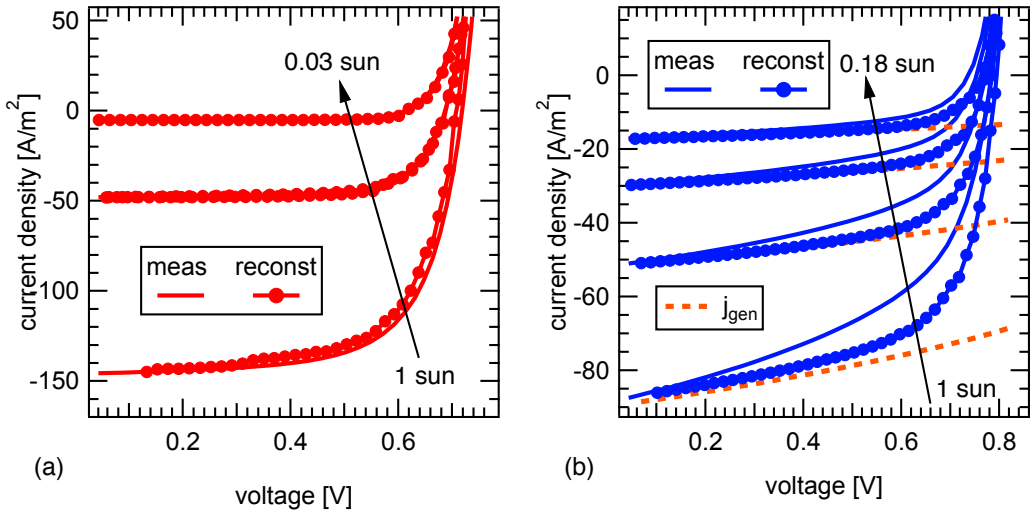


Figure 6.13: (a) Measured and reconstructed current–voltage response of a PTB7:$PC_{71}BM$ 1:1.5 solar cell, processed with and (b) without DIO as additive for different illumination intensities at 300K. In (b) the generation term $j_{gen}$ varies with voltage with respect to the TDCF findings (see Fig. 6.11).

combination rates for both devices at low charge carrier densities. For carrier concentrations above $n = 10^{22}\mathrm{m}^{-3}$ the lifetime values of both devices no longer coincide (see Fig. 6.10). In order to determine the nongeminate recombination yield by TPV/CE measurements, it was assumed that all charges participating in the recombination process are encompassed in the CE transient. This assumption can be critical if isolated domains are present, which is discussed below.

Concerning the charge photogeneration, from prebias dependent TDCF measurements a field-assisted dissociation of polarons is found for the device processed without additive, while the device prepared with DIO shows a rather constant separation yield [130]. For the former device, we find about 20% less generation close to $V_{oc}$ than under short circuit conditions. The difference in polaron pair dissociation is in good agreement to earlier results of Brenner *et al.* They observed a stronger field dependence of photocurrent generation in PTB7 relative to the fullerene for devices processed without additive [121]. The field dependence was recently discussed in context of reduced LUMO energy levels of $PC_{71}BM$ molecules being dispersed in a polymer matrix [126]. Due to higher electron affinity of fullerene agglomerates compared to dispersed molecules [131], a good intermixing and a direct contact of fullerene agglomerates to a polymer matrix phase may be essential for efficient electron–hole

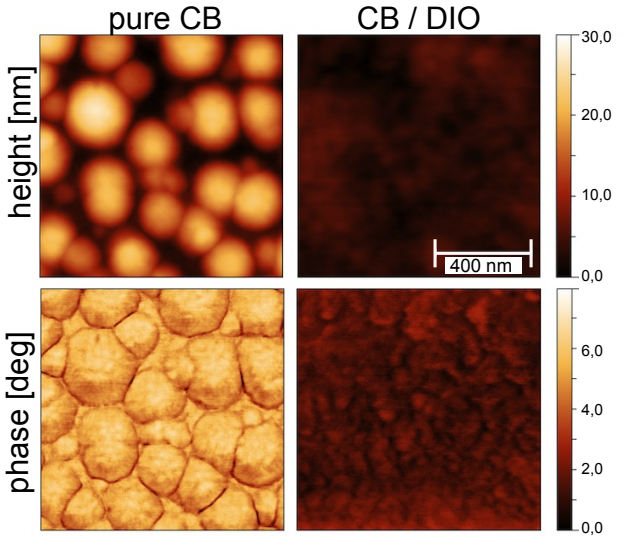


Figure 6.14: Height and phase AFM images of both, the device processed from pure CB solution and from CB and DIO as co-solvent. From the height image a smoothening for the device processed with additive becomes apparent. The variation of several degrees in the phase diagram of the sample processed without additive indicates two different material regions. We assume a pure fullerene phase of up to 200 nm in size embedded in a matrix mix-phase of polymer and fullerene as described in Ref. [126].

separation. Thus, charge photogeneration is facilitated in the well intermixed system created by the use of an additive, and under these conditions geminate recombination can be neglected. For the device processed without additive a field-assisted charge generation becomes apparent. From TDCF measurements the voltage dependent dissociation probability PP(V) between $V = 0$ V and $V_{oc}$ was derived by a polynomial fit.

For the device with additive reconstructed and measured $j/V$ data coincide almost perfectly, as shown in Fig. 6.13(a): Both, fill factor and $V_{oc}$ are reproduced quite accurately for all light intensities. As only nongeminate losses were considered to reconstruct the $j/V$ behavior, they are identified as the dominant loss process responsible for device performance limitation.

In case of the device processed from pure CB, both field-dependent photogeneration and nongeminate recombination limit the performance. However, considering both loss mechanisms, the reconstructed $j/V$ data overestimates the device performance (Fig. 6.13(b)). This discrepancy stems from an underestimation of either geminate or nongeminate losses.
The degree of geminate recombination was verified by TDCF measurements at different delay times (10 ns up to 380 ns) and excitation energies, but the deter-

mined PP($V$) dependence remained virtually unchanged [130]. Thus, PP($V$) and the derived photogeneration current $j_{gen}(V)$ are expected to be determined exactly, at least as long as the dissociation of polaron pairs takes place within 380 ns. It is known from other low-band gap polymers like PCPDTBT or PCDTBT that CT decay / dissociation times of less than 10 ns is a credible assumption [132, 66, 133].

Apparently, determining the nongeminate loss current $j_{loss}$ requires more assumptions and, therefore, bears more uncertainty. The experimentally determined nongeminate recombination rate $R(n)$ stems from TPV/CE measurements under open circuit conditions. It is assumed not to be explicitly dependent on voltage. A voltage dependent recombination rate might be due to a field-dependent mobility, with a negative voltage coefficient reported in some blend compositions [134, 135]. Also, spatial variations of the charge carrier density cannot be resolved in CE experiments. If gradients are present, they are more pronounced towards $V = 0$ V than around $V_{oc}$ [77]. However, both effects—a potentially field-dependent mobility and significant charge carrier gradients—would lead to an overestimation of the nongeminate recombination rate, not an underestimation. Therefore, they cannot be responsible for the apparent overestimation of device performance.

An alternative which could potentially explain the discrepancy between measured $j/V$ characteristics and the reconstruction for the device without additive is given in trapped charges (photogenerated or intrinsic) in spatially isolated domains, i.e., without percolation pathways to the respective electrode. These trapped charge carriers could recombine with mobile charge carriers at the organic–organic interface influencing the apparent recombination rate. However, they can not contribute directly to the charge transport, and could not therefore be observed in charge extraction experiments. Consequently, the calculated nongeminate loss current $j_{loss}$ (see Eq. (5.14)) would be underestimated, leading to an overestimated reconstruction of the photocurrent (see Eq. (3.8)). This scenario is very likely for solar cells prepared without the co-solvent.

Indeed, a combination of resonant X-ray scattering and microscopy as well as AFM images (Fig. 6.14) revealed 50-200 nm pure $PC_{71}BM$ domains in devices processed without additive [126] favoring a trapping process as described above. In Fig. 6.12, theoretical charge carrier density data $n(V)$, required for a successful $j/V$ reconstruction of one sun illumination, was exemplarily added for the device processed without additive (blue dashed line). Also, the correspondingly shifted effective lifetime in dependence on the theoretically necessary charge carrier density at $V_{oc}$, $\tau(n)$, is shown in Fig. 6.10 for the same device (blue open circles). Both representations illustrate that a considerable amount of trapped charges contributes to the nongeminate loss current.

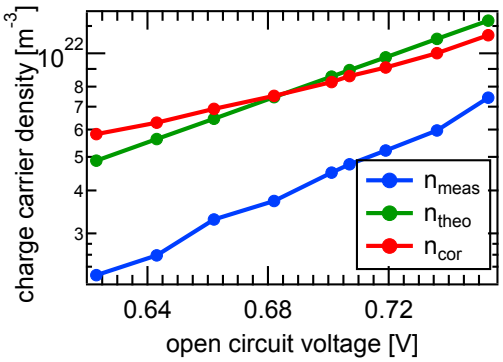


Figure 6.15: Measured (blue), corrected by geometric capacitance (red) and theoretically calculated charge carrier density (green) for various voltages $V_{oc}$ and the device processed without additive.

Further evidence that trapped charges are the origin of the apparent deviation is given by dark capacitance measurements in the following. CE experiments in the voltage range $-0.35\ \mathrm{V} < V < -0.05\ \mathrm{V}$ were applied to determine an experimental dark capacitance of $C_{dark} = 3.37$ nF, which is about 47% higher than the expected geometric capacitance ($C_{geo} = \varepsilon\varepsilon_0\frac{A}{d}$) roughly estimated by assuming a realistic, effective dielectric constant $\varepsilon = 3.7$ as well as the measured thickness ($d = 130$ nm) and active area ($A = 9.12\ \mathrm{mm}^2$) of the device. A likely scenario is that not only the geometric capacitance, but also spatially trapped charge carriers in isolated material (fullerene) domains contribute to the dark capacitance. As $C_{dark}$ is used to correct all transients from illuminated CE experiments, this would reduce the determined charge carrier density in the bulk, relevant for nongeminate recombination. In Fig. 6.15 three different charge carrier densities are plotted versus $V_{oc}$.

In blue the charge carrier concentration corrected by the measured dark capacitance is depicted, while in red the same experimental data, but corrected by the geometric capacitance $C_{geo}$ is shown. The green data points are reconstructed by the following assumptions: Geminate loss are estimated to 20% between V = 0 V and $V_{oc}$ from TDCF measurements (see Fig. 6.11). Thus, $j_{gen} = 0.80 \cdot j_{sc}$ is assumed.

Furthermore, all generated charges at $V_{oc}$ are expected to be lost by nongeminate recombination and therefore $j_{gen} = j_{loss} = \frac{n_{theo}}{\tau}$. This enables to calculate $n_{theo}$ (green data). It turns out that a reduction of $C_{dark}$ to meet the estimated capacitance of a plate (planar dielectric) with $\varepsilon = 3.7$ leads to charge carrier densities in the same range as necessary for successful $V_{oc}$ reconstruction, as evident from Fig. 6.15. Consequently, CE data corrected by $C_{dark}$ underestimates $n(V_{oc})$ as traps in the bulk lead to an apparent higher

capacitance.

### 6.2.5 Conclusion

In a detailed study the transient methods of TPV, voltage dependent CE and TDCF were applied to PTB7:$PC_{71}BM$ bulk heterojunction solar cells to analyze the origin of performance limitation and the origin of the positive impact of the co-solvent 1,8-diiodooctane (DIO). In devices processed with DIO, a voltage independent charge photogeneration was found and discussed with respect to a reduced LUMO energy of $PC_{71}BM$ molecules dispersed in a polymer matrix. The performed $j/V$ reconstruction agreed perfectly well with the measured response. This finding allowed us to identify nongeminate recombination as the performance limiting loss mechanism for the device with DIO. In contrast, devices processed from pure CB solution showed both, severe geminate and nongeminate losses. A strong deviation of measured and reconstructed $j/V$ characteristics became apparent, which was discussed with respect to spatially trapped charge carriers in isolated pure $PC_{71}BM$ domains. It was argued that those trapped charge carriers can explain the discrepancy in the $j/V$ reconstruction. In addition, this interpretation was supported by measurements of the dark capacitance and comparison with the geometric capacitance.

Chapter 7

# Planar vs. Bulk heterojunction

In this final chapter the two main active layer architectures of OPV—planar and bulk heterojunction organic solar cells—are compared in view off differences in device performance and charge carrier decay dynamics. As material system of choice the small molecule CuPc and the fullerene $C_{60}$ are deposited by thermal evaporation. Experimental techniques such as transient photovoltage and charge extraction are used in combination with macroscopic device simulations (carried out by A. Wagenpfahl) for the following investigations. Main parts of this section are published in Paper 4.

## 7.1 Introduction

The previous chapters dealt with solution processed bulk heterojunction organic solar cells [24], in which the active layer is composed of a blend of two organic semiconductors, one acting as electron donor, the other as electron acceptor. A promising power conversion efficiency of 7.0% was shown (see Fig. (6.9(a))) for the material system PTB7:$PC_{71}BM$. An alternative layer composition next to the BHJ is the planar heterojunction (PHJ), with two adjacent thin layers of donor and acceptor. A PHJ device was indeed the first organic photovoltaic cell with reasonable efficiency as reported by Tang in 1986 [23]. The PHJ approach, however, has not been able to yield the highest reported efficiencies in recent years, although a notable 5.24% have been achieved recently for a tetraphenyldibenzoperiflanthene (DBP)/$C_{60}$ bilayer [136]. The previous chapters were focused on the charge carrier dynamics in BHJ systems as it was also the matter in various publications by other groups in the past [137, 138, 74]. Despite an expected bimolecular charge carrier decay with a quadratic dependence of the recombination rate on charge carrier density, an empirically found apparent order of decay higher than two is found (see Fig. 6.3 (a) and the drawn conclusion in Section 6.1.2) and discussed in view of a capture and release process of charge carriers into and from trap states, respectively [139, 73, 140, 66, 72, 112]. Thereby, the complex donor–acceptor morphology and its influence on the charge carrier dynamics complicate the interpretation of experimental findings, leading to debates among several research groups concerning the origin of the slow nongeminate

recombination. To gain more insight into the impact of phase separation on charge recombination, a BHJ and a PHJ solar cell in direct comparison were investigated in the following.

## 7.2 Device Preparation & Measurements

Devices reported on in this chapter were prepared at the IMEC institute in Belgium and shipped to Würzburg under nitrogen atmosphere for further studies. As preparation conditions differ from those mentioned in Sec. 4.6 the respective steps are briefly listed.

Pre-patterned ITO covered glass substrates (kintec, $< 20$ ohm/square) were thoroughly cleaned (soap, deionized water and solvents). The substrates undergo a 15 minutes UV-ozone treatment prior to the depositions of the organic materials. The organic materials bathocuproine (BCP, Aldrich), copper-phthalocyanine (CuPc, Aldrich) and fullerene ($C_{60}$ from SES-research) are purified at least once using thermal gradient vacuum sublimation. The materials are deposited in a high vacuum chamber (base pressure $< 10^{-6}$ Torr) using thermal evaporation, with an evaporation rate around 0.5-1.0 Å/s. Acceptor/donator thickness of the planar device were set to 25/25 nm. The ratio of the blended CuPc/$C_{60}$ layer is kept constant at 1:1. The top contact (Ag) is deposited in the same vacuum chamber, and it defines a cell area of 3 mm$^2$.

Both cell types were studied by TPV and CE measurements under different light intensities, while detailed explanation on the techniques can be found in Section 4. Due to negligible influence of recombination during charge extraction for this material system the measured charge carrier densities were not corrected for these losses. Densities per area were calculated by considering the active layer area instead of volume.

In order to support the experimental data macroscopic device simulations performed by an organic solar cell simulation software were applied, written and carried out by A. Wagenpfahl. The simulation software is based on solving the differential equation system of Poisson, continuity and drift–diffusion equations [141, 142, 59]. The light excitation profile was calculated by a transfer matrix method generating excitons in a pure semiconductor and polaron pairs in blended materials, respectively [141]. The illumination was set to an AM1.5 spectrum. If an exciton diffuses to a heterointerface within its lifetime it gets converted to a polaron pair. The following generation and recombination dynamics were described by the Braun–Onsager and Langevin theory [39, 68]. By fitting the $j/V$ characteristics of a PHJ and a BHJ device under illumination and in the dark (see Fig. (7.1)), the simulation parameters within the experimental validated regime are acquired and summarized

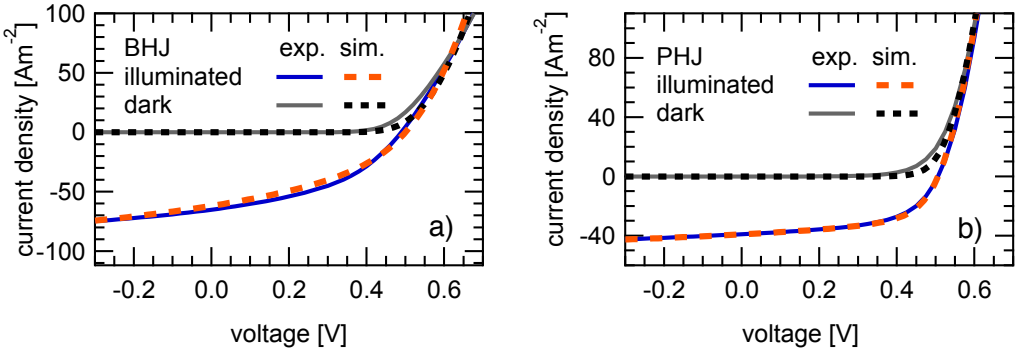


Figure 7.1: Dark and illuminated (one sun intensity) current–voltage characteristics for the bulk heterojunction (a) and the planar heterojunction (b) organic solar cell including respective fits on the experimental data. The fits enable to extract device simulation parameters (see Table B.1) required for further analysis.

in Table B.1 of the appendix. Except the mobility it was a main focus to use equal parameters for both device architectures to account for the same material composition. The LUMO and HOMO levels of CuPc and $C_{60}$ are in accordance with Ref. [143]. An effective blend was created combining the energy level $\mathrm{HOMO}_{CuPc}$ with $\mathrm{LUMO}_{C_{60}}$. Additionally, the thickness of the BHJ active layer was reduced from 50 nm to 45 nm, still within the preparation error. The absolute value for the decay rate $k_r$ used within the Braun–Onsager model should not be overestimated, as it includes microscopic instead of directly measurable parameters, e.g. high local mobilities required for effective charge separation [144, 47]. The exciton diffusion length was set to a value larger than the spatial extent of the active layers.

## 7.3 Results

Several planar and bulk heterojunction solar cells with the same active layer thickness of overall $d = 50$ nm were prepared, all yielding similar $j/V$ characteristics. Both CuPc/$C_{60}$ cell types were processed in one run, neglecting to optimize the thickness in view of an increased performance. For the CE and TPV measurements representative samples were selected and the $j/V$ characteristics for one sun is depicted in Fig. 7.1. The power conversion efficiency of the PHJ was $\eta = 1.1\%$, yielding a short circuit current density of $j_{sc} = 3.9$ mA/cm$^2$, an open circuit voltage of $V_{oc} = 507$ mV and a fill fac-

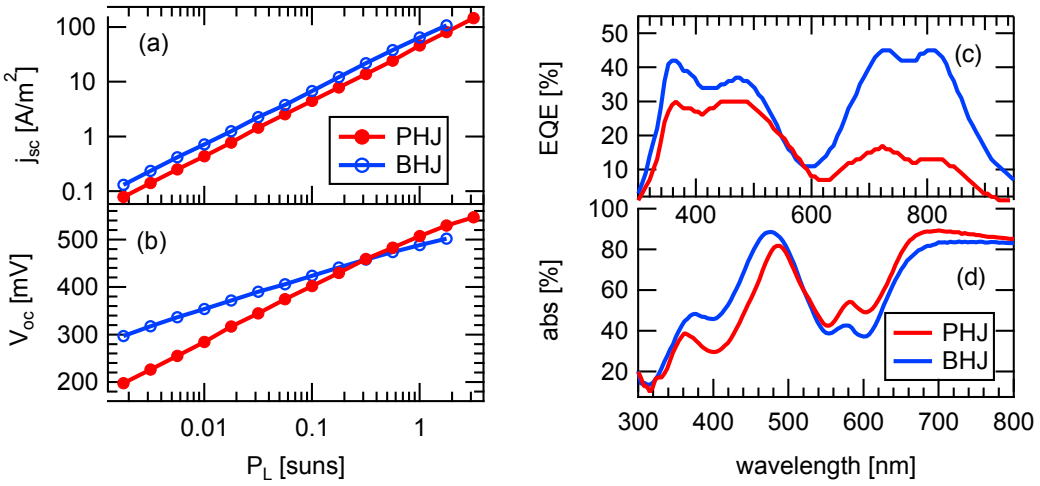


Figure 7.2: Comparison of a PHJ and a BHJ solar cells based on the materials CuPc and $C_{60}$ at room temperature as a function of bias light: (a) short circuit current density $j_{sc}$ and (b) open circuit voltage $V_{oc}$ as well as EQE (c) and absorption spectra (d).

tor of $FF = 55\%$ at room temperature and one sun illumination intensity. Under equivalent conditions the BHJ yielded $\eta = 1.4\%$, $j_{sc} = 6.5$ mA/cm$^2$, $V_{oc} = 488$ mV and $FF = 43\%$. In Figure 7.2, $j_{sc}$ and $V_{oc}$ of PHJ and BHJ solar cells are compared in dependence on incident light intensity. Thereby, $j_{sc}$ is significantly higher in the BHJ than in the PHJ device for all light intensities (Fig. 7.2 (a)). In view of the external quantum efficiency (EQE) and the absorption profile shown in Fig. 7.2(c),(d) this is not surprising. Specially a reduced contribution of CuPc in the EQE of the bilayer configuration in the wavelength range above 550 nm becomes apparent, probably related to the limited exciton diffusion length limiting charge photogeneration in PHJ devices. In contrast, the open circuit voltage (Fig. 7.2 (b)) is found to be lower in the PHJ for low light intensities, but exceeds the voltage of the BHJ for light intensities above 0.3 suns. Similar results of $V_{oc}(P_L)$ are shown in Ref. [145] and discussed with respect to the different ideality factors for both device structures, although without going into detail. As the open circuit voltage is determined by the balance of charge carrier generation and recombination, $G = R$, transient photovoltage and charge extraction measurements to study nongeminate recombination under open circuit conditions are used to further analyze this finding.

In Figure 7.3(a) we present the results of TPV measurements on the PHJ

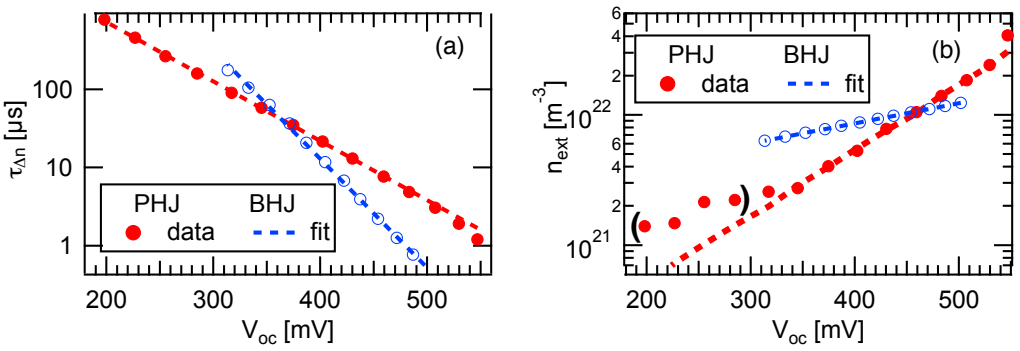


Figure 7.3: (a) Small perturbation charge carrier lifetime $\tau_{\Delta n}$ and (b) charge carrier density versus open circuit voltage $V_{oc}$ for CuPc/$C_{60}$ based planar and bulk heterojunction organic solar cells.

and BHJ device. TPV, introduced in detail in Chapter 4, is based on monitoring the photovoltage decay upon a small optical perturbation during various constant bias light conditions [70]. From the voltage transient, the small perturbation charge carrier lifetime $\tau_{\Delta n}$ is extracted in dependence of the respective open circuit voltage due to the constant background illumination. Figure 7.3(a) depicts an exponential dependence of $\tau_{\Delta n}$ on the open circuit voltage $V_{oc}$ similar to TPV studies on polymer:fullerene bulk systems shown in Chapter 5, 6 or in literature in the past [70, 73, 92]. This finding is valid for both architectures, the present CuPc/$C_{60}$ PHJ and the CuPc:$C_{60}$ BHJ device. A steeper slope is observed for the BHJ. The variation of the effective charge carrier lifetime with light intensity indicates a nongeminate loss mechanism for both device architectures.

In order to analyze the charge carrier dynamics, the number of charge carriers participating directly in the recombination process is required. Within the effective medium approach for BHJ devices, the charge carrier density profile can be approximated to be spatially uniform within the active layer. Spatial variations in the charge carrier generation are compensated to a certain degree by a diffusive current transport. Thus, the charge carrier densities can be measured by the straightforward charge extraction (CE) technique (see Chapter 4 and the results in Chapter 5, 6). The situation is different in PHJ devices: polaron generation and recombination are very nonuniform [146], i.e., localized at the planar donor–acceptor heterointerface. Considering the TPV technique as example, the photovoltage rise upon laser excitation is based on charge carriers successfully generated at the planar donor–acceptor interface from the primary photoexcitations. The subsequent charge carrier decay is

proportional to the nongeminate recombination of electron and hole at this interface, not to the overall charge carrier concentration. Thus, only charge carriers at the interface ($n_{int}$) are relevant for the charge carrier decay analysis in PHJ solar cells.

Nevertheless, for comparison CE measurements were also performed on the PHJ system. As the contribution of capacitive charges is even more dominant for PHJ, the corresponding correction (described in details in Sec. 4.3) becomes more important. The density of extracted charge carriers $n_{ext}$ was calculated assuming in first approximation a constant (uniform) charge carrier distribution in analogy to the BHJ device (see Sec. 4.3) and appears exponentially dependent on $V_{oc}$ (see Fig. 7.3(b)). It is noted that this is in contradiction to the findings of Credgington *et al.* [147], who found a linear dependence of $n_{ext}$ on $V_{oc}$ in pentacene/$C_{60}$ bilayer devices due to the dominating geometric capacitance. The exponential dependence depicted in Fig. 7.3(b) suggests that the chemical capacitance of the present active material CuPc/$C_{60}$ provides a stronger contribution to the total amount of charges at a certain light intensity than the dielectric plate capcacitance. In comparison to the BHJ device, the data derived from the planar device is stronger dependent on $V_{oc}$.

As mentioned before, the approximation of a uniform charge distribution in PHJ devices might not be precise enough to describe the decay dynamics exactly. The relevant quantity, the charge carrier concentration at the interface $n_{int}$ cannot be determined directly, e.g. by the CE technique. Thus, a different approach is needed.

Based on a model introduced in Ref. [146] the open circuit voltage $V_{oc}$ in PHJ solar cells depends—in addition to material constants such as the effective band gap energy $E_g$ and the effective density of states $N_D$—only on the charge carrier concentration $n_{int}$ at the planar interface [146],

$$V_{oc} = \frac{E_g}{q} - \frac{n_{id}kT}{q} \ln\left(\frac{N_D^2}{n_{int}^2}\right). \tag{7.1}$$

For the sake of simplicity the effective density of states $N_D$ as well as the interface charge carrier density $n_{int}$ were assumed to be equal in donor and acceptor. Furthermore, $q$ is the elementary charge, $kT$ the thermal energy and $n_{id}$ the ideality factor. In Ref. [146] Eq. (7.1) was derived by considering the position dependent charge concentration and the related field distribution. Assumptions such as thermionic emission at the contacts and disregard of doping or trapping lead to a simplified expression for $V_{oc}$ in PHJ devices, implicitly representing the charge/field distribution across the device. Within the model, band bending compensates for the energy losses at the contacts.

The effective band gap energy $E_g$ is found to be rather independent of device architecture and was determined from $V_{oc}(T)$ of the BHJ device to be

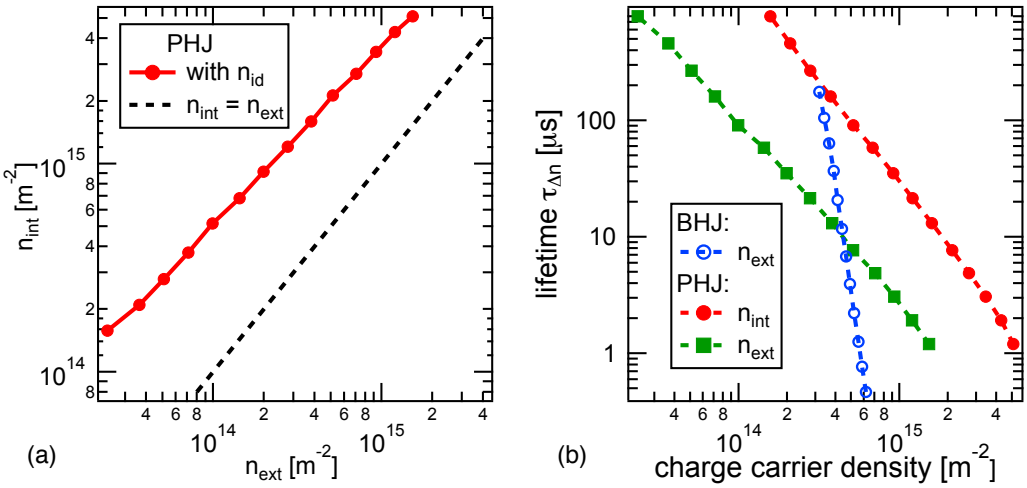


Figure 7.4: (a) Charge carrier concentration in the PHJ solar cell at the donor–acceptor interface $n_{int}$ calculated by Eq. (7.2) vs. the charge carrier density extracted from CE measurements, $n_{int}$. The black dashed line represents the case $n_{int} = n_{ext}$, which would imply that there are no significant charge carrier gradients. (b) Small perturbation charge carrier lifetime $\tau_{\Delta n}$ vs. respective carrier densities of the bulk heterojunction (blue), of the planar heterojunction experimentally determined (green) and the theoretically calculated interface carrier density (red).

$E_g \approx 1.03$ eV. Thereby, $V_{oc}$ turned out to be limited by injection barriers $\Phi$ below T=250 K, roughly estimated as $\Phi \gtrsim 0.2$ eV according to Ref. [98]. A 2-dimensional density of states $N_{D_{2d}} = 6.3 \cdot 10^{17}$ m$^{-2}$ at the heterointerface was derived from the 3-dimensional density $N_D$ of the macroscopic simulation (see Table. B.1) by $N_{D_{2d}} = N_D^{2/3}$. Accordingly, $n_{int}$ has the unit m$^{-2}$ as well. The ideality factor is determined from $V_{oc}$ vs. $\ln(j_{sc})$ data as described in Chapter 5 and Ref. [96] and found to be $n_{id} \approx 1.94$. Eq. (7.1) solved for $n_{int}$ leads to

$$n_{int} = N_D \exp \frac{(qV_{oc} - E_g)}{2n_{id}kT}, \tag{7.2}$$

which enables to calculate the charge carrier density at the planar interface, $n_{int}$, from the measured open circuit voltage. In Fig. 7.4(a), $n_{int}$ is compared to $n_{ext}$. The latter was determined by CE as described above. In order to realize a 2-dimensional density $n_{ext}$ was multiplyed by the active layer thickness. Focusing on nongeminate recombination, the respective small perturbation carrier lifetimes $\tau_{\Delta n}$ of PHJ and BHJ as a function of charge carrier density are depicted in Fig. (7.4(b)). In order to allow a comparison with the calculated

interface charge carrier density $n_{int}$ (see Eqn. (7.2)), the respective densities $n_{ext}$ of PHJ and BHJ are both represented per area instead of volume, as described above.

## 7.4 Discussion

### 7.4.1 Recombination

The short circuit current density $j_{sc}$ of the CuPc/$C_{60}$ BHJ solar cell is higher than for the PHJ for all light intensities studied, although the dependence on the illumination intensity is similar as shown in Fig. 7.2 (a). From the absorption profile in Fig. 7.2 (d), a similar absorption yield in both device architectures becomes apparent. Meanwhile a reduced EQE for the planar compared to the bulk device in the wavelength range 550 nm $< \lambda <$ 800 nm is found, as depicted in Fig. 7.2 (c). One possible explanation is that the charge generation in the pure, 25 nm thick, CuPc layer is limited by the exciton diffusion length $d_{ex}$. Depending on the CuPc crystal size $d_{ex}$ is in the range of 15 nm $< d_{ex} <$ 20 nm [148, 149]. For this reason, the enhanced exciton splitting rate in BHJ devices due to the well distributed heterointerface results in a higher maximum current output (see Fig. 7.2 (a)). The charge transport within the spatially disordered photoactive layer of the BHJ device does not seem to limit the current output significantly. Koster *et al.* presented a rough estimate of nongeminate charge losses under short circuit conditions by the relation $j_{sc} \propto P_L^{\alpha}$. Assuming that the generation rate of free charges is proportional to light intensity the bimolecular recombination loss efficiency is defined by $\eta_{BR} = \alpha^{-1} - 1$ [105]. For the present material system this approach reveals negligible losses of about 1.5% in the BHJ device.

The situation is different for the open circuit voltage, as depicted in Fig. 7.2 (b). At lower light intensities, $V_{oc_{PHJ}} < V_{oc_{BHJ}}$, whereas from 0.3 suns onward the situation is reversed. Open circuit conditions are equivalent to $G = R$, i.e., the differences in open circuit voltage for PHJ and BHJ can be explained by the different recombination rates.

As pointed out above, in PHJ predominantly the charge carrier density at the heterointerface $n_{int}$ is relevant for the nongeminate recombination process. The almost linear dependence of $n_{int}$ on $n_{ext}$ (Fig. 7.4(a)) suggests the majority of photogenerated charge carriers reside at the planar heterointerface. This implies a strong carrier concentration gradient from the metal–semiconductor interface towards the donor–acceptor interface for low light intensities. However, at higher illumination intensities, the concentration of photogenerated charge carriers increases strongly at the heterointerface, reducing the diffusion

current, which ultimately leads to the carrier gradient pointing away from the interface [146].

In Fig. 7.4(b) the small perturbation charge carrier lifetime $\tau_{\Delta_n}$ in dependence on a 2-dimensional charge carrier density of PHJ and BHJ devices are directly compared. Both show a decreasing lifetime with increasing charge carrier density. This behavior was already discussed for polymer:fullerene solar cells in Chapter 6 (see Fig. 6.2(a)) and in literature [70, 73, 92]. For high charge carrier densities the photogenerated charge carriers in the PHJ have a longer lifetime than in BHJ devices, indicating the strong impact of the device architecture. This behavior can be explained by diffusion of charge carriers away from the heterointerface, which becomes more important in PHJ at high illumination densities due to preferred photogeneration at this interface. For intense bias light, electrons (holes) diffuse within the acceptor (donor) layer away from the planar heterointerface. Thus, they are screened from bimolecular recombination, which occurs primarily at the donor–acceptor interface, leading to an enhanced charge carrier lifetime in PHJ devices. The latter can be directly related to the open circuit voltage of the PHJ device exceeding the voltage of the BHJ system under high illumination densities (Fig. 7.2 (b)). Pointing towards the comparison of $n_{ext}$ and $n_{int}$ in Fig. 7.4(b) an almost parallel shift with similar slope $\lambda$ becomes evident. The charge carrier density at the interface $n_{int}$, theoretically calculated by Eq. (7.2) is slightly higher than the experimental parameter $n_{ext}$. The choice of $N_D$, identified from the simulation, comprises the most inaccuracy. Nevertheless, a change of $N_D$ would only lead to a parallel shift of $n_{int}$ in Fig. 7.4(b) without impact on our conclusions. Furthermore, a non-linear dependence of the small perturbation charge carrier lifetime $\tau_{\Delta n}$ on the charge carrier density ($\tau_{\Delta n} \propto n^{-\lambda}$) can be derived from Fig. 7.4(b). Thereby, the slope $\lambda$ represents the charge carrier decay order $\lambda$+1 according to $dn/dt \propto n^{\lambda+1}$, usually found to be higher than two if determined by transient experiments on organic solar cells (see Chapter 6, Fig. 6.1.2). The deviation from a quadratic decay order is commonly explained by the influence of trapped charge carriers [70, 73, 74]. The data depicted in Fig. 7.4(b) shows a significantly steeper slope for the BHJ device than for the PHJ device and both devices exceed the quadratic decay order. This finding clearly reveals the influence of the active layer morphology on charge trapping and suggests a lot more charges being trapped in the complex morphology of a bulk system than in simple PHJ device architecture.

### 7.4.2 Open Circuit Voltage

As mentioned above and depicted in Fig. 7.1 the experimental current–voltage characteristics of BHJ and PHJ devices were fitted by a macroscopic device

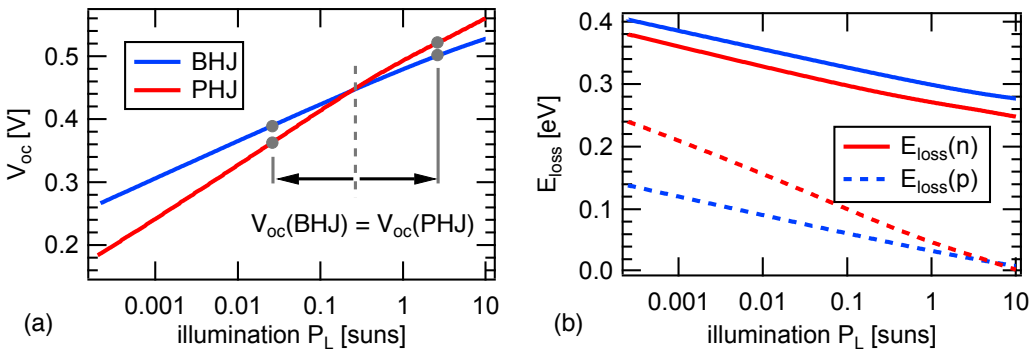


Figure 7.5: (a) Simulated open circuit voltage $V_{oc}$ and (b) calculated loss in potential for PHJ and BHJ devices as a function of illumination intensity. Vertical lines at 10 suns before and after the crossing of $V_{oc}$ mark the intensities at which the charge carrier distributions are shown in Fig. 7.6.

simulation program. For details see the experimental section (7.2) and a summary of the derived fitting parameters in the Appendix (Table B.1). The retrieved parameter set was subsequently used to qualitatively reproduce the experimentally found dependence of $V_{oc}$ on the light intensity $P_L$. The results from the simulation are depicted in Fig. 7.5(a) and perfectly agree with the experiment (Fig. 7.2(b)). In principle, only experimentally determined parameters were used as input for the simulation. As noted in the experimental section, only slight adjustments were necessary to improve the fits to the measured $j/V$ response. Parameters determined by TPV and CE measurements were not used for the simulation, even though experimental and modeled charge carrier concentration and lifetime are qualitatively similar. The main purpose of the simulation was to show that nongeminate recombination, as discussed in the previous section, leads to charge carrier distributions which specifically depend on the respective device architecture. The corresponding loss of electric potential (Fig. 7.5(b)) leads to the experimentally observed differences in the dependence of the open circuit voltage on light intensity for PHJ and BHJ devices.

Mathematically $V_{oc}$ can be described for both device architectures as the effective band gap $E_g$ determined by the lowest unoccupied molecular orbital (LUMO) of $C_{60}$ and the highest occupied molecular orbital (HOMO) of CuPc (cf. Eqn. 7.1), reduced by all potential losses, injection barriers $\Phi$ and Coulomb interaction between charge carriers $E_{loss}$,

$$V_{oc} = \left(E_g - \Phi_n - \Phi_p - E_{loss}\right)/q. \tag{7.3}$$

In accordance with the experimentally found sum of injection barriers, the barrier parameters were set to $\Phi_p = 0.25$ eV (anode) and $\Phi_n = 0.0$ eV (cathode).
In order to find an expression for the loss in potential $E_{loss}$, the drift–diffusion equation for electrons,

$$j_n = qn\mu_n E - qD_n \frac{\partial n}{\partial x} \tag{7.4}$$

and holes respectively

$$j_p = qp\mu_p E + qD_p \frac{\partial p}{\partial x} \tag{7.5}$$

is considered, with the electron and hole mobilities $\mu_n$, $\mu_p$ as well as their related diffusion constants $D_n$, $D_p$ and the electric field over the device $E$. As the net current flow under open circuit condition has to vanish, the sum of the two drift–diffusion equations for electrons and holes can be set to zero and subsequently be written as a function of the electric field. The overall lost electric potential therefore reads

$$E_{loss} = \int_0^L \frac{-D_n \frac{\partial n(x)}{\partial x} + D_p \frac{\partial p(x)}{\partial x}}{\mu_n n\,(x) + \mu_p p\,(x)} \mathrm{d}x, \tag{7.6}$$

with the active layer thickness $L$. From Eq. (7.6), we find high charge carrier density gradients to be responsible for losses of $V_{oc}$, whereas high charge carrier densities generated by illumination lead to an increase of $V_{oc}$. In order to pinpoint the origin of the detailed $V_{oc}$ vs. light intensity dependence, the integral can be separated into two parts for the derivative of electrons and holes, respectively. The results are shown in Fig. 7.5(b). The corresponding charge carrier profiles for BHJ and PHJ devices are presented in Fig. 7.6 for the two light intensities marked in Fig. 7.5(a), as well as for dark conditions.

As described, the BHJ has a higher open circuit voltage at low light intensities, but due to the lesser slope of $V_{oc}$ vs. illumination, as compared to the PHJ, the latter has the higher $V_{oc}$ above 0.3 suns (Fig. 7.2 (b)). The carrier concentration profiles (Fig. 7.6) show a fundamental difference, since holes and electrons are well separated from each other in PHJ solar cells, but reside within an effective medium in the BHJ. Minority charge carriers in the PHJ, i.e., electrons in the p-conducting as well as holes in the n-conducting material possess a charge carrier density of not more than $10^5$ m$^{-3}$. In contrast, a BHJ solar cell shows a high concentration of both types of charge carriers across the whole extent of the device, which leads to a slightly higher overall generation term than in PHJ. A metal electrode generally injects electrons as well as holes into a semiconductor described as thermal activation by the thermionic emission theory. Consequently, the ratio between injected electrons and holes is an exponential function of the offsets between the metal Fermi level and the

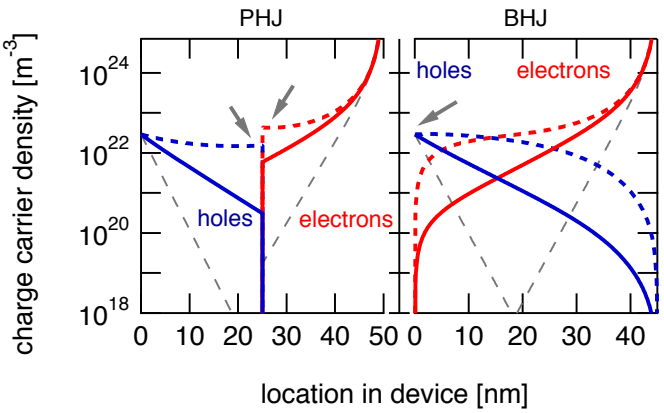


Figure 7.6: Charge carrier density distribution due to photogeneration and injection for a PHJ (left) and a BHJ (right) device at zero (thin dashed), low (solid) and high (dashed) illumination intensity, corresponding to the leftmost and rightmost markers in Fig. 7.5(b). With increasing light intensity charges are accumulated at the heterointerface in contrast to the fixed boundary conditions at the electrodes. At high illumination levels space charge regions marked by grey arrows can be observed.

LUMO and HOMO levels of the semiconductor. An injection barrier as used here refers to the smaller value of both offsets. For the anode, where holes are the majority charge carriers, this can be stated as

$$p \propto \exp(-\Phi_p) \quad \text{and} \quad n \propto \exp(-E_g + \Phi_p). \tag{7.7}$$

Hence, in Fig. 7.6 the rightmost and leftmost charge carrier densities, which means at the electrodes, are constant for all illumination levels. Photogenerated charge carriers are accumulated inside the bulk and especially in proximity of the heterointerface.

BHJ devices are described as effective medium with a band gap $E_g$ of 1.05 eV. For this reason, the injection of majority carriers at the anode corresponds to hole injection into CuPc, whereas the minority carriers at this interface are electrons injected into $C_{60}$. In contrast, in PHJ devices only one of the two photoactive materials is adjacent to a given electrode, e.g. CuPc (anode). Thus, while the majority (hole) injection barrier corresponds to the BHJ case, the minority carriers have a larger injection barrier equal to the CuPc gap less $\Phi_p$, which leads to a lower concentration of minority charge carriers. The situation at the cathode is equivalent, considering that electrons are majorities there. Consequently, the higher a certain injection barrier is, the lower the difference between injected majority and minority charge carriers.

The charge carrier profiles of the BHJ and the PHJ device (Fig. 7.6), can be

interpreted in terms of Eq. (7.6). In PHJ devices, the type of majority charge carrier changes always at the heterointerface. In contrast, charge carriers in the BHJ are not restricted to specific layers. Therefore, the spatial position at which the type of majority charge carriers changes from electrons to holes is not constant. Accordingly, the charge carrier densities and especially their sums are always higher in a BHJ than in a PHJ device. The smaller $V_{oc}$ of the PHJ device in particular at low illumination levels, however, is also caused by the additional steep gradient of the charge carrier concentration. With increasing light intensity, the photogenerated charge at the donor–acceptor interface of PHJ devices has a major impact on the charge carrier gradient within the organic layers. For low light intensities, this gradient leads to charge diffusion towards the interface, while at higher light intensities the gradient can change direction. This is in accordance with longer charge carrier lifetimes derived experimentally by TPV for the planar device (see Fig. 7.4(b)) as charges diffusing away from the interface are screened from nongeminate recombination. In terms of $V_{oc}$ this weaker gradient reduces the loss in electric potential (Fig. 7.5(a)) and leads to an open circuit voltage exceeding the one of the BHJ device at intensities above 0.3 suns (Fig. 7.5(b)). Above one sun, space charges (Fig. 7.6, arrows) start piling up in both device architectures.

In the PHJ device, the space charge is built up at the CuPc/$C_{60}$ interface due to the localized photogeneration, introducing a diffusion of charge carriers away from the heterointerface equivalent with the experimentally found enhanced charge carrier lifetime. For this device geometry, $V_{oc}$ is independent of the injection barriers [146]. In BHJ solar cells, however, the space charge region forms at the anode with its small injection barrier, further lowering the open circuit voltage and potentially also the current into this electrode.

## 7.5 Conclusion

The recombination mechanisms of planar and bulk heterojunction solar cells were studied. To this end, transient photovoltage and charge extraction techniques were applied to devices based on CuPc and $C_{60}$. The observed difference in the light intensity dependence of the open circuit voltage between both architectures can be explained by the decay dynamics of charge carriers, as well as their spatial distribution. In bilayer devices, the charge generation primarily occurs at the planar heterojunction, and the photogenerated majority charges are transported in layers with low densities of minority carriers. This induces an enhanced charge carrier lifetime, and carrier profiles that ultimately lead to diffusion away from the heterojunction. In BHJ, however, the complex intermixing of donor and acceptor phase introduces an increased

charge carrier recombination. The $V_{oc}$ values for BHJ are higher compared to PHJ at low light intensities. The smaller slope of $V_{oc}(P_L)$ of the former leads to a cross-section, so that at higher light intensities the open circuit voltage of the BHJ remains below the PHJ device. This effect is due to higher recombination rates in BHJ devices as well as the exclusive impact of the injection barrier on the BHJ solar cells. The experimental findings, in particular the $V_{oc}$ dependence on light intensity, were reproduced by a macroscopic device simulation. Thus, this chapter revealed the impact of the actual charge carrier distribution and charge carrier recombination—both affected by the device architecture—on the open circuit voltage.

Chapter 8

# Conclusion

## Conclusion

The main focus of this work was to elucidate the performance limitations of the emerging organic photovoltaic (OPV) technology on the basis of representive devices. The key experimental techniques were transient photovoltage (TPV) and charge extraction (CE) which provide access to the lifetime and the density of photogenerated charge carriers in organic solar cells under operating conditions. In contrast to other techniques used to study charge carrier dynamics, for instance charge extraction by linear increasing voltage (CE-LIV), TPV experiments are realized by a small optical perturbation and thus under quasi-equilibrium conditions. Other techniques in use were transient photocurrent (TPC) and time delayed collection field (TDCF) to study the charge carrier density and the charge photogeneration, respectively. Besides the standard reference system of OPV, poly(3-hexylthiophene):[6,6]-phenyl-$C_{61}$butyric acid methyl ester (P3HT:$PC_{61}$BM), the low-band gap polymer PTB7 in combination with [6,6]-phenyl-$C_{71}$butyric acid methyl ester and evaporated samples based on the small molecules CuPc and $C_{60}$ were investigated intensively.

By an extensive TPV/TPC study it was feasible to analyze the standard OPV reference system, P3HT:$PC_{61}$BM, with the Shockley Equation (SE). It was shown that the SE parameters, i.e., the ideality factor and the dark saturation current, are directly related to charge carrier recombination and are accessible by transient studies on photovoltage and photocurrent in case of field-independent charge carrier generation. The good agreement of static and transient approaches over a wide temperature range demonstrated the validity of the Shockley model for organic solar cells based on material systems satisfying the requirement of field-independent polaron-pair dissociation. Furthermore, the temperature dependence of the dark saturation current $j_0$ allowed determining the effective band gap of the photoactive blend, perfectly agreeing with the literature values of the energy onset of the photocurrent due to charge transfer state absorption. In addition a consisting model was presented, directly relating the ideality factor to recombination of free with trapped charge carriers in an exponential density of states.

On closer consideration of the work above, as-prepared (pristine) and thermally treated (annealed) P3HT:$PC_{61}BM$ solar cells were analyzed by TPV and voltage dependent CE experiments from room temperature to $T = 200K$. The determined charge carrier decay rate under open circuit voltage conditions and the voltage dependent charge carrier densities $n(V)$ enabled to calculate the nongeminate loss current $j_{loss}$. It was shown that $j_{loss}$ alone is sufficient to reconstruct the measured $j/V$ characteristics across the whole operational range for annealed and pristine solar cells and different temperatures. From the perfect agreement of measured and reconstructed data a voltage independent charge photogeneration can be deduced for this material composition and the studied temperature range.

Subsequently, the $j/V$ reconstruction procedure was also applied to the rather new low-band gap polymer PTB7 in combination with $PC_{71}BM$. The devices were processed from pure chlorobenzene and a subset was optimized with 1,8-diiodooctane (DIO) as co-solvent. The dramatic changes in device performance were discussed with respect to the dominating loss processes. While in the devices processed from CB solution, severe geminate and nongeminate recombination were observed, the use of DIO facilitates efficient polaron pair dissociation and minimizes geminate recombination. This was verified by TDCF measurements. The nongeminate loss current $j_{loss}$ of the samples with DIO alone enabled $j/V$ reconstruction while geminate and nongeminate losses were considered to describe the $j/V$ response of samples prepared without additive. The clear performance overestimation by reconstruction for the latter device was attributed to trapped charges in isolated domains of pure fullerene phases.

Finally, nongeminate recombination in devices based on CuPc and $C_{60}$ was addressed. To this end, two device architectures—the planar heterojunction (PHJ) and the bulk heterojunction (BHJ)—were directly compared in view of differences in charge carrier decay dynamics. TPV and CE experiments provided the charge carrier lifetime and density. The observed difference in the light intensity dependence of the open circuit voltage between both architectures was explained by the decay dynamics of charge carriers as well as their spatial distribution.

In PHJ solar cells, the charge generation primarily occurs at the planar heterojunction, and the photogenerated majority charges are transported in layers with low densities of minority carriers. This induces an enhanced charge carrier lifetime, and carrier profiles that ultimately lead to diffusion away from the heterojunction. As from extraction techniques only the spatially averaged carrier concentration can be determined, the charge carrier density at the interface $n_{int}$ was derived from the open circuit voltage.

In BHJ devices, however, the complex intermixing of donor and acceptor

phase introduces an increased charge carrier recombination. The $V_{oc}$ values for BHJ are higher compared to PHJ at low light intensities. The smaller slope of $V_{oc}(P_L)$ for the BHJ leads to a cross-section, so that at higher light intensities the open circuit voltage of the BHJ remains below the PHJ device. This effect is due to higher recombination rates in BHJ devices as well as the exclusive impact of the injection barrier on the BHJ solar cells. We reproduced the experimental findings, in particular the $V_{oc}$ dependence on light intensity, by a macroscopic device simulation. Thus, the impact of the actual charge carrier distribution and charge carrier recombination—both affected by the device architecture—on the open circuit voltage was identified.

In summary this work revealed the detailed impact and peculiarities of charge carrier losses (recombination) on the performance of different types of organic solar cells. By focusing on the $j/V$ characteristics the influence of the active layer morphology on geminate and nongeminate recombination was highlighted. While nongeminate losses mainly effect $V_{oc}$ and can not be neglected in any of the devices studied, geminate losses limit the photogeneration and the fill factor and are strongly related to the morphology of the investigated material compositions. Consequently, one can realize an optimum exploitation of performance potential of a given active material by controlling its morphology. Nevertheless, to achieve the market launch of OPV in near future, further progress from physical and chemical point of view is essential. This definitely will include the synthesis of new, stable, high-performance semiconducting polymers as well as subsequently optimized device processing parameters.

# Zusammenfassung

Das Hauptaugenmerk dieser Arbeit lag in der Untersuchung der Leistungslimitierung der aufstrebenden Technologie organischer Photovoltaik anhand von ausgewählten Beispielen. Schlüsselexperimente waren dabei die Methoden der transienten Photospannung (TPV) und der Ladungsextraktion (CE), welche einen Zugang zur Lebenszeit und Dichte photogenerierter Ladungen unter Arbeitsbedingungen der Zelle ermöglichen. Im Gegensatz zu anderen Techniken zur Untersuchung von Ladungsträgerdynamiken, wie z. B. der *charge extraction by linear increasing voltage* (CELIV) Methode, werden TPV Experimente durch eine kleine optische Störung und damit unter Quasi-Gleichgewichtsbedingungen realisiert. Neben dem Standardreferenzsystem der OPV, poly(3-hexylthiophene):[6,6]-phenyl-$C_{61}$butyric acid methyl ester (P3HT:$PC_{61}$BM) wurden das *low-bandgap* Polymer PTB7 in Kombination mit [6,6]-phenyl-$C_{71}$butyric acid methyl ester ($PC_{71}$BM) sowie aufgedampfte Proben basierend auf CuPc und $C_{60}$ intensiv untersucht.

In einer umfangreichen Studie stützend auf TPV/TPC Messungen war es möglich das Standardreferenzsystem der OPV, P3HT:$PC_{61}$BM mit der Shockley Gleichung (SE) zu untersuchen. Es wurde gezeigt, dass die Shockley Parameter, sprich der Idealitätsfaktor und der Dunkelsättigungsstrom, direkt mit der Rekombination von Ladungen zusammenhängen und durch transiente Messungen der Photospannung bzw. des Photostroms zugänglich sind, sofern eine feldunabhängige Ladungsgeneration vorliegt. Die gute Übereinstimmung von statischem und transientem Ansatz über einen großen Temperaturbereich verdeutlicht die Gültigkeit des Shockley Models für organische Solarzellen basierend auf Materialsystemen mit feldunabhängiger Polaronenpaartrennung. Des Weiteren ermöglichte die Temperaturabhängigkeit des Dunkelsättigungsstroms $j_0$ die Bestimmung der effektiven Bandlücke des photoaktiven Materials. Es zeigt sich eine perfekte Übereinstimmung mit den Literaturwerten, berechnet aus dem Einsetzen des Photostroms bei Absorption über den Ladungstransferzustand. Zudem wurde ein in sich konsistentes Model dargelegt, welches den Idealitätsfaktor direkt mit der Rekombination freier und gefangener Ladungen, verteilt in einer exponentiell abfallenden Zustandsdichte, verknüpft.

In einer noch detaillierteren Studie wurden unbehandelte (pristine) und thermisch geheizte (annealed) P3HT:$PC_{61}$BM Zellen mittels TPV und spannungsabhängigen Ladungsextraktionsmessungen, über einen Temperaturbereich von Raumtemperatur bis $T = 200K$, untersucht. Der so ermittelte Ladungsträgerzerfall unter Leerlaufbedingungen und die spannungsabhängigen Ladungsträgerdichten $n(V)$ ermöglichten die Berechnung eines nichtgeminalen Verluststroms $j_{loss}$. Es wurde gezeigt, dass, über den kompletten

Temperaturbereich, die gemessene $j/V$ Kurve im 4. Quadranten, sowohl der unbehandelten als auch der geheizten Probe, einzig mittels des experimentell bestimmten Verluststroms $j_{loss}$ komplett nachgebildet werden kann. Durch die perfekte Übereinstimmung von gemessenen und nachgebildeten $j/V$ Daten kann eine spannungsunabhänige Photogeneration für dieses Materialsystem und den untersuchten Temperaturbereich abgeleitet werden.

Anschließend wurde die Vorgehensweise der $j/V$ Rekonstruktion auf das neuartige *low-band gap* Polymer PTB7, in Verbindung mit $PC_{71}BM$ angewandt. Die Zellen wurden aus einer Chlorbenzol(CB)-Lösung hergestellt, während eine Teilmenge mittels des Zusatzes 1,8-diiodooktan (DIO) optimiert wurde. Die daraus resultierende dramatische Leistungsverbesserung wurde im Bezug auf die dominierenden Verlustmechanismen erörtert. Während beachtliche geminale wie nichtgeminale Verluste in Proben hergestellt aus reiner CB-Lösung zu beobachten waren, erleichtert die Zugabe von DIO die effiziente Trennung von Polaronenpaaren und minimiert geminale Verluste. Dies konnte mittels TDCF Messungen bestätigt werden. Alleinig der nichtgeminale Verluststrom $j_{loss}$ von Proben hergestellt mit DIO als Zusatz ermöglicht eine $j/V$ Nachbildung, während eine $j/V$ Rekonstruktion der Zellen ohne DIO die Berücksichtigung geminaler und nichtgeminaler Verluste verlangt. Die deutlich sichtbare Überschätzung der gemessenen Kurve durch die $j/V$ Rekonstruktion der Probe ohne DIO wurde mit gefangenen Ladungen in abgeschlossenen Domänen in Verbindung gebracht.

Letztlich wurde die nichtgeminale Rekombination in Proben basierend auf CuPc und $C_{60}$ untersucht. Zu diesem Zweck wurden zwei unterschiedliche Proben Architekturen, die planare (PHJ) und die Mischübergangsstruktur (BHJ), direkt im Bezug auf Unterschiede in der Ladungsträgerdynamik miteinander verglichen. TPV und CE Experimente liefern Lebenszeit und Dichte der Ladungsträger. Die gemessenen Unterschiede zwischen beiden Architekturen in der Lichtabhängigkeit der Leerlaufspannung konnte anahnd der Zerfallsdynamik der Ladungsträger sowie deren räumlicher Verteilung veranschaulicht werden.
In der planaren Struktur findet die Generation von Ladung vorzugsweise am planaren Heteroübergang statt und die photogenerierten Majoritätsladungsträger werden in einer Schicht mit einer geringen Dichte an Minoritätsladungsträgern transportiert. Dies bewirkt eine Verlängerung der Lebenszeit und ein Ladungsträgerprofil, welches zu einer Diffusion weg vom Heteroübergang führt. Da mittels Exktraktionsmethoden nur räumlich gemittelte Konzentrationen bestimmt werden können, wurde die Dichte an Ladungen um die hetero Grenzschicht $n_{int}$ über deren Zusammenhang mit der Leerlaufspannung bestimmt.
In Mischübergangszellen hingegen führt das komplexe Netz aus Donator und

Akzeptor zu einer erhöhten Rekombination. Die $V_{oc}$-Werte der BHJ Zelle sind höher als die der PHJ bei niedrigen Lichtleistungen. Die kleinere Steigung von $V_{oc}(P_L)$ der BHJ führt zu einem Schnittpunkt, so dass bei höheren Lichtintensitäten die Leerlaufspannung der BHJ unterhalb der PHJ bleibt. Dieser Effekt beruht auf höherer Rekombination in der Mischübergangssolarzelle sowie dem ausschließlichen Einfluss von Injektionsbarrieren auf diese. Die experimentellen Beobachtungen, im speziellen die $V_{oc}$-Abhängigkeit von der Lichtleistung, konnten mit Hilfe von makroskopischen Simulationen überprüft werden. Somit wurden in dieser Studie der Einfluss der effektiven Ladungsträgerdichteverteilung und der Rekombination, welche beide von der Architektur der Probe beeinflusst werden, auf die Leerlaufspannung offengelegt.

Alles in allem verdeutlicht diese Arbeit die Auswirkungen von Ladungsträgerverlusten (Rekombination) auf die Leistung verschiedener organischer Solarzellen. Durch gezieltes Untersuchen der $j/V$ Kennlinie stand der Einfluss der Morphologie der aktiven Schicht auf geminale und nichtgeminale Verluste im Vordergrund. Während nichtgeminale Verluste vorwiegend $V_{oc}$ beeinflussen und in keiner der untersuchten Proben vernachlässigt werden konnte, limitieren geminale Verluste die Photogeneration und den Füllfaktor und sind stark von der Morphologie der hier betrachteten Materialien abhängig. Folglich erreicht man das Optimum der Leistung eines gegebenen Materialsystems am besten anhand der Einflussnahme auf die Morphologie. Dennoch, um eine Vermarktung von OPV in naher Zukunft zu realisieren, ist ein Fortschritt auf physikalischer und chemischer Seite unerlässlich. Dies umfasst die Synthese neuer, stabiler, hocheffizienter, halbleitender Polymere genauso wie eine darauf folgende Optimierung der Herstellungsparameter.

# Bibliography


[1] Europäische Union. Energie 2020. Technical report, 2011.

[2] Photon. Das Solarstrom-Magazin. page 112, December 2012.

[3] Photon. Das Solarstrom-Magazin. page 52, April 2012.

[4] VDI. Nachrichten, December 2012.

[5] A. E. Becquerel. Mémoire sur les effets électriques produits sous l'influence des rayons solaires. *Comt. Rend. Acad. Sci.*, 9:561, 1839.

[6] D. M. Chapin, C. S. Fuller, and G. L. Pearson. A New Silicon p-n Junction Photocell for Converting Solar Radiation into Electrical Power. *Journal of Applied Physics*, 25(5):676, 1954.

[7] W. Shockley and H. Queisser. Detailed Balance Limit of Efficiency of p-n Junction Solar Cells. *Journal of Applied Physics*, 32(3):510, 1961.

[8] M. Green, K. Emery, Y. Hishikawa, W. Warta, and E. Dunlop. Solar cell efficiency tables (version 41). *Progress in Photovoltaics: Research and Applications*, 21(1), 2013.

[9] R. Gaudiana. Third-Generation Photovoltaic Technology - The Potential for Low-Cost Solar Energy Conversion. *The Journal of Physical Chemistry Letters*, 1(7):1288–1289, April 2010.

[10] C. Brabec, J. Hauch, P. Schilinsky, and C. Waldauf. Production Aspects of Organic Photovoltaics and Commercialization of Devices. 30(January), 2005.

[11] A. Huebler, B. Trnovec, T. Zillger, M. Ali, N. Wetzold, M. Mingebach, A. Wagenpfahl, C. Deibel, and V. Dyakonov. Printed Paper Photovoltaic Cells. *Advanced Energy Materials*, 1(6):1018–1022, 2011.

[12] V. Shrotriya. Organic photovoltaics: Polymer power. *Nature Photonics*, 3(8):447–449, August 2009.

[13] R. García-Valverde, J. Cherni, and A. Urbina. Life cycle analysis of organic photovoltaic technologies. *Progress in Photovoltaics: Research and Applications*, 18(7):535–558, 2010.

[14] G. Li, R. Zhu, and Y. Yang. Polymer solar cells. *Nature Photonics*, 6(3):153–161, 2012.

[15] C. Brabec and J. R. Durrant. Solution-Processed Organic Solar Cells. 33(July), 2008.

[16] M. Jorgensen, K. Norrman, S. Gevorgyan, T. Tromholt, B. Andreasen, and F. Krebs. Stability of polymer solar cells. *Advanced materials*, 24(5):580–612, 2012.

[17] M. Volmer. Die verschiedenen lichtelektrischen Erscheinungen am Anthracen, ihre Beziehungen zueinander, zur Fluoreszenz und Dianthracenbildung. *Annalen der Physik*, 345(4):775–796, 1913.

[18] W. Helfrich and W. Schneider. Recombination Radiation in Anthracene Crystals. *Physical Review Letters*, 14(7):229–231, 1965.

[19] M. Pope and C. E. Swenberg. *Electronic Processes in Organic Crystals and Polymers*, volume 51. Oxford University Press, USA, 2nd editio edition, 1999.

[20] W. Brütting. *Physics of Organic Semiconductors*. WILEY-VCH, 2005.

[21] H. Shirakawa, E. Louis, A. MacDiarmid, C. Chiang, and A. J. Heeger. Synthesis of electrically conducting organic polymers: halogen derivatives of polyacetylene, (CH) x. *Journal of the Chemical Society, Chemical Communications*, (16):578, 1977.

[22] C. Chiang, C. Fincher, Y. Park, A. Heeger, H. Shirakawa, E. Louis, S. Gau, and A. MacDiarmid. Electrical Conductivity in Doped Polyacetylene. *Physical Review Letters*, 39(17):1098–1101, 1977.

[23] C. W. Tang. Two-layer organic photovoltaic cell. *Applied Physics Letters*, 48(2):183–186, 1986.

[24] N. Sariciftci, L. Smilowitz, A. J. Heeger, and F. Wudl. Photoinduced electron transfer from a conducting polymer to buckminsterfullerene. *Science*, 258(5087):1474–1476, 1992.

[25] G. Yu, J. Gao, J. C. Hummelen, F. Wudl, and a. J. Heeger. Polymer Photovoltaic Cells: Enhanced Efficiencies via a Network of Internal Donor-Acceptor Heterojunctions. *Science*, 270(5243):1789–1791, December 1995.

[26] A. M. Ballantyne, T. Ferenczi, M. Campoy-Quiles, T. M. Clarke, A. Maurano, K. H. Wong, W. Zhang, N. Stingelin-Stutzmann, J. Kim, D. Bradley, J. R. Durrant, I. McCulloch, M. Heeney, J. Nelson, S. Tierney, W. Duffy, C. Mueller, and P. Smith. Understanding the Influence of Morphology on Poly(3-hexylselenothiophene):PCBM Solar Cells. *Macromolecules*, 43(3):1169–1174, 2010.

[27] P.G. Karagiannidis, S. Kassavetis, C. Pitsalidis, and S. Logothetidis. Thermal annealing effect on the nanomechanical properties and structure of P3HT:PCBM thin films. *Thin Solid Films*, 519(12):4105–4109, 2011.

[28] X. Liu, S. Huettner, Z. Rong, M. Sommer, and R. H. Friend. Solvent additive control of morphology and crystallization in semiconducting polymer blends. *Advanced Materials*, 24(5):669–74, 2012.

[29] R. E. Peierls. *Quantum Theory of Solids*. Oxford University Press, 1955.

[30] S. Schaur. *Electrochemical doping of organic field-effect transistors to improve contact resistances*. Master thesis, Linz, 2010.

[31] C. Arndt. *Untersuchung von angeregten Zuständen in Bulk-Heterojunction Polymer/Fulleren-Solarzellen*. Master thesis, Ilmenau, 2003.

[32] M. Mingebach. *Photocurrent in Organic Solar Cells*. PhD thesis, Würzburg, 2012.

[33] B. Kippelen and J.-L. Brédas. Organic photovoltaics. *Energy & Environmental Science*, 2(3):251–261, 2009.

[34] C. Deibel, D. Mack, J. Gorenflot, D. Rauh, and V. Dyakonov. Energetics of excited states in the conjugated polymer poly(3-hexylthiophene). *Physical Review B*, 81(8):85202, 2010.

[35] I. Scheblykin, A. Yartsev, T. Pullerits, V. Gulbinas, and V. Sundström. Excited state and charge photogeneration dynamics in conjugated polymers. *The Journal of Physical Chemistry B*, 111(23):6303–6321, 2007.

[36] P. Shaw, A. Ruseckas, and I. Samuel. Exciton Diffusion Measurements in poly(3-hexylthiophene). *Advanced Materials*, 20(18):3516–3520, 2008.

[37] T. Stuebinger and W. Bruetting. Exciton diffusion and optical interference in organic donor-acceptor photovoltaic cells. *Journal of Applied Physics*, 90(7):3632–3642, 2001.

[38] I. Hwang, D. Moses, and A. Heeger. Photoinduced Carrier Generation in P3HT / PCBM Bulk Heterojunction Materials. *Journal of Physical Chemistry C*, 17:4350–4354, 2008.

[39] L. Onsager. Initial Recombination of Ions. *Physical Review*, 54:555, 1938.

[40] C. L. Braun. Electric field assisted dissociation of charge transfer states as a mechanism of photocarrier production. *Journal of Chemical Physics*, 80:4157–4161, 1984.

[41] C. Deibel and V. Dyakonov. Polymer-fullerene bulk heterojunction solar cells. *Reports on Progress in Physics*, 73(9):096401, 2010.

[42] L. Koster, E. Smits, V. Mihailetchi, and P. Blom. Device model for the operation of polymer/fullerene bulk heterojunction solar cells. *Physical Review B*, 72(8):85205, 2005.

[43] C. Deibel, A. Wagenpfahl, and V. Dyakonov. Influence of charge carrier mobility on the performance of organic solar cells. *physica status solidi (RRL) - Rapid Research Letters*, 2(4):175–177, 2008.

[44] V. Mihailetchi, L. Koster, J. Hummelen, and P. Blom. Photocurrent Generation in Polymer-Fullerene Bulk Heterojunctions. *Physical Review Letters*, 93(21):216601, November 2004.

[45] R. Hoofman, M. Haas, L. Siebbeles, and J. Warman. Highly mobile electrons and holes on isolated chains of the semiconducting polymer poly(phenylene vinylene). *Letters to nature*, 392:54–56, 1998.

[46] T. Savenije, J. Kroeze, X. Yang, and J. Loos. The formation of crystalline P3HT fibrils upon annealing of a PCBM:P3HT bulk heterojunction. *Thin Solid Films*, 511-512:2–6, 2006.

[47] C. Deibel, T. Strobel, and V. Dyakonov. Origin of the Efficient Polaron-Pair Dissociation in Polymer-Fullerene Blends. *Physical Review Letters*, 103(3):036402, 2009.

[48] A. Petersen, A. Ojala, T. Kirchartz, T. Wagner, F. Würthner, and U. Rau. Field-dependent exciton dissociation in organic heterojunction solar cells. *Physical Review B*, 85(24):245208, 2012.

[49] R. Street, S. Cowan, and A. Heeger. Experimental test for geminate recombination applied to organic solar cells. *Physical Review B*, 82(12):11–13, 2010.

[50] J. Kniepert, M. Schubert, J. Blakesley, and D. Neher. Photogeneration and Recombination in P3HT/PCBM Solar Cells Probed by Time-Delayed Collection Field Experiments. *The Journal of Physical Chemistry Letters*, 2(7):700–705, 2011.

[51] M. Mingebach, S. Walter, V. Dyakonov, and C. Deibel. Direct and charge transfer state mediated photogeneration in polymer-fullerene bulk heterojunction solar cells. *Applied Physics Letters*, 100(19):193302, 2012.

[52] H. Ohkita, S. Cook, Y. Astuti, W. Duffy, S. Tierney, W. Zhang, M. Heeney, I. McCulloch, J. Nelson, D. Bradley, and J. R. Durrant. Charge carrier formation in polythiophene/fullerene blend films studied by transient absorption spectroscopy. *Journal of the American Chemical Society*, 130(10):3030–3042, 2008.

[53] S. Shoaee, T. Clarke, C. Huang, S. Barlow, S. Marder, M. Heeney, I. McCulloch, and J. R. Durrant. Acceptor energy level control of charge photogeneration in organic donor/acceptor blends. *Journal of the American Chemical Society*, 132(37):12919–12926, 2010.

[54] A. Miller and E. Abrahams. Impurity Conduction at Low Concentrations. *Physical Review*, 120(3):745–755, November 1960.

[55] H. Bässler. Charge Transport in Disordered Organic Photoconductors a Monte Carlo Simulation Study. *physica status solidi (b)*, 175(1):15–56, 1993.

[56] F. Schmidlin. Theory of trap-controlled transient photoconduction. *Physical Review B*, 16(6):2362–2385, 1977.

[57] H. Bässler and A. Köhler. Charge transport in organic semiconductors. *Topics in current chemistry*, 312:1–65, 2012.

[58] S. Baranovskii. *Charge Transport in Disordered Solids*. Wiley, 2006.

[59] A. Wagenpfahl, D. Rauh, M. Binder, C. Deibel, and V. Dyakonov. S-shaped current-voltage characteristics of organic solar devices. *Physical Review B*, 82(11):115306, 2010.

[60] A. Wagenpfahl. *Numerical simulations on limitations and optimization strategies of organic solar cells*. PhD thesis, Würzburg, 2013.

[61] T. Strobel, C. Deibel, and V. Dyakonov. Role of Polaron Pair Diffusion and Surface Losses in Organic Semiconductor Devices. *Physical Review Letters*, 105(26):266602, 2010.

[62] G. Dennler, M. Scharber, and C. Brabec. Polymer-Fullerene Bulk-Heterojunction Solar Cells. *Advanced Materials*, 21(13):1323–1338, 2009.

[63] C. Deibel, V. Dyakonov, and C. J. Brabec. Organic Bulk-Heterojunction Solar Cells. *IEEE Journal of Selected Topics in Quantum Electronics*, 16(6):1517–1527, 2010.

[64] V. Shrotriya, G. Li, Y. Yao, T. Moriarty, K. Emery, and Y. Yang. Accurate Measurement and Characterization of Organic Solar Cells. *Advanced Functional Materials*, 16(15):2016–2023, 2006.

[65] I. Howard, R. Mauer, M. Meister, and F. Laquai. Effect of morphology on ultrafast free carrier generation in polythiophene:fullerene organic solar cells. *Journal of the American Chemical Society*, 132(42):14866–14876, 2010.

[66] F. Etzold, I. Howard, R. Mauer, M. Meister, T.-D. Kim, K.-S. Lee, N. S. Baek, and F. Laquai. Ultrafast exciton dissociation followed by nongeminate charge recombination in PCDTBT:PCBM photovoltaic blends. *Journal of the American Chemical Society*, 133(24):9469–9479, 2011.

[67] J. Kern, S. Schwab, C. Deibel, and V. Dyakonov. Binding energy of singlet excitons and charge transfer complexes in MDMO-PPV:PCBM solar cells. *physica status solidi (RRL) - Rapid Research Letters*, 5(10-11):364–366, 2011.

[68] P. Langevin. Recombinaison et mobilites des ions dans les gaz. *Ann. Chim. Phys.*, 28:433, 1903.

[69] C. Deibel, A. Baumann, and V. Dyakonov. Polaron recombination in pristine and annealed bulk heterojunction solar cells. *Applied Physics Letters*, 93(16):163303, 2008.

[70] C. G. Shuttle, B. O'Regan, A. M. Ballantyne, J. Nelson, D. D. C. Bradley, J. de Mello, and J. R. Durrant. Experimental determination of the rate law for charge carrier decay in a polythiophene:fullerene solar cell. *Applied Physics Letters*, 92(9):093311, 2008.

[71] C. Deibel and A. Wagenpfahl. Comment on Interface state recombination in organic solar cells. *Physical Review B*, 82(20):207301, 2010.

[72] T. Kirchartz, B. Pieters, J. Kirkpatrick, U. Rau, and J. Nelson. Recombination via tail states in polythiophene:fullerene solar cells. *Physical Review B*, 83(11):115209, 2011.

[73] A. Foertig, A. Baumann, D. Rauh, V. Dyakonov, and C. Deibel. Charge carrier concentration and temperature dependent recombination in polymer-fullerene solar cells. *Applied Physics Letters*, 95(5):052104, 2009.

[74] A. Baumann, T. J. Savenije, D. H. K. Murthy, M. Heeney, V. Dyakonov, and C. Deibel. Influence of Phase Segregation on Recombination Dynamics in Organic Bulk-Heterojunction Solar Cells. *Advanced Functional Materials*, 21(9):1687–1692, 2011.

[75] C. G. Shuttle, R. Hamilton, B. C. O'Regan, J. Nelson, and J. R. Durrant. Charge-density-based analysis of the current-voltage response of polythiophene/fullerene photovoltaic devices. *Proceedings of the National Academy of Sciences of the United States of America*, 107(38):16448, 2010.

[76] A. Maurano, C. G. Shuttle, R. Hamilton, A. M. Ballantyne, J. Nelson, W. Zhang, M. Heeney, and J. R. Durrant. Transient Optoelectronic Analysis of Charge Carrier Losses in a Selenophene/Fullerene Blend Solar Cell. *The Journal of Physical Chemistry C*, 115(13):5947–5957, 2011.

[77] C. Deibel, A. Wagenpfahl, and V. Dyakonov. Origin of reduced polaron recombination in organic semiconductor devices. *Physical Review B*, 80(7):75203, 2009.

[78] A. Mozer, N. Sariciftci, A. Pivrikas, R. Österbacka, G. Juška, L. Brassat, and H. Bässler. Charge carrier mobility in regioregular poly(3-hexylthiophene) probed by transient conductivity techniques: A comparative study. *Physical Review B*, 71(3):035214, 2005.

[79] G. Juska, K. Arlauskas, M. Viliunas, and J. Kocka. Extraction current transients: new method of study of charge transport in microcrystalline silicon. *Physical review letters*, 84(21):4946–4949, 2000.

[80] G. Juška, K. Genevičius, K. Arlauskas, R. Österbacka, and H. Stubb. Charge transport at low electric fields in $\pi$-conjugated polymers. *Physical Review B*, 65(23):233208, 2002.

[81] C. G. Shuttle. *Recombination dynamics in polythiophene:fullerene solar cells*. PhD thesis, London, 2008.

[82] C. G. Shuttle, A. Maurano, R. Hamilton, B. O'Regan, J. C. de Mello, and J. R. Durrant. Charge extraction analysis of charge carrier densities

in a polythiophene/fullerene solar cell: Analysis of the origin of the device dark current. *Applied Physics Letters*, 93(18):183501, 2008.

[83] J. Mort, I Chen, A Troup, M Morgan, J. Knights, and R. Lujan. Nongeminate Recombination of a-Si: H. *Physical Review Letters*, 45(16):1348, 1980.

[84] T. Offermans, S. Meskers, and R. J. Janssen. Time delayed collection field experiments on polymer: Fullerene bulk-heterojunction solar cells. *Journal of Applied Physics*, 100(7):074509, 2006.

[85] U. Zhokhavets, T. Erb, H. Hoppe, G. Gobsch, and N.S. Sariciftci. Effect of annealing of poly(3-hexylthiophene)/fullerene bulk heterojunction composites on structural and optical properties. *Thin Solid Films*, 496(2):679, 2006.

[86] C. R. McNeill, J. J. M. Halls, R. Wilson, G. L. Whiting, S. Berkebile, M. G. Ramsey, R. H. Friend, and N. C. Greenham. Efficient Polythiophene/Polyfluorene Copolymer Bulk Heterojunction Photovoltaic Devices: Device Physics and Annealing Effects. *Advanced Functional Materials*, 18(16):2309, 2008.

[87] F. Padinger, R.S. Rittberger, and N.S. Sariciftci. Effects of Postproduction Treatment on Plastic Solar Cells. *Advanced Functional Materials*, 13(1):85–88, 2003.

[88] Y. Liang, Z. Xu, J. Xia, S. Tsai, Y. Wu, G. Li, C. Ray, and L. Yu. For the bright future-bulk heterojunction polymer solar cells with power conversion efficiency of 7.4%. *Advanced Materials*, 22(20):135–138, 2010.

[89] M. R. Hammond, R. J. Kline, A. Herzing, L. J. Richter, D. S Germack, H. Ro, C. L. Soles, D. Fischer, T. Xu, L. Yu, M. F. Toney, and D. M. Delongchamp. Molecular order in high-efficiency polymer/fullerene bulk heterojunction solar cells. *ACS Nano*, 5(10):8248–8257, 2011.

[90] J. W. Arbogast and C. S. Foote. Photophysical properties of C70. *Journal of the American Chemical Society*, 113(23):8886–8889, 1991.

[91] M. M. Wienk, J. M Kroon, W. J. H. Verhees, J. Knol, J.C. Hummelen, P. van Hal, and R. J. Janssen. Efficient methano[70]fullerene/MDMO-PPV bulk heterojunction photovoltaic cells. *Angewandte Chemie*, 42(29):3371–3375, 2003.

[92] A. Maurano, R. Hamilton, C. G. Shuttle, A. M. Ballantyne, J. Nelson, B. O'Regan, W. Zhang, I. McCulloch, H. Azimi, M. Morana, C. J. Brabec, and J. R. Durrant. Recombination dynamics as a key determinant of open circuit voltage in organic bulk heterojunction solar cells: a comparison of four different donor polymers. *Advanced Materials*, 22(44):4987–4992, 2010.

[93] S. M. Sze and Kwok K. Ng. *Physics of semiconductor devices*. Wiley-Blackwell, New York, 2007.

[94] D. Chirvase, Z. Chiguvare, M. Knipper, J. Parisi, V. Dyakonov, and J. C. Hummelen. Temperature dependent characteristics of poly(3 hexylthiophene)-fullerene based heterojunction organic solar cells. *Journal of Applied Physics*, 93(6):3376, 2003.

[95] K. Vandewal, K. Tvingstedt, A. Gadisa, O. Inganäs, and J. Manca. On the origin of the open-circuit voltage of polymer-fullerene solar cells. *Nature Materials*, 8(11):904–909, 2009.

[96] L. J. A. Koster, V. D. Mihailetchi, R. Ramaker, and P. W. M. Blom. Light intensity dependence of open-circuit voltage of polymer:fullerene solar cells. *Applied Physics Letters*, 86(12):123509, 2005.

[97] M. Limpinsel, A. Wagenpfahl, M. Mingebach, C. Deibel, and V. Dyakonov. Photocurrent in bulk heterojunction solar cells. *Physical Review B*, 81(8):085203, 2010.

[98] D. Rauh, A. Wagenpfahl, C. Deibel, and V. Dyakonov. Relation of open circuit voltage to charge carrier density in organic bulk heterojunction solar cells. *Applied Physics Letters*, 98(13):133301, 2011.

[99] R. Hamilton, C. G. Shuttle, B. O'Regan, T. C. Hammant, J. Nelson, and J. R. Durrant. Recombination in Annealed and Nonannealed Polythiophene/Fullerene Solar Cells: Transient Photovoltage Studies versus Numerical Modeling. *The Journal of Physical Chemistry Letters*, 1(9):1432–1436, 2010.

[100] C. van Berkel, M. J. Powell, R. Franklin, and I. D. French. Quality factor in a-Si:H nip and pin diodes. *Journal of Applied Physics*, 73(10):5264, 1993.

[101] I. Riedel, E. von Hauff, J. Parisi, N. Martín, F. Giacalone, and V. Dyakonov. Diphenylmethanofullerenes: New and Efficient Acceptors in Bulk-Heterojunction Solar Cells. *Advanced Functional Materials*, 15(12):1979–1987, 2005.

[102] K. Vandewal, A. Gadisa, W. Oosterbaan, S. Bertho, F. Banishoeib, I. Van Severen, L. Lutsen, T. Cleij, D. Vanderzande, and J. Manca. The Relation Between Open-Circuit Voltage and the Onset of Photocurrent Generation by Charge-Transfer Absorption in Polymer:Fullerene Bulk Heterojunction Solar Cells. *Advanced Functional Materials*, 18(14):2064–2070, 2008.

[103] Z. Guan, J. Kim, H. Wang, C. Jaye, D. Fischer, Y. Loo, and A. Kahn. Direct determination of the electronic structure of the poly(3-hexylthiophene):phenyl-[6,6]-C61 butyric acid methyl ester blend. *Organic Electronics*, 11(11):1779–1785, 2010.

[104] J. Blakesley and D. Neher. The relationship between energetic disorder and open-circuit voltage in bulk heterojunction organic solar-cells. *Physical Review B*, 84(7):075210, 2011.

[105] L. J. A. Koster, M. Kemerink, M. Wienk, K. Maturová, and R. Janssen. Quantifying bimolecular recombination losses in organic bulk heterojunction solar cells. *Advanced Materials*, 23(14):1670–1674, 2011.

[106] G. Adriaenssens, S. Baranovskii, W. Fuhs, J. Jansen, and Ö. Öktü. Photoconductivity response time in amorphous semiconductors. *Physical Review B*, 51(15):9661–9667, 1995.

[107] A. Foertig, J. Rauh, V. Dyakonov, and C. Deibel. Shockley equation parameters of P3HT:PCBM solar cells determined by transient techniques. *Physical Review B*, 86(11):115302, September 2012.

[108] G. Wetzelaer, M. Kuik, H. Nicolai, and P. Blom. Trap-assisted and Langevin-type recombination in organic light-emitting diodes. *Physical Review B*, 83(16):165204, 2011.

[109] A. I. Rudenko and V. I. Arkhipov. Drift and diffusion in materials with traps. *Philosophical Magazine Part B*, 45(2):177–187, 1982.

[110] J. Schafferhans, A. Baumann, A. Wagenpfahl, C. Deibel, and V. Dyakonov. Oxygen doping of P3HT:PCBM blends: Influence on trap states, charge carrier mobility and solar cell performance. *Organic Electronics*, 11(10):1693–1700, 2010.

[111] C. G. Shuttle, R. Hamilton, J. Nelson, B. C. O'Regan, and J. R. Durrant. Measurement of Charge-Density Dependence of Carrier Mobility in an Organic Semiconductor Blend. *Advanced Functional Materials*, 20(5):698–702, 2010.

[112] D. Rauh, C. Deibel, and V. Dyakonov. Charge Density Dependent Nongeminate Recombination in Organic Bulk Heterojunction Solar Cells. *Advanced Functional Materials*, 22(16):3371–3377, 2012.

[113] T. Kirchartz and J. Nelson. Meaning of reaction orders in polymer:fullerene solar cells. *Physical Review B*, 86(16):165201, 2012.

[114] R. C. I. MacKenzie, C. G. Shuttle, M.L. Chabinyc, and J. Nelson. Extracting Microscopic Device Parameters from Transient Photocurrent Measurements of P3HT:PCBM Solar Cells. *Advanced Energy Materials*, 2(6):662–669, 2012.

[115] X. Yang, J. Loos, S. Veenstra, W. Verhees, M. Wienk, J. Kroon, M. Michels, and R. J. Janssen. Nanoscale morphology of high-performance polymer solar cells. *Nano letters*, 5(4):579–583, 2005.

[116] B. Xue, B. Vaughan, C. Poh, K. Burke, L. Thomsen, A. Stapleton, X. Zhou, G. Bryant, W. Belcher, and P. Dastoor. Vertical Stratification and Interfacial Structure in P3HT:PCBM Organic Solar Cells. *The Journal of Physical Chemistry C*, 114(37):15797–15805, 2010.

[117] G. Kalita, M. Masahiro, W. Koichi, and M. Umeno. Nanostructured morphology of P3HT:PCBM bulk heterojunction solar cells. *Solid-State Electronics*, 54(4):447–451, 2010.

[118] M. Gluecker, A. Foertig, V. Dyakonov, and C. Deibel. Impact of nongeminate recombination on the performance of pristine and annealed P3HT:PCBM solar cells. *physica status solidi (RRL) - Rapid Research Letters*, 8:337–339, 2012.

[119] S. S. van Bavel, M. Bärenklau, G. de With, H. Hoppe, and J. Loos. P3HT/PCBM Bulk Heterojunction Solar Cells: Impact of Blend Composition and 3D Morphology on Device Performance. *Advanced Functional Materials*, 20(9):1458–1463, 2010.

[120] R. Mauer, I. Howard, and F. Laquai. Effect of Nongeminate Recombination on Fill Factor in Polythiophene/Methanofullerene Organic Solar Cells. *The Journal of Physical Chemistry Letters*, 1(24):3500–3505, 2010.

[121] T. J. K. Brenner, Z. Li, and C. R. McNeill. Phase-Dependent Photocurrent Generation in Polymer/Fullerene Bulk Heterojunction Solar Cells. *The Journal of Physical Chemistry C*, 115(44):22075–22083, 2011.

[122] F. Robert. Solar energy. Outlook brightens for plastic solar cells. *Science*, 332(6027):293, 2011.

[123] D. Credgington, F. Jamieson, B. Walker, T. Nguyen, and J. R. Durrant. Quantification of geminate and non-geminate recombination losses within a solution-processed small-molecule bulk heterojunction solar cell. *Advanced Materials*, 24(16):2135–2141, 2012.

[124] S. Albrecht, S. Janietz, W. Schindler, J. Frisch, J. Kurpiers, J. Kniepert, S. Inal, P. Pingel, K. Fostiropoulos, N. Koch, and D. Neher. Fluorinated copolymer PCPDTBT with enhanced open-circuit voltage and reduced recombination for highly efficient polymer solar cells. *Journal of the American Chemical Society*, 134(36):14932–44, 2012.

[125] A. Foertig, A. Wagenpfahl, T. Gerbich, D. Cheyns, V. Dyakonov, and C. Deibel. Nongeminate Recombination in Planar and Bulk Heterojunction Organic Solar Cells. *Advanced Energy Materials*, 2(12):1483, 2012.

[126] B. Collins, Z. Li, J. R. Tumbleston, E. Gann, C. R. McNeill, and H. Ade. Absolute Measurement of Domain Composition and Nanoscale Size Distribution Explains Performance in PTB7:PC71BM Solar Cells. *Advanced Energy Materials*, 2012.

[127] S. Lou, J. Szarko, T. Xu, L. Yu, T. Marks, and L. Chen. Effects of additives on the morphology of solution phase aggregates formed by active layer components of high-efficiency organic solar cells. *Journal of the American Chemical Society*, 133(51):20661–20663, 2011.

[128] H. Kraus, S. Väth, J. Kern, A. Foertig, A. Sperlich, C. Deibel, and V. Dyakonov. Triplet Excitons in High-Efficiency Organic Solar Cell Materials. *in prep.*

[129] Y. Liang and L. Yu. A new class of semiconducting polymers for bulk heterojunction solar cells with exceptionally high performance. *Accounts of chemical research*, 43(9):1227–1236, 2010.

[130] A. Foertig, J. Kniepert, M. Gluecker, V. Dyakonov, D. Neher, and C. Deibel. Nongeminate and Geminate Recombination as performance limit in PTB7:PC71BM solar cells. *submitted.*

[131] F. Jamieson, E. Domingo, T. McCarthy-Ward, M. Heeney, N. Stingelin, and J. R. Durrant. Fullerene crystallisation as a key driver of charge separation in polymer/fullerene bulk heterojunction solar cells. *Chemical Science*, 3(2):485–492, 2012.

[132] D. Jarzab, F. Cordella, J. Gao, M. Scharber, H.-J. Egelhaaf, and M. Loi. Low-Temperature Behaviour of Charge Transfer Excitons in Narrow-Bandgap Polymer-Based Bulk Heterojunctions. *Advanced Energy Materials*, 1(4):604–609, 2011.

[133] G. Grancini, M. Maiuri, D. Fazzi, A. Petrozza, H-J. Egelhaaf, D. Brida, G. Cerullo, and G. Lanzani. Hot exciton dissociation in polymer solar cells. *Nature Materials*, 11(12):1–5, 2012.

[134] L. J. A. Koster. Charge carrier mobility in disordered organic blends for photovoltaics. *Physical Review B*, 81(20):205318, 2010.

[135] S. Albrecht, W. Schindler, J. Kurpiers, J. Kniepert, J. C. Blakesley, I. Dumsch, S. Allard, K. Fostiropoulos, U. Scherf, and D. Neher. On the Field Dependence of Free Charge Carrier Generation and Recombination in Blends of PCPDTBT/PC70BM: Influence of Solvent Additives. *The Journal of Physical Chemistry Letters*, 3(5):640–645, 2012.

[136] M. Hirade and C. Adachi. Small molecular organic photovoltaic cells with exciton blocking layer at anode interface for improved device performance. *Applied Physics Letters*, 99(15):153302, 2011.

[137] T. M. Clarke, F. Jamieson, and J. R. Durrant. Transient Absorption Studies of Bimolecular Recombination Dynamics in Polythiophene/Fullerene Blend Films. *The Journal of Physical Chemistry C*, 113(49):20934–20941, 2009.

[138] M. Tong, N. Coates, D. Moses, and A. J. Heeger. Charge carrier photogeneration and decay dynamics in the poly(2,7-carbazole) copolymer PCDTBT and in bulk heterojunction composites with PC70BM. *Physical Review B*, 81(12):125210, 2010.

[139] J. Nelson. Diffusion-limited recombination in polymer-fullerene blends and its influence on photocurrent collection. *Physical Review B*, 67(15):155209, 2003.

[140] A. Thakur, G. Wantz, G. Garcia-Belmonte, J. Bisquert, and L. Hirsch. Temperature dependence of open-circuit voltage and recombination processes in polymer-fullerene based solar cells. *Solar Energy Materials and Solar Cells*, 95(8):2131–2135, 2011.

[141] L. Pettersson, L. Roman, and O. Inganäs. Modeling photocurrent action spectra of photovoltaic devices based on organic thin films. *Journal of Applied Physics*, 86(1):487–496, 1999.

[142] S. Selberherr. *Analysis and Simulation of Semiconductor Devices*. Springer-Verlag, 1984.

[143] B. Rand, D. Burk, and S. Forrest. Offset energies at organic semiconductor heterojunctions and their influence on the open-circuit voltage of thin-film solar cells. *Physical Review B*, 75(11):115327, 2007.

[144] D. Veldman, S. C. J. Meskers, and R. A. J. Janssen. The Energy of Charge-Transfer States in Electron Donor-Acceptor Blends: Insight into the Energy Losses in Organic Solar Cells. *Advanced Functional Materials*, 19(12):1939–1948, 2009.

[145] J. Xue, B. P. Rand, S. Uchida, and S. R. Forrest. Mixed donor-acceptor molecular heterojunctions for photovoltaic applications. II. Device performance. *Journal of Applied Physics*, 98(12):124903, 2005.

[146] D. Cheyns, J. Poortmans, P. Heremans, C. Deibel, S. Verlaak, B. Rand, and J. Genoe. Analytical model for the open-circuit voltage and its associated resistance in organic planar heterojunction solar cells. *Physical Review B*, 77(16):165332, 2008.

[147] D. Credgington, Y. Kim, J. Labram, T. D. Anthopoulos, and J. R. Durrant. Analysis of Recombination Losses in a Pentacene/C 60 Organic Bilayer Solar Cell. *The Journal of Physical Chemistry Letters*, 2:2759–2763, 2011.

[148] Y. Terao, H. Sasabe, and C. Adachi. Correlation of hole mobility, exciton diffusion length, and solar cell characteristics in phthalocyanine/fullerene organic solar cells. *Applied Physics Letters*, 90(10):103515, 2007.

[149] D. Cheyns. Privat Communication. 2012.

Appendix A

# Relation between charge carrier decay order and $\tau_{\Delta n}$

The small perturbation charge carrier lifetime $\tau_{\Delta n}$ is determined from transient photovoltage (TPV) measurements. TPV is a small perturbation technique based on the fact that the change in carrier density $\Delta n$ is small in comparison to the steady state charge carrier density $n$. Considering a generalized recombination dynamic $\frac{dn}{dt} = kn^{\lambda+1}$ the small perturbation in $n$ can be described as,

$$\frac{d\Delta n}{dt} = \frac{d(n+\Delta n)}{dt} - \frac{dn}{dt} = k(n+\Delta n)^{\lambda+1} - kn^{\lambda+1} \tag{A.1}$$

$$= kn^{\lambda+1}\left(1+\frac{\Delta n}{n}\right)^{\lambda+1} - kn^{\lambda+1} \tag{A.2}$$

$$\approx kn^{\lambda+1}\left(1+(\lambda+1)\frac{\Delta n}{n}\right) - kn^{\lambda+1} \tag{A.3}$$

$$= kn^{\lambda+1}\left((\lambda+1)\frac{\Delta n}{n}\right) \tag{A.4}$$

$$\frac{d\Delta n}{dt} = \frac{dn}{dt}\left((\lambda+1)\frac{\Delta n}{n}\right) \tag{A.5}$$

while the relation $(1-x)^n \approx 1-nx$ was used, valid for $nx << 1$. Using the first derivative of Eq. (4.2) together with Eq. A.5 yields

$$\frac{dn}{dt} = -\frac{n}{(\lambda+1)\tau_{\Delta n}} \overset{\text{Eq. 3.4}}{=} \frac{n}{\tau(n)}, \tag{A.6}$$

and therefore shows the relation of small perturbation carrier lifetime $\tau_{\Delta n}$ and the recombination order $\lambda+1$. Considering the experimentally derived relations for $n$, c.f. Eq. (5.5) and $\tau_{\Delta n}$, c.f. Eq. (5.4) the above derived Eq. (A.6) yields,

$$\frac{dn}{dt} = -\frac{n^{\lambda+1}}{(\lambda+1)\tau_{\Delta n_0} n_0^{\lambda}}. \tag{A.7}$$

Appendix B

# Device simulation parameters

The following parameters were extracted by fitting the current–voltage characteristics of planar and bulk heterojunction devices under 1 sun illumination. The simulation was carried out by A. Wagenpfahl and his macroscopic device simulator.

| parameter | symbol | BHJ | PHJ | unit |
|---|---|---|---|---|
| work function ITO/BCP | $W_{F_{ITO}}$ | -4.848 | -4.848 | eV |
| workfunction Ag | $W_{F_{Ag}}$ | -4.05 | -4.05 | eV |
| LUMO CuPc | $\mathrm{LUMO}_{CuPc}$ | -3.0 | -3.0 | eV |
| HOMO CuPc | $\mathrm{HOMO}_{CuPc}$ | -5.1 | -5.1 | eV |
| LUMO $C_{60}$ | $\mathrm{LUMO}_{C_{60}}$ | -4.05 | -4.05 | eV |
| HOMO $C_{60}$ | $\mathrm{HOMO}_{C_{60}}$ | -6.15 | -6.15 | eV |
| mobility CuPc | $\mu_e$ | $3 \cdot 10^{-9}$ | $1.7 \cdot 10^{-8}$ | $\mathrm{m}^2/\mathrm{Vs}$ |
| mobility $C_{60}$ | $\mu_e$ | $3 \cdot 10^{-9}$ | $3 \cdot 10^{-6}$ | $\mathrm{m}^2/\mathrm{Vs}$ |
| density of states | $N_D$ | $5 \cdot 10^{26}$ | $5 \cdot 10^{26}$ | $\mathrm{m}^{-3}$ |
| dielectric constant CuPc | $\varepsilon_{CuPc}$ | – | 3.4 | – |
| dielectric constant $C_{60}$ | $\varepsilon_{C_{60}}$ | – | 4.0 | – |
| dielectric constant blend | $\varepsilon_{blend}$ | 3.4 | – | – |
| polaron pair dist. | $r_{PP}$ | 1.2 | 1.2 | nm |
| polaron decay rate | $k_r$ | – | $1.4 \cdot 10^5$ | $\mathrm{s}^{-1}$ |

Table B.1: Parameters for device simulation found from fits on respective experimental $j/V$ data.

Appendix C

# List of Publications

## Full Papers

Paper–1 Concentration and Temperature Dependent Recombination in Polymer-Fullerene Solar Cells.
**A. Foertig**, A. Baumann, D. Rauh, V. Dyakonov, C. Deibel. *Applied Physics Letters* **95**, 052104, (2009).

Paper–2 Impact of nongeminate recombination on the performance of pristine and annealed P3HT:PCBM solar cells.
M. Gluecker, **A. Foertig**, V. Dyakonov, C. Deibel. *Rapid Research Letters* **6**, No. 8 337-339, (2012).

Paper–3 Shockley Equation Parameters of Organic Solar Cells determined by Transient Techniques.
**A. Foertig**, J. Rauh, V. Dyakonov, C. Deibel. *Physical Review B* **86**, 115302, (2012).

Paper–4 Bimolecular Recombination in Planar and Bulk Heterojunction Organic Solar Cells.
**A. Foertig**, A. Wagenpfahl, T. Gerbich, D. Cheyns, V. Dyakonov, C. Deibel. *Advanced Energy Materials* **2**, 12, 1483, (2012).

Paper–5 Nongeminate and Geminate Recombination in PTB7:$PC_{71}BM$ solar cells.
**A. Foertig**, J. Kniepert, M. Gluecker, T. Brenner, V. Dyakonov, D. Neher, C. Deibel. *Advanced Functional Materials* (2013).

Paper–6 Order of Decay of Mobile Charge Carriers in P3HT:PCBM Solar cells
C. Deibel, D. Rauh, **A. Foertig**, *Applied Physics Letters* **103**, 043307, (2013).

Paper–7 Triplet Excitons in High-Efficiency Organic Solar Cell Materials.
H. Kraus, S. Vaeth, J. Kern, **A. Foertig**, A. Sperrlich, C. Deibel, V. Dyakonov. *in preparation* (2013).

# Contributions to Conferences

## Talks

1. High Order Temperature Dependent Recombination in Polymer-Fullerene Solar Cells.
   **A. Foertig**, A. Baumann, D. Rauh, T. Gerbich, V. Dyakonov, C. Deibel,
   *DPG-Frühjahrstagung in Regensburg*, (2010).

2. Charge Trapping as the Origin of the High Order Recombination in Pristine and Annealed Polythiophene-Fullerene Solar Cells.
   **A. Foertig**, J. Lorrmann, A. Baumann, C. Deibel, V. Dyakonov,
   *Material and Research Society (MRS) Fall meeting, Boston*, (2010).

3. Recombination Dynamics in Oxygen Exposed Bulk Heterojunction Solar Cells.
   **A. Foertig**, A. Baumann, C. Deibel, V. Dyakonov,
   *DPG-Frühjahrstagung in Berlin*, (2011).

4. Morphology induced impact of charge carrier recombination on the $j/V$ response of organic solar cells.
   **A. Foertig**, M. Gluecker, C. Deibel, V. Dyakonov,
   *DPG-Frühjahrstagung in Dresden*, (2012).

## Poster presentations

1. Transient Photovoltage and Photocurrent of Polymer-Fullerene Solar Cells.
   **A. Foertig**, A. Baumann, D. Rauh, T. Gerbich, V. Dyakonov, C. Deibel,
   *DPG-Frühjahrstagung in Dresden*, (2009).

2. Investigation of the Photocurrent in Polymer-Fullerene Solar Cells. Organic Photovoltaics.
   **A. Foertig**, M. Mingebach, M. Limpinsel, A. Wagenpfahl, V. Dyakonov, C. Deibel,
   *Organic Photovoltaics, SPP1355 Spring School, Krippen*, (2010).

Anhang D

# Danksagung

Diesen Abschnitt möchte ich nutzen um mich bei den Personen zu bedanken, die mich während meiner Arbeit am Institut begleitet und unterstützt haben und damit ein erfolgreiches Abschließen meiner Promotion ermöglichten. Mein Dank geht besonders an:

- Prof. Dr. Vladimir Dyakonov für die Betreuung dieser Doktorarbeit im direkten Anschluss an meine Diplomarbeit. Gerade die unkonventionellen und im ersten Moment auch unbequemen Fragen im Vorfeld von Präsentationen bei Tagungen oder vor dem Einreichen von Manuskripten bei wissenschaftlichen Journalen, gaben oft neue Denkansätze und waren äußerst hilfreich und zielführend.

- Prof. Dr. Jean Geurts für die spontane und unkomplizierte Bereitschaft zur Begutachtung dieser Arbeit.

- PD Dr. Carsten Deibel für unzählige Diskussions- und Interpretationsrunden während der Promotion und Diplomarbeit. Sein stets offenes Ohr bei aufkommenden physikalischer Problemen und Fragestellungen weiß ich sehr zu schätzen.

- Meinen Freund und Kollegen am Transport-Kryo Andreas Baumann für die tolle Zusammenarbeit im Labor, die ausgiebige Aufarbeitung der Bundesliga Spieltage und die meist hart umkämpften Tennismatches nach der Arbeit sowie den unvergessen Dephotex-Trip nach Barcelona. Zudem ein besonderer Danke fürs Korrekturlesen dieser Arbeit!

- Die Mitstreiter im Solarzellen-Team für die vielen wissenschaftlichen Diskussionen und die tolle Teamarbeit. Besonders erwähnt seien hier Markus Mingebach und Andreas Zusan für die Arbeit im Labor, Wapf als Simulant meiner Wahl, Daniel Rauh für die intensive Betreuung während der Diplomarbeit und die tolle Dephotex-Zeit sowie natürlich Jens Lorrmann für Python und IT-Hilfe jeglicher Art und die Floorball-Matches.

- Prof. Fricke für die Möglichkeit, seine Energietechnik Vorlesung betreuend zu begleiten und die hoch interessanten Gespräche und Einblicke, die sich daraus ergaben.

- David Cheyns für die Probenpräparation am IMEC und die gute Zusammenarbeit.

- Meinen Diplomanden Thiemo Gerbich und Markus Glücker für ihre Mithilfe - es hat viel Spaß gemacht mit euch zu arbeiten.

- Allen Bürokollegen von E07 der vergangenen Jahre – Moritz Liedke, Julien Gorenflot, Daniel Mack, Jens Lorrmann, Stefan Walter, Alexander Wagenpfahl und Andreas Baumann – es war eine grandiose Zeit!

- Den Supercappos Volker Lorrmann und Christian Weber für die Abwechslung vom Forschungsgebiet der OPV und unzähligen spaßigen Momente auch abseits der Uni.

- Den Kollegen aus der Photophysik-Ecke Björn Gieseking, Julia Kern, Julien Gorenflot, und allen Diplomanden für anregende Diskussionen in den Meetings und im Labor.

- Den lehrstuhleigenen IT-Spezialisten Andreas Sperlich und Hannes Kraus für die stets kompetente Hilfe, wenn der Rechner, sein Bediener oder das Netz mal einen schlechten Tage hatten.

- André Thiem-Riebe für seine Wartungsdienste im Labor und das wachsame Auge im Bezug auf die Laborsicherheit.

- Valentin Baianov für seine gewissenhafte Arbeit und Hilfe bei neuen Optiken oder Problem mit dem Laser.

- Unsere gute Seele am Lehrstuhl Diep Phan für ihre tatkräftige Unterstützung bei Bestellungen, Dienstreisen, Abrechnungen oder allen anderen erdenklichen Problemen und bürokratischen Hindernissen.

- Den gesamten Lehrstuhl der EP VI für die tolle Arbeitsatmosphäre und so manche Feierlichkeit, die noch lange in meiner Erinnerung bleiben wird. Danke für insgesamt 4 1/2 tolle Jahre!

Ein ganz großes Dankeschön geht an meine Freunde, meine Familie und insbesondere an meine Eltern Gerda und Rainer. Durch ihre Unterstützung während des Studiums und der Promotion wurde diese Arbeit erst ermöglicht.
Last but not least gebührt meiner Freundin Katrin natürlich noch ein dickes Danke. Es ist unbezahlbar, wenn man nach schlechten Tagen an der Uni jemanden hat, der einem zuhört und wieder etwas aufbaut. Dabei hat sie stets an mich geglaubt und mir schier unendliches Verständnis vor allem während der finalen Schreibphase entgegen gebracht. Vielen lieben Dank!